Alma Mater Studiorum - Università di Bologna

DOTTORATO DI RICERCA IN

MECCANICA E SCIENZE AVANZATE DELL'INGEGNERIA

Ciclo 35

Settore Concorsuale: 09/A1 - INGEGNERIA AERONAUTICA, AEROSPAZIALE E NAVALE

Settore Scientifico Disciplinare: ING-IND/07 - PROPULSIONE AEROSPAZIALE

DEVELOPMENT OF NUMERICAL TOOLS FOR THE SIMULATION, DESIGN AND OPTIMIZATION OF A HELICON PLASMA THRUSTER

Presentata da: Nabil Souhair

Coordinatore Dottorato

Lorenzo Donati

Supervisore

Fabrizio Ponti

Co-supervisore

Enrico Corti

Mirko Magarotto

Esame finale anno 2023

So, surely with hardship
comes ease.

Quran 94:5

Acknowledgements

I stand here today with a feeling of immense gratitude and a sense of accomplishment. The journey to this point was not an easy one, but it was made possible by the unwavering support and encouragement from the people who matter the most to me.

Firstly, I would like to express my deepest gratitude to my late father, who may not be here with me today, but whose spirit and legacy live on through my work. His unwavering belief in my abilities and his encouragement to pursue the academic path has been the driving force behind my success. I will forever cherish the memories of his words, “Insha’Allah you will become a Doctor” and it is with great pride that I dedicate this thesis to his memory.

I would also like to express my heartfelt gratitude to my wife, for her love, and support throughout this journey, and to my family for being there for me, cheering me on and providing me with the encouragement I needed to succeed.

I am also grateful to my dear friend Hady, who has been a constant source of inspiration. I am honored to have him as my Space Brother.

Finally, I would like to extend my sincere gratitude to my supervisors, Prof. Fabrizio Ponti and Dr. Mirko Magarotto. Their guidance and expertise throughout my doctorate journey has been instrumental in shaping my research and helping me to reach this point. Their support and encouragement have been a beacon of hope and have helped me to persevere even when the road ahead seemed uncertain.

To all of those who have supported me throughout this journey, your support and encouragement have been the foundation upon which this thesis was built, and I am forever grateful for all that you have done for me.

Abstract

In the last years, the Helicon Plasma Thruster (HPT) concept has been proven to be a valid candidate to generate thrust for small satellites and CubeSats. In order to further increase the performances of such a thruster, and to evaluate its applicability to bigger satellites, accurate numerical tools are required to simulate the plasma dynamics in a HPT. The main phenomena governing a HPT consists in plasma production and heating in the production stage, namely inside a Helicon source, and plasma acceleration and detachment in the region downstream the Helicon source, which is called plume stage. Two main topics have been addressed in this work thesis. First, the development of a *Global Model* (GM) with several chemistry models suitable for preliminary analysis of HPTs fed with noble gases such as argon, neon, krypton and xenon, and alternative propellants such air and iodine have been tackled. For what concerns the noble gases, a novel lumping methodology has been developed. This can be used in order to dramatically reduce the computational cost without affecting accuracy when modelling the excited species in the plasma chemistry for both GM and multidimensional codes. Regarding iodine, this propellant is becoming of great interest as a valid alternative to xenon in the electric propulsion field, therefore there is a growing need for models capable of predicting the thruster performance accounting for its chemistry. In this regard, a GM with an iodine chemistry set has been developed; cross-sections and reaction rates have been collected from literature as well. For what concerns air, this gained a great deal of interest in the recent years due to the application the air-breathing technology. In this regard, a chemistry model has been set collecting data, namely cross-sections and transport coefficients, from literature and a GM capable of simulating a HPT has been developed. Second, a 3D self-consistent numerical tool capable of accurately predicting the plasma generation and transport across a HPT was developed. In particular, the tool can treat discharges with a generic 3D geometry, and model the actual plasma-antenna coupling. Specifically, the 3D numerical tool consists of two main modules, i) the EM module which provides the power deposited by the antenna into the plasma, and ii) the FLUID module, responsible of predicting the plasma profiles driven by the deposited power. The two modules run iteratively until a steady state solution is converged. Optionally, a third module is available for solving the plume with either i) a simplified semi-analytical approach, ii) a PIC code, or iii) directly by integration of the fluid equations. In conclusion, results provided exploiting both the numerical tools have been benchmarked against experimental measures of HPTs or Helicon reactors, obtaining very good qualitative agreement with the experimental trend for what concerns the GM; in regard of the 3D numerical strategy, an excellent agreement of the physical trends predicted against the measured data (deviations lower than 25%), is obtained.

Contents

Appendices

List of Figures

List of Tables

Chapter 1

Helicon Plasma Thruster

1.1 Rationale of Electric Propulsion Systems

In conventional chemical rockets, thrust is obtained heating a working fluid by means of a dedicated chemical reaction (usually combustion but also decomposition [1]) and expanding it through a nozzle. Therefore, in a chemical rocket the main constraints which limit the velocity of the exhaust fluid, and in turn the specific impulse, are:

- the maximum amount of heat that can be provided to the fluid without damaging the walls of the combustion chamber and of the nozzle
- the energy that the chemical reaction can provide

In electric thrusters these limitations does not hold true because:

- the working fluid is constrained away from the thruster's solid walls by electric means (e.g., magnetostatic fields [2, Chap. 5])
- the upper values of specific impulses attainable with electric propulsion (up to 10000 s), are obtained accelerating the working fluid with the aid of Electrostatic or Electro-Magnetic (EM) body-forces (e.g., Lorentz force [2, Chap. 8.1])

In literature, electric propulsion concepts have often been divided into three categories depending on the means in which the working fluid is accelerated: (i) *electrothermal propulsion*, if the propellant is heated with electric means and then accelerated with a nozzle; (ii) *electrostatic propulsion*, if an electric body-force is applied for accelerating and ionizing particles; (iii) *electromagnetic propulsion*, if an ionized propellant stream is accelerated by means of the interaction of magnetic fields and currents (the former can be both internal or external to the stream [2, Chap. 8.1]). Table 1.1 provides the typical performances (thrust T and specific impulse I_{sp}) of the most diffused electric, and chemical, thruster concepts.

Clearly, in order to provide electric heating or EM body-forces, electric thrusters require dedicated power supplies. The amount of electrical power Pw required for achieving certain thruster performances (i.e., thrust T and a specific impulse I_{sp}) is given by

$$Pw = \frac{1}{2}\eta T I_{sp} \tag{1.1}$$

Propulsion concept	T [N]	I_{sp} [s]
Electric		
Electrothermal	10^{-3} - 10	
- Resistojet		≤ 500
- Arcjet		≤ 1000
Electrostatic	10^{-6} - 1	
- Ion		200 - 10000
- Hall effect		300 - 6000
- FEEP		≤ 10000
Electromagnetic	10^{-6} - 1	
- Magnetoplasmadynamic		2000 - 5000
- PPT		1000
- Cathodeless		≤ 2000
Chemical		
Liquid monopropellant	10^{-1} - 10^{3}	≤ 300
Liquid bipropellant	1 - 10^{6}	≤ 450
Solid	10^{2} - 10^{7}	≤ 350

Table 1.1: Summary of the performances (thrust T and specific impulse I_{sp}) of the most diffused electrical and chemical thruster concepts [2, 3, 4, 5].

where η is the efficiency of thrust power conversion. The mass of the power supply m_P depends principally on Pw, therefore it can be assumed that

$$m_P = \alpha_P \; Pw \tag{1.2}$$

where α_P is a proportionality constant. Combining Eq. 1.1 and Eq. 1.2 it can be easily shown that [2, Chap. 1.4]:

- for a certain mission profile, increasing I_{sp} above a certain threshold value is no more convenient in terms of the total spacecraft mass, because the increase of the power supplies mass m_P overcomes the saving up of propellant mass
- for a certain amount of electrical power Pw available, increasing I_{sp} results in a reduction of T

Therefore, due to the m_p constraint: (i) the thruster with the highest specific impulse is not always the most suited for a certain mission scenario; (ii) as shown in Table 1.1, electric thrusters are usually characterized by higher specific impulses than chemical rockets but also by significantly lower thrust attainable. Moreover, an electric propulsion system is in general more complex than a chemical one because extra components are required.

Typically, the power is supplied to the thruster by means of a Power Processing Unit (PPU) which processes the DC electric power provided from the satellite into the specific form required by the thruster (e.g., increasing the voltage or DC/AC conversion). In order to guarantee a high electrical efficiency and a reduced mass and volume, the PPU is usually one of the most complex and challenging components of an electric propulsion system [4]. At the same time, a fluidic line is in general required to provide the propellant to the thruster. Even though the latter is not much more complex than for a mono-propellant or a cold gas thruster, the flows to be handled are usually very small and occur for very prolonged periods of time (months), therefore special challenges arise for the design of precise flow controllers and leak-free valving [4]. Therefore, the main disadvantages of an electric thruster with respect to a chemical one are:

- a lower thrust attainable due to the limited power available on a satellite (i.e., the m_p constraint)
- the more complex and expensive process required to integrate the thruster into a satellite

Because of the substantial differences between chemical and electric thrusters, the mission scenarios in which two typologies of space propulsion concepts can be applied are significantly different

- Electric propulsion is particularly suited for interplanetary orbit transfers or station keeping corrections, where the required high total impulses can be provided with low-thrust and long-time manoeuvres
- Chemical propulsion instead is the only option now available for launchers which require very high thrusts (up to tens of mega-Newton) in order to overcome the Earth's gravity force

A fairly complete list of space missions employing electric thruster can be found in [6]; it can be easily noted that the most widely employed electric propulsion concepts are Ion and Hall-effect thrusters [7].

1.2 Helicon Plasma Thruster

One of the most promising concepts of plasma propulsion system under development is the Helicon Plasma Thruster (HPT) [8] (see Fig. 1.1). Referring to Fig. 1.2, two main stages can be distinguished in a HPT: the production stage in correspondence of the plasma source, and the acceleration stage (or the "plume" stage) downstream the exhaust section of the thruster. Plasma is produced by introducing a mass flow of gaseous propellant into a Helicon reactor [10]. This consists of a dielectric tube surrounded by a Radio Frequency (RF) antenna working in the MHz range [11, 12]. Permanent magnets or coils are wrapped around the tube in order to provide a quasi-axial magnetic field that allows the propagation of Helicon waves and enhances the confinement of the plasma inside the source [13, 14]. The magnetic field largely influences also the acceleration stage providing the "magnetic nozzle" effect downstream the exhaust section of the thruster [15]. In a HPT, the stream of exhausted particles is a quasi-neutral and current-free plasma [16], therefore the system does not need grids, electrodes and neutralizers like in traditional electric propulsion devices [17]. For this reason, HPTs are considered a cost-effective alternative particularly suitable for applications such as SmallSats and CubeSats [11, 12]. Moreover, thanks to their simple design, HPTs can be operated with various propellants [18, 19, 12]. In synthesis, the HPT concept is simple from an engineering and a manufacturing point of view, versatile and with a virtually endless operational lifetime [8]. To summarize, the HPT encompasses:

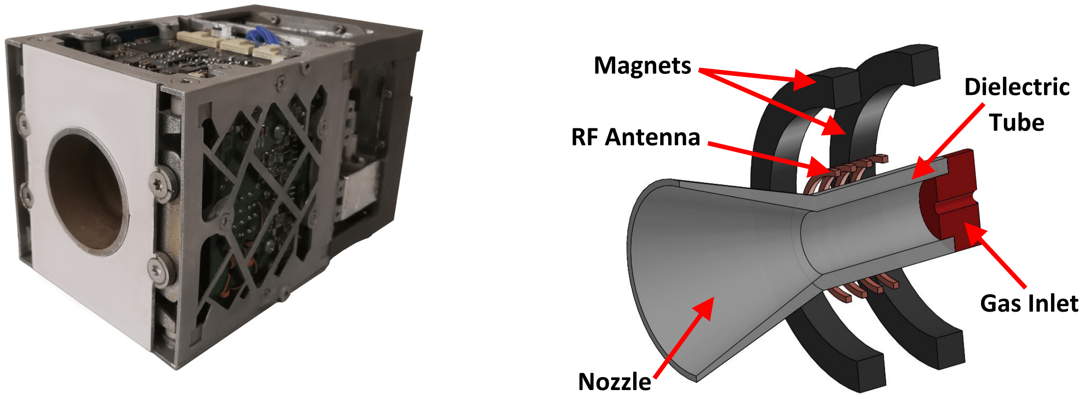

Figure 1.1: REGULUS, a Helicon Plasma Thruster produced by T4i [9] and its schematics.

- a dielectric tube inside which plasma is produced ionizing the propellant
- a Radio Frequency (RF) antenna that works in the MHz range, and produces the EM fields for plasma generation and heating
- permanent magnets or coils that generate a magneto-static field with divergent field lines that act as magnetic nozzle

The first research on HPTs was carried out by Boswell and the space plasma propulsion group at the Australian National University in the early 2000s [20]. Afterwards, the

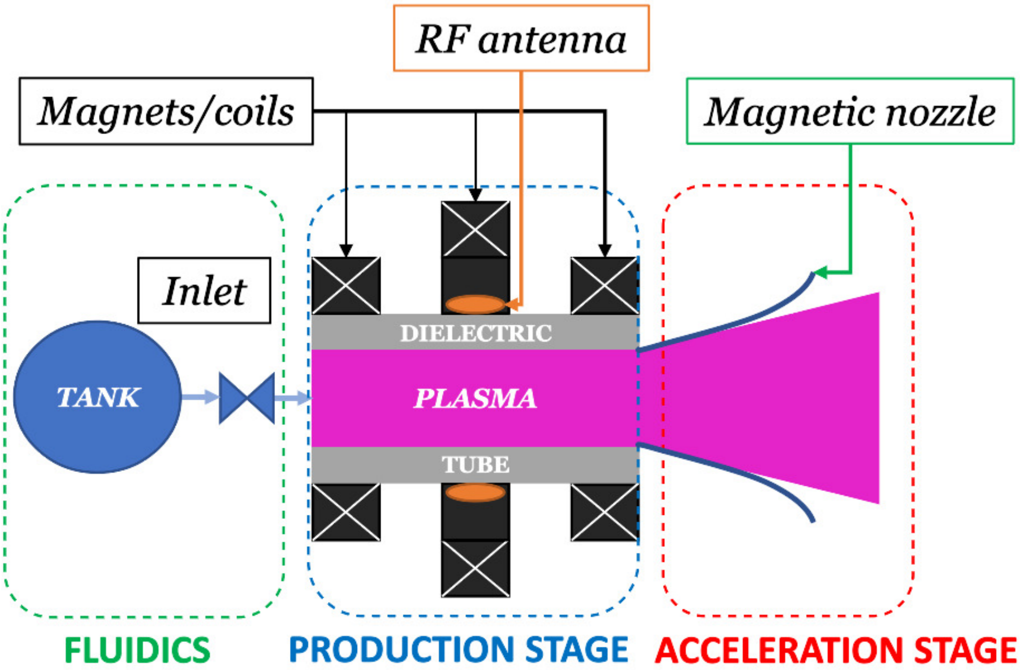

Figure 1.2: Schematic of a Helicon plasma source.

HPT technology has been developed at the University of Padova during several projects such as the European HPH.COM [21] and the Italian SAPERE/STRONG [22]. The outcomes of these two projects allowed the realization of REGULUS [11, 12], a propulsion unit developed by T4i [23] for CubeSats larger than 6U and SmallSats. The VASIMR rocket, developed by NASA, is another case of propulsive system which employs a Helicon source for the production stage [24]. The UC3M University of Madrid, along with SENER Aeroespacial, is designing and testing a 1 kW thruster as part of the HIPATIA project [25], while the universities of Stuttgart and Manchester have been working on an atmosphere-breathing HPT to be used in Very Low Earth Orbits (VLEO) [18]. The research under way at Tohoku University in Japan is also shedding light on the physical mechanisms and plasma behaviour that govern the performance of HPTs, allowing for their optimisation [26]. The Massachusetts Institute of Technology [27], the Michigan Institute of Technology [28], and the Washington University [29] have also worked on and contributed to the HPT technology. In Tab. 1.2, the main HPT research projects and performance from literature are reported.

The key aspect of the HPT is the Helicon plasma source (i.e. the production stage). Compared to Inductively Coupled Plasma (ICP) and Capacitively Coupled Plasma (CCP) [30], Helicon sources are characterized by a very efficient plasma production: high plasma densities ($\geq 10^{19}$ m^{-3}) can be reached with simple antenna geometry (e.g. single loop, helix, and Nagoya Type-III [31]) and moderate RF power [10]. The first experiments on Helicon sources date back to '60s when Lehane and Thonemann [32] measured EM waves propagating in a cylindrical source at about 15 MHz: a very low frequency range for the waves known to propagate in plasma at that time. Since the 80's, Helicon discharges have become a very intense field of research, both from a theoretical and a technological standpoint, in particular thanks to the contributions of Chen and Boswell [10, 33, 34]. The applications in which Helicon sources have been principally employed are: enhanced plasma processing [35], material surface modification [36], semiconductor manufacturing processes [37], and space propulsion.

Institution	Pw [W]	T [mN]	Propellant	$L \times \Phi$ [mm]
Ad Astra	$\approx 2 \times 10^5$	$\approx 10^3$	H/Ar/Kr	1000×100
ANU	≤ 900	$1 - 3$	Ar	300×10
UNIPD	≤ 50		Ar	200×40
T4i	$50 - 150$	≤ 1	I_2/Xe	100×20
UC3M	$\leq 10^3$		Ar/Xe	200×30
Todai	$\leq 3 \times 10^3$	≤ 6	Ar	1000×100
Tohokudai	$800 - 6000$	$10 - 60$	Ar	200×100
MIT	$\approx 10^3$	≈ 10	Ar/N_2	200×40
UMich	≤ 200		Xe	
UW	$\leq 5 \times 10^4$		Ar	200×20
USTUTT	≤ 250		Ar/O_2/N_2	

Table 1.2: Summary of the performances of the most relevant HPTs found in literature: institution which developed the HPT under consideration, input power Pw, produced thrust T (reported only if measured directly), propellant gas adopted, rough estimation of the discharge chamber envelope (length L × diameter Φ).

1.2.1 Phenomena governing the HPT dynamics

In order to optimize the propulsive figures of merit (e.g. specific impulse, thrust/mass ratio, and efficiency) of a HPT, a deep physical insight has to be gained into both the plasma generation and plasma acceleration mechanisms. The dense plasma ($\geq 10^{19}$ m^{-3}) production is governed by the propagation of whistler waves in the discharge region (identified as *Production Stage* in Fig. 1.2). In general, in a uniform Helicon source, the dispersion relation can present two branches which describe the propagation of a faster and a lower wave; the former has been classically referred as Helicon wave and the latter as Trivelpiece-Gould (TG) [38]. Specifically, the power deposition phenomena comes from the dumping of such waves by means of collisional processes and Landau damping [39, Chap. 7.4]. In particular, due to the motion of charged particles and the diffusion processes that contribute to the achievement of a stable discharge, the density production in Helicon sources is non-uniform [40]. The resulting density gradient greatly modifies the wave structure so that non uniform plasma profiles can induce cut-offs at certain radial positions of the cylindrical Helicon source [41]. Moreover, if also the non-uniformity of the actual magneto-static field is accounted, cut-offs, resonances, radial reflections and mode conversions of the excited waves might arise. In turn, the latter can result in power deposition profiles peaked in the central core region of the discharge rather than at the edge as expected in ICPs [30]. Therefore, the key physical phenomena that govern the Helicon source are the EM wave propagation, the plasma transport, and their mutual coupling.

The acceleration and detachment phenomena take place mainly downstream the Helicon source (identified as *Acceleration Stage* in Fig. 1.2). The *Acceleration Stage* is characterized by the formation of a plume where the plasma is more rarefied than in the *Production Stage* (density in the range 10^{16} – 10^{18} m^{-3}) [42]. The plume can be divided into two separate regions, respectively near region and far region, depending on the phenomena which govern the plasma dynamics [43]. In the near region, particle collisions and the geometry of the applied magneto-static field drive the plasma behaviour. Instead in the far region, the expansion of the plasma is mainly governed by the thermal pressure, and the ambipolar diffusion.

1.2.2 Prediction of HPT performances

Provided the complexity and the variety of the phenomena involved in the dynamics of a HPT, several theoretical and numerical strategies have been adopted to predict the performances of such a thruster. Three analytical models have been developed respectively by Lafleur [44], Ahedo [45], and Fruchtmann [46]. These tools are particularly useful in the preliminary design of the thruster, when a quick estimation of the performances (e.g., thrust and specific impulse), and of the plasma properties inside the source (e.g., plasma density and electron temperature) is required. Nonetheless, for the optimization of the thruster more advanced numerical instruments must be adopted.

Several numerical approaches have been pursued in literature for modelling both the *Production Stage* and the *Acceleration Stage*; the most relevant are: fluid, kinetic, Particle-In-Cell with Monte-Carlo Collisions (PIC-MCC), and hybrid. The fluid approach assumes the particle distribution function to describe the plasma in terms of continuity, momentum and energy equations [47]. This method is the less demanding in terms of computational resources and thus is widely used [48]. The fluid approach shows though to be limited whenever the particles distribution function departs significantly from the equilibrium (i.e., the Maxwellian), e.g., when diluted and weakly collisional plasma is considered [49]. The kinetic approach is based on the Boltzmann equation together with the solution of the Maxwell equations [47] and determines uniquely the self-consistent particles distribution function which is then linked to the macroscopic fluid properties of interest (e.g., density, temperature, mean velocity) by its averaging [47]. This method is usually exploited under simplified hypotheses (e.g., mono-dimensional domain) to limit the computational burden [48, 50]. The PIC-MCC approach integrates in accurate manner the particles trajectories under the effect of Electro-Magnetic (EM) fields [51], which makes the method particularly suitable for the investigation of non-equilibrium situations. Even though very accurate, this method is computationally intensive, especially for a high density plasma (e.g., ¿ 10^{19} m^{-3}) [49]. Lastly, to preserve the accuracy of kinetic and PIC-MCC methods, while reducing the computational burden, the approaches mentioned above have been combined in hybrid solvers [52, 49, 53]. In this regard, it is worth mentioning the Hyphen code developed at the University of Madrid in which the hybrid solution of the plasma motion is coupled to an EM module in order to obtain a self-consistent description of HPTs[54] and/or Electron Cyclotron Resonance (ECR) thrusters [53]. With Hyphen, the plasma dynamics is solved both in the source and in part of the plume.

For what concerns the simulation of the *Production Stage*, despite the huge amount of codes that solves for the EM wave propagation [41, 55, 56, 57, 58, 59], there are few examples of numerical models that solve self-consistently the Helicon discharge by accounting for both the power deposition, and the transport phenomena. In this regard, a one-dimensional (1D) radial fluid model [60] has been adopted to study cylindrical Helicon sources; the main limitation of this formulation relies on the assumption of semi-empirical relations to estimate the plasma profiles along the axis of the discharge. A much more accurate two-dimensional (2D) axisymmetric model of a Helicon material processing reactor has been solved by means of both fluid, and hybrid approaches [61, 62]. In the latter the electron distribution function has been calculated with a PIC-MCC strategy, and then exploited for the evaluation of the transport coefficients in the fluid equations. The power deposited by the TG wave has been neglected both in the fluid and hybrid model. Similarly, a 2D-axisymmetric fluid model has been exploited to simulate a Helicon reactor for plasma etching[63]. A cylindrical Helicon source has been studied with an hybrid code where the PIC-MCC approach for ion simulation has been coupled to a fluid formulation of electrons motion [64]. Though only ions have been solved by PIC-MCC, and the geometry is 2D-axisimmetric, the computational cost of this approach can be considerably high for plasma density values higher than $\geq 10^{19}$ m^{-3}. Finally, if the analysis of the *Acceleration Stage* is considered both fluid [15], kinetic [65], PIC-MCC [66], and hybrid [67] approaches have been followed. Nonetheless, particular care must be adopted if fluid or hybrid codes are employed because, in the plume, the particles distribution function can significantly depart from Maxwellian [66], in particular if double layer arises [68, 69]. Nevertheless, it is worth recalling that if two different simulation strategies are adopted to simulate the *Production Stage* and the *Acceleration Stage*, the boundary conditions at the source outlet and at the plume inlet must be chosen carefully in order to avoid mismatching between the two solvers [45].

Recently, a promising numerical tool has been developed at the University of Padova, namely 3D-VIRTUS [70], to simulate the production stage of a HPT. Specifically, this tool is composed of two mutually coupled modules: the first one solves the EM wave propagation and thus the power coupled into the plasma by the antenna [71]; the second is a fluid module that handles the plasma transport [70]. The latter relies on the finite-volume method and has been implemented via the OpenFOAM library [72]. It comprises, for each plasma species (i.e., electrons, ions, neutrals and excited), a set of governing equations based on the Drift-Diffusion (DD) approximation [70]. Considering that the wave propagation has faster dynamics compared to the plasma transport (at least three orders of magnitude [70]) the two phenomena are solved individually in an iterative loop till convergence. 3D-VIRTUS can be used to estimate the propulsive performance (e.g., thrust and specific impulse) of a HPT if coupled with a tool that solves the acceleration stage. To this end, a simplified analytical model [44] has been adopted providing a satisfactory estimation of the propulsive performance of an actual HPT, being the maximum disagreement between predictions and measures of the thrust lower than 30% [13]. Even though this strategy has proven to give promising results, the disagreement must be reduced in order to provide reliable predictions of the propulsive performance. Nonetheless, improvements are needed in terms of the transport models implemented for the solution of both the production stage and the acceleration stage.

1.2.3 Alternative propellants

Xenon has long been the almost-exclusive propellant choice for electric propulsion (EP) [7] since it has a low ionisation energy (12.1 eV), a high ionisation cross-section, a heavy mass (131.3 AMU), and is chemically inert. However, Xe is a trace gas in the atmosphere, and its production as a by-product from the separation of air is an expensive process. As the EP market continues to grow, the current supply of Xe will not be able to satisfy the forecasted demand [73]. Potential alternative propellants are a topic of current interest [74, 75]. Other noble gases, e.g., krypton [19], have been proposed. These are more abundant than Xe in the atmosphere, and can be up to 10-times cheaper, but are still rare gases that are produced in the same way. Water is a promising candidate [76], which is highly abundant. For solar system missions, it would also make feasible the concept of in-situ resource utilisation. Niche EP concepts, that make inherent use of alternative propellants, are also appearing. This includes atmosphere-breathing electric propulsion systems (ABEP), which have potential use in very-low Earth orbits for drag compensation without propellant storage as they can ingest residual atmospheric particles [77, 78]. These non-noble substances, although appealing, are reactive, and their use in conventional Hall Effect Thrusters (HET) is limited owing to cathode degradation [79]. In this respect, cathode-less thrusters under development, such as the Electron Cyclotron Resonance Thruster (ECRT) [80] and HPT [8, 11], are superior and have been tested with a variety of propellants [81]. Of particular interest is iodine [82, 83], which can be stored in its solid state and, being three-times denser than Xe, provides a higher total impulse for a given storage volume. Both atomic and diatomic iodine also have a lower ionisation energy than Xe (10.5 and 9.3 eV). It can be stored at ambient conditions, so no cryogenic system is required. Its procurement cost is very low (90% lower than Xe), and it presents no transportation challenges due to the absence of pressurised tanks. Solid iodine has already been successfully tested in orbit in systems such as the NPT30 ion thruster of ThrustMe [84] and T4i's REGULUS-50 HPT [12]. However, the use of iodine creates unique design and operational challenges. Iodine has a high electronegativity that can lead to corrosion with many common materials. Modelling the complex chemistry of alternative propellants in cathode-less thrusters is in its early stages. Models must be capable of handling mixtures of several substances in addition to molecular collisions such as dissociation, vibrational and rotational excitations. For this reason 0D models such as Global Models may come in handy for handling several chemical reactions when studying a HPT working with different propellants.

1.3 Outline of the work

The objectives of this work are grouped in two main parts:

- **Plasma chemistry:** the development of a Global Model (GM) and its exploitation for an accurate analysis of the plasma chemistry of a HPT fed with several propellant. Traditional propellants like argon, neon, krypton and xenon are firstly assessed. Moreover, novel propellants like iodine and air are studied. The GM predicts the volume average properties of the plasma within the production stage. The acceleration stage is tackled either through an analytical model [85] or by means of a Particle-In-Cell (PIC) code, namely Starfish[86, 87].

- **Plasma transport:** the development of a 3D numerical model for the plasma transport through a HPT. The fluid approach is considered for a more accurate analysis of HPTs, particularly for both the production and acceleration stage. To this end, the balance of mass, momentum and energy [88] for each plasma species are implemented in a *C++* numerical code.

The rest of the work is organized as follows:

Chapter 2 First a Global Model is presented. The diffusion models employed are discussed as long as a simple propulsive model used.

Chapter 3 Noble gases such as argon, neon, krypton and xenon are considered in the GM. A novel lumping procedure for accounting several excited states and their transitions is presented and benchmarked against experimental data. A sensitivity analysis on the variance of the database of cross-sections present in literature is shown and the effects on the predictions of plasma parameters such density and temperature, is discussed.

Chapter 4 Iodine is studied as a possible alternative propellant for HPT. The GM presented in Chapter 2 is exploited with an iodine chemistry and diffusion model for studying the discharge chamber of a real HPT. The acceleration stage is handled by a Particle-In-Cell code. Numerical results are compared to experimental data.

Chapter 5 Air chemistry is implemented in the GM. The latter is compared against numerical simulations taken from literature due to lack of experimental data, i.e., a "verification" is done rather than a validation. Moreover, for the sake of validation of the model, the setup of an experimental campaign currently ongoing at the University of Stuttgart with the aim of measuring the performance of an air-breathing HPT, is shown.

Chapter 6 A 3D numerical tool for the solution of the plasma transport focused on the fluid approach and implemented in *C++* through the OpenFOAM libraries, is presented.

Chapter 7 The numerical tool is exploited for providing detailed analysis of an HPT in terms of physical models.

Chapter 8 The numerical tool is benchmarked against data measured on an experimental Helicon reactor taken from literature.

Conclusions The main findings of the research activity are discussed, future work is illustrated and the novelty made by this work is highlighted.

Part I

Global Modelling (GM) of a HPT with alternative propellants

Global models gained a great deal of interest in the past decades as a simulation tool for plasma discharges, mainly due to the reduced-complexity physics and heuristic approach which characterize them. In fact, they represent an ideal tool for implementing complex chemistry sets and plasma processes: global models can embed hundreds or thousands of reactions, which comes in handy when one wants to predict the performance of a HPT dealing with different propellants.

Chapter 2

Global Models

Global Models (GM) are 0D volume averaged models, where densities and temperatures are spatially averaged and only their time evolution is tracked. The variation in space of each physical quantity is taken into account through semi-empirical diffusion models. The model solutions allow for tracking of the propulsive parameters and the discharge species densities and temperatures. Furthermore, the developed numerical models can be generalized to applications other than electric propulsion, such as lightning technology, industrial reactors, plasma surface processing, biomedical and waste treatment.
In this work, a GM has been developed in order to predict the performance of HPTs working with multiple propellants. The main assumptions considered are:

(i) the plasma source presents a cylindrical geometry;

(ii) the magnetostatic field is axisymmetric;

(iii) the presence of magnetic cusps in the source is taken into account through a semi-empirical correction [89];

(iv) in the acceleration stage the paraxial approximation holds [90];

(v) in the acceleration stage plasma is frozen to the field lines up to the detachment;

In Fig.2.1, the phenomena associated to the GM control volume are schematically reported. The dynamics of the helicon plasma source are solved according to the conservation of mass (Eq. 2.1) for each species involved in the plasma, and electron energy (Eq. 2.2) equations

$$\frac{dn_I}{dt} = R^I_{chem} - R^I_{wall} - R^I_{ex} + R^I_{in} \tag{2.1}$$

$$\frac{d}{dt}\left(\frac{3}{2}n_e T_e\right) = P_{RF} - P_{chem} - P_{wall} - P_{ex} \tag{2.2}$$

where n_I is the number density of the species I. T_e is the electron temperature in eV. For the species I, R^I_{chem} is the source/sink term associated to plasma reactions, R^I_{wall} to wall losses, R^I_{ex} to particles outflow, and R^I_{in} to particles inflow. P_{RF} is the power coupled to the plasma, along with P_{chem} is the source/sink term associated to plasma reactions, P_{wall}

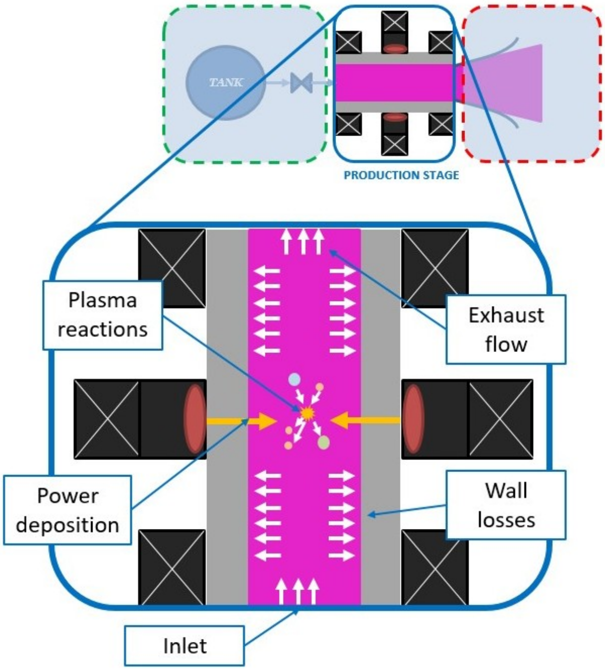

Figure 2.1: Schematics of the GM control volume.

to wall losses, and P_{ex} to particles outflow. The plasma reactions considered are discussed in more details in the next chapters according to the propellant considered. Nevertheless, the main reactions consist in elastic scattering, ionization and excitation, thus the R^I_{chem} and P_{chem} terms read [91]

$$R^I_{chem} = \sum_J K_{JI} n_J n_e - \sum_J K_{IJ} n_I n_e \tag{2.3}$$

$$P_{chem} = \sum_I \sum_J K_{IJ} n_I n_e \Delta U_{IJ} + \sum_I K_{II} n_I n_e \frac{3m_e}{m_I} T_e \tag{2.4}$$

where K_{IJ} is the rate constant for the inelastic transitions from species I to species J, K_{II} is the rate constant for elastic collisions between species I and electrons, ΔU_{IJ} is the energy difference (in eV) between species I and species J, and m_e and m_I are the electron mass and the species I mass respectively [92]. Assuming the Bohm sheath criterion at the source walls, and a sonic thruster outlet [93], similar expressions hold for R^I_{wall} and R^I_{ex}

$$R^I_{wall} = \frac{S^I_{wall}}{V} \Gamma^I_{wall} \tag{2.5}$$

$$R^I_{ex} = \frac{S^I_{ex}}{V} \Gamma^I_{ex} \tag{2.6}$$

where V is the volume of the source, Γ^I is the particle flux, and S^I is the equivalent (or effective) source surface for particle loss. For ions and electrons $\Gamma^e = \Gamma^i = n_e u_B$ where

u_B is the Bohm speed [93]. For what concerns the equivalent surface, S^I_{wall} is accounted according to the model described in Sec. 2.1, whereas S^g_{ex} is equal to the physical thruster outlet area and, assuming the neutrals are in the free-molecular regime, $\Gamma^g = 1/4 n_g u_{th}$, where u_{th} is the neutrals thermal speed [94]. From the Bohm sheath criterion, the energy terms read [93]

$$P_{wall} = R^e_{wall}\left(2 + \log\sqrt{\frac{m_i}{2\pi m_e}}\right)T_e \tag{2.7}$$

$$P_{ex} = R^e_{ex}\left(2 + \log\sqrt{\frac{m_i}{2\pi m_e}}\right)T_e \tag{2.8}$$

2.1 Diffusion model

In order to define the particles and energy fluxes at the walls a diffusion model must be included in the GM. It is well known that in proximity of the walls a sheath of charged particles is formed [95] which greatly influences the spatial density variation. The latter can be accounted for by means of an heuristic formulation of the edge-to-wall ratio proposed by Godyak [96] and later extended by Lee and Lieberman [95]. Furthermore, these models can be further extended to account for non-uniform magnetic fields (e.g., magnetic cusps) and electronegative plasmas.

2.1.1 Edge-to-wall density ratio

For low pressure conditions, and according to Godyak [96], the edge-to-wall ratio reads:

$$h_L = \frac{n(L/2)}{n(0)} \approx 0.86\left(3 + \frac{L}{2\lambda}\right)^{-1/2} \tag{2.9a}$$

$$h_R = \frac{n(R)}{n(0)} \approx 0.8\left(4 + \frac{R}{\lambda}\right)^{-1/2} \tag{2.9b}$$

where h_L and h_R represent the density ratios between the wall and the bulk respectively for a discharge composed of two infinite plates at the intermediate distance L, and an infinite cylinder with radius R. It is worth reporting that Eqts. 2.9 lose validity when dealing with high pressure regime. Lee and Lieberman [95] proposed another heuristic solution that accounts for both low and high pressure regimes, which reads:

$$h_L = \frac{n(L/2)}{n(0)} \approx 0.86\left(3 + \frac{L}{2\lambda} + \left(\frac{0.86 l u_\mathrm{B}}{\pi D_a}\right)^2\right)^{-1/2} \tag{2.10a}$$

$$h_R = \frac{n(R)}{n(0)} \approx 0.8\left(4 + \frac{R}{\lambda} + \left(\frac{0.8 R u_\mathrm{B}}{\chi_{01} J_1(\chi_{01}) D_a}\right)^2\right)^{-1/2} \tag{2.10b}$$

In 2.10, D_a is the ambipolar diffusivity [88], u_B is the Bohm velocity, J_1 and χ_{01}, respectively the Bessel function of the first order and the first zero of the zeroth-order Bessel function. In presence of an axial magnetic field B, the cross-field ambipolar diffusivity $D_{\perp a}$ [88] must be taken into account.

The overall equivalent loss surface is then expressed through the effective area A_{eff} defined as:

$$A_{\text{eff}} = 2\pi R^2 h_L + 2\pi R L h_R \tag{2.11}$$

Electronegativity

According to Liebermann [97], in electronegative plasma, positive and negative ions show a tendency to stratify into an electronegative core and an outer electropositive layer. More specifically, negative ions are confined by the potential drop in proximity of the sheath (e.g, at the walls or at the thruster's outlet). The latter in fact is mainly populated by electrons and positive ions, and may be affected by the negative ion population in the bulk of the discharge. Therefore, h_L and h_R must be corrected to account for the presence of negative ions, by introducing the electronegativity parameter $\alpha = n_-/n_e$, and the temperature ratios γ_+ and γ_- as described by Chabert [98]. The corrected expressions for h_L and h_R reads, for a low pressure plasma discharge in absence of magnetic field:

$$h_L = 0.86 \left(3 + \frac{L}{2\lambda} + (1+\alpha)^{1/2}\frac{\gamma_+}{5}\left(\frac{L}{\lambda}\right)^2\right)^{-1/2} \left(\frac{\gamma_- - 1}{\gamma_-(1+\alpha)^2} + \frac{1}{\gamma_-}\right)^{1/2} \tag{2.12a}$$

$$h_R = 0.8 \left(4 + \frac{R}{\lambda} + (1+\alpha)^{1/2}\gamma_+\left(\frac{R}{\lambda}\right)^2\right)^{-1/2} \left(\frac{\gamma_- - 1}{\gamma_-(1+\alpha)^2} + \frac{1}{\gamma_-}\right)^{1/2} \tag{2.12b}$$

where

$$\gamma_+ = T_+/T_e \tag{2.13a}$$

$$\gamma_- = T_e/T_- \tag{2.13b}$$

It is worth noting that this formulations does not account for the presence of a magnetic field. In this regard, Mròzek [99] proposed a modified which reads,

$$h_R = 0.8 f_b \left(4 + \frac{R}{\lambda} + (1+\alpha)^{1/2}\gamma_+\left(\frac{R}{\lambda}\right)^2\right)^{-1/2} \left(\frac{\gamma_- - 1}{\gamma_-(1+\alpha)^2} + \frac{1}{\gamma_-}\right)^{1/2} \tag{2.14}$$

where $f_b = (1 + (\omega\tau)^2)^{-1}$, ω is the cyclotron frequency and τ the mean free time.

Magnetic cusps

Although in the GM the assumption of uniform magnetic field is employed, the latter can be corrected through an empirical model [7] in order to account for the effects of cusps in the magnetic topology which happens, e.g., in presence of permanent magnets. In fact, in proximity of the cusps, the magnetic field lines become significantly radial. To account for this effect, in the h_R the ambipolar diffusion coefficient D_a must be employed rather than the perpendicular diffusivity. Then, according to Goebel and Katz [7], the total cusp area A_{cusp} can be introduced as,

$$A_{\text{cusp}} = 4 N_{\text{cusps}} \sqrt{r_{\text{ci}} r_{\text{ce}}} 2\pi R \tag{2.15}$$

where r_{ci}, r_{ce} are respectively the ion and electron cyclotron radii, and N_{cusps} the number of cusps which depends on the magnets configuration. Finally, the effective area [7] becomes then,

$$A_{\mathrm{eff}} = 2\pi R^2 h_L \beta + h_{R\perp}(2\pi RL - A_{\mathrm{cusp}}) + h_{R\|} A_{\mathrm{cusp}} \tag{2.16}$$

2.1.2 Diffusion parameters

In order to evaluate the diffusion parameters, an estimation of the collision frequency ν is required, which reads,

$$\nu = \frac{v_{th}}{\lambda} \tag{2.17}$$

where v_{th} is the thermal velocity, and λ is the mean free path defined as,

$$\lambda = \frac{1}{n_g \sigma} \tag{2.18}$$

where n_g is the gas density and σ is the collision cross section. The Langevin cross section [97] can be employed for the ions [100], which reads,

$$\sigma_L = q_e \left(\frac{\pi}{2\varepsilon_0}\right)^{1/2} \left(\frac{\alpha_p}{\varepsilon_r}\right)^{1/2} \tag{2.19}$$

where α_p is the species polarizability and ε_r is the relative kinetic energy of the colliding particles. Finally, this approach is employed in the GM targeted at the noble gases studied in Chapter 3.

Another approach to compute the diffusion parameters relies on the method of Lennard-Jones potentials which provides an empirical description of the particles' interatomic and intermolecular interactions. In the case of self-diffusion the diffusivity coefficient is defined as [101],

$$D = \frac{3}{8}\sqrt{\frac{k_B T}{M\pi}} \frac{1}{\sigma_{LJ}^2 \Omega^{1,1} n} \tag{2.20}$$

where M, T and n are respectively mass, temperature and density of the self-diffusive species, σ_{LJ} the zeroth energy collision diameter, and $\Omega^{1,1}$ the collision integral [101]. The latter can be evaluated through the following empirical equation,

$$\Omega^{l,s} = \left(\frac{A}{T^{*B}}\right) + \left[\frac{C}{\exp(DT^*)}\right] + \left[\frac{E}{\exp(FT^*)}\right] + \left[\frac{G}{\exp(HT^*)}\right] + RT^{*B}\sin(ST^{*W} - P) \tag{2.21}$$

where $A, B, C, D, E, F, G, H, R, S, W, P$ are empirical coefficients depending on the gas and taken from literature [102], T^* is the reduced temperature defined as $T^* = \frac{T_0}{\epsilon/k_B}$ where T_0 is the heavy species temperature and ϵ/k_B is the second Lennard-Jones parameter [102][103][104].

The self-diffusion model is no more suited when the interactions between two different species in the diffusion process cannot be neglected, thus binary diffusion coefficients must be determined for each species. In particular, the binary diffusion coefficient between a species i and species j can be defined as:

$$D_{ij} = \frac{3}{8}\sqrt{\frac{k_B T}{\pi}\frac{M_i + M_j}{2M_i M_j}}\frac{1}{\sigma_{LJ_i}\sigma_{LJ_j}\Omega_D^{1,1} n} \tag{2.22}$$

and defining:

$$M_{ij} = \frac{2M_i M_j}{M_i + M_j} \tag{2.23a}$$

$$\sigma_{LJ_{ij}} = \sqrt{\sigma_{LJ_i}\sigma_{LJ_j}} \tag{2.23b}$$

$$\left.\frac{\epsilon}{k_B}\right|_{ij} = \sqrt{\left.\frac{\epsilon}{k_B}\right|_i \left.\frac{\epsilon}{k_B}\right|_j} \tag{2.23c}$$

it is possible to write equation 2.24 similarly to 2.20:

$$D_{ij} = \frac{3}{8}\sqrt{\frac{k_B T}{\pi M_{ij}}}\frac{1}{\sigma_{LJ_{ij}}^2 \Omega_D^{1,1}}\frac{1}{n} \tag{2.24}$$

where Ω_D is calculated using 2.21.

When dealing with molecular plasma (e.g., iodine and air), the previous models may fail in describing the diffusion of the species mixtures. To this end, a mixture-averaged approximation must be assumed in the computation of the diffusion coefficient for the generic species i:

$$D_i = \frac{1 - Y_i}{\sum_{j \neq i} \frac{X_i}{D_{ij}}} \tag{2.25}$$

where X and Y are respectively defined by:

$$X_i = \frac{n_i}{\sum n_j} \tag{2.26a}$$

$$Y_i = \frac{M_i n_i}{\sum M_j n_j} \tag{2.26b}$$

In conclusion, this approach is employed in the GM targeted at iodine and air presented in Chapter 4-5.

2.2 Propulsion model

Propulsive performance such as thrust and specific impulse are computed according to the plume model presented in [90], which consists of a quasi-one dimensional description of a HPT. For what concerns the discharge chamber, the principal outputs are the average plasma density n inside the source and the upstream plasma thrust at the source's outlet F_0 which is the plasma thrust contribution in absence of a magnetic nozzle. Regarding the latter, the electrons inertia is assumed to be negligible, the cold ions hypothesis [90, 88] is enforced, and both ions and electrons are assumed to exit the source with the Bhom velocity u_B [39, Chap. 8]; therefore F_0 reads,

$$F_0 = \big(M\Gamma u_B + \langle p_e \rangle\big)A_0 \tag{2.27}$$

where M is the ion mass, Γ is the ions flux at the source outlet (expressed in $\mathrm{m}^{-2}\mathrm{s}^{-1}$), $\langle p_e \rangle$ is the radially averaged electron pressure, and A_0 is the outlet section of the thruster. Eq. 2.27 can be rewritten as

$$F_0 = 2\beta q n T_e A_0 \tag{2.28}$$

where β is a dimensionless parameter that accounts for non-uniformity within the plasma, q is the elementary charge, and T_e the electron temperature (expressed in eV). In the region downstream the source outlet an additional thrust due to the magnetic nozzle F_{mag} is produced; therefore the total thrust provided by the plasma acceleration F_p is equal to

$$F_p = F_0 + F_{mag} \tag{2.29}$$

In particular F_{mag} is given as [46]

$$F_{mag} = \int_V J_\theta B_r dV \tag{2.30}$$

where B_r is the radial component of the magneto-static field, J_θ is the azimuthal plasma current, and V is the volume in which the magnetic nozzle effect is non-negligible. In particular, assuming the paraxial approximation $B_z(r,z) \approx B_z(0,z)$, Eq. 2.30 can be rewritten as [46]

$$F_{mag} = \int_{A_0}^{A} \langle p_e \rangle dA \tag{2.31}$$

where A is the area of the magnetic flux tube which determines the boundary of the magnetic nozzle region. Notably, the role played by the magnetic nozzle is analogous to that of a physical nozzle with the exception that in the latter the force imparted is generated by the pressure at the walls, whereas in the former the average value of the pressure in the whole expansion volume is responsible to the force generation. From mass and momentum conservation [44], Eq. 2.31 can be rewritten as

$$F_{mag} = F_0 \frac{(\mathcal{M}-1)^2}{2\mathcal{M}} \tag{2.32}$$

where $\mathcal{M} = v/u_B$ is the magnetic Mach number, and v is the velocity of the plasma. Thus, the thrust produced by the plasma acceleration can be expressed as

$$F_p = F_0 + F_0 \frac{\big(\mathcal{M}-1\big)^2}{2\mathcal{M}} \tag{2.33}$$

Provided that the plasma detaches from the magnetic field lines at some point downstream the source outlet, the value of $\mathcal{M}$ to be adopted in Eq. 2.33 is $\mathcal{M}_{det}$, namely the magnetic Mach number at the detachment point. A criterion to determine the position where the detachment happens consists in assuming that the latter occurs when the ion gyroradius is equal to the radius of the plasma flow area defined by the diverging magnetic field, hence $\mathcal{M}_{det}$ can be found solving

$$\frac{1}{2}\left(\mathcal{M}_{det}^2 - 1\right) - \ln \mathcal{M}_{det} = \ln\left(\frac{qB_0^2 A_0}{\pi M T_i}\right) \tag{2.34}$$

where B_0 is the magnetic field at the source outlet, and T_i is the ion temperature (expressed in eV). The overall thrust generated with the plasma acceleration is then,

$$F_p = F_0 \frac{\mathcal{M}_{det}^2 + 1}{2\mathcal{M}_{det}} \tag{2.35}$$

Finally, the total thrust T produced by a HPT is the sum of F_p, and of the thrust generated by the neutral gas expansion F_{gas} which reads,

$$F_{gas} = \dot{m}_0 v_g \left(1 + \frac{k_B T_g}{M v_g^2}\right) \tag{2.36}$$

where $\dot{m}_0$ is the input mass flow rate, k_B is the Boltzmann constant, T_g is the neutral gas temperature (expressed in K), $v_g = \sqrt{\gamma k_B T_g / M}$ is the speed of sound, and γ is the specific heat constant. Therefore, the thrust T provided by the HPT reads,

$$T = F_p + F_{gas} \tag{2.37}$$

and the specific impulse I_{sp} can be computed as

$$I_{sp} = \frac{T}{g_0 \dot{m}_0} \tag{2.38}$$

where g_0 is the sea level gravity constant.

Chapter 3

Argon, Neon, Krypton and Xenon

Argon, neon, krypton and xenon are among the most used gases in plasma propulsion and laboratory discharges. The increasingly maturity of plasma technologies fed with these gases has brought to the need for more accurate and reliable numerical simulations of the discharges. In this regard, the modelling of the excited states and their fine-structure plays an important role. This chapter presents a methodology to compute the plasma properties (e.g, density and temperature) by means of a GM. A suitable chemistry model accounting for the dynamics of the excited states in low-pressure (< 50 mTorr) plasma discharges filled with argon, neon, krypton and xenon gases is proposed. Moreover, two main aspects are covered: (i) a novel lumping methodology is proposed to reduce the number of reactions and species considered in order to keep at bay the computational cost without a major loss of accuracy; (ii) the influence that different datasets of cross-sections have on the results has been assessed.

3.1 Introduction

Being particularly simple to store and handle, noble gases like argon, neon, krypton and xenon are frequently used for plasma production. In particular, argon is one of the most used gases in industrial and laboratory discharges [105], neon is common in lightning technology [106], along with krypton and xenon are widely used in space propulsion thanks to their good propulsive performance [17, 107, 108].

The increasingly maturity of plasma technologies has brought to the need for more accurate and reliable numerical simulations of the discharges. In this regard, the modelling of the excited states and their fine-structure plays a non-negligible role [109, 105]. In literature, several approaches have been pursued to simulate plasma discharges accounting for the dynamics of the excited states. Collisional-Radiative Models (CRM) are numerical tools that describe very carefully the transitions between different excited states. Several CRMs for argon plasma have been developed, for instance Boegarts [110] considered 65 energy levels for studying a 1 kV glow discharge. Vlcek, developed a CRM [111] based on the atomic corrected model of Katsonis [112] and applied it to atmospheric arcs [113], low pressure (<50 mTorr) glow discharges and hollow cathodes [114]. In the latter case he considered transitions only between $1s$ and $2p$ states (in Paschen notation). A similar approach is found in the work of Zhu [115] for the low pressure cases for which transitions between $1s$ and $2p$ were considered. Regarding neon, Navratil [106] developed a CRM for studying low pressure positive columns; the interactions between $1s$, $2p$ and higher states have been considered. A similar approach has been adopted by Baghel [116]. Regarding krypton, Gangwar developed a CRM [117] for discharges where the pressure ranges between 1-50 mTorr and considered the dynamics of $1s$, $2p$ and few higher states. Prince performed a similar study for krypton-fed Hall Effect Thrusters [108], whereas Priti [118] and Zhu [119] did it for xenon. A broader review on CRMs can be found in Van Sijde [120]. The main drawback of CRMs is that they provide a 0-Dimensional (0D) description of the system. The profiles of the plasma parameters (e.g., density and temperature) are assumed constant or prescribed by heuristic expressions [105], not derived by the solution of conservation equations. A different approach to simulate the plasma dynamics relies on multidimensional fluid or hybrid solvers [48, 121]. In 1D, 2D and 3D models plasma profiles are solved (and not assumed) even though the dynamics of the excited species is treated with a much lower accuracy with respect to CRMs to avoid an excessive computational burden. In several fluid and hybrid codes the dynamics of the excited species have been neglected [122, 123, 124], in other cases only neutral and charged particles have been tracked [125]. In this regard, many authors assumed that the excited states decay immediately and thus they modeled them just as a loss term in the electron energy equation. Some solvers adopted this strategy for simulating argon [126, 127] and xenon [122, 123, 128, 129] discharges. Other authors consider the excited states by lumping them into one or few effective species. This approach has been used both for argon [130, 131, 132] and krypton [133] discharges. Meunier [134] used a similar strategy for neon, but no details on the lumping methodology has been provided. Nevertheless, a more complete review can be found in Kim [121] or in Van Dijk [48].

The modelling of the excited states is further complicated by the variance between the cross-sections proposed by different authors. In this regard, Pitchford [135] performed a comparative analysis of electron-neutral scattering cross-sections for argon. Swarm parameters like excitation and ionization coefficients from the cross-sections have been computed and compared against measured values. An analogue analysis was done for krypton and xenon by Bordage [136] and for neon by Alves [137]. Nonetheless, a thorough search of the relevant literature regarding comparative studies to assess how such variance affects the prediction of plasma parameters, like electron density, yielded to the conclusion that such analysis has never been published in literature.

In this chapter, the influence that the excited states have on the numerical predictions of plasma properties as density and temperature (i.e., not for spectroscopic purposes), is analyzed. In this regard, the analysis covers two main aspects: (i) definition of a lumping methodology to reduce the energy levels considered, (ii) evaluation of the effect that different datasets of cross-sections have on the numerical results. The lumping strategy aims at the accurate simulation of the excited species with a reduced computational cost and with easier algorithms since only a limited number of species is solved. These features are paramount when the simulation of a plasma discharge shall be iterated numerous times (e.g., for the sensitivity analysis on cross-sections performed in this work) or when dealing with multidimensional codes. The target application of this work is low-pressure discharges (< 50 mTorr) filled with argon, neon, krypton and xenon gases. First, the lumping methodology has been implemented in a 0D model. Results have been benchmarked against those obtained treating each energy level of the excited states as an individual species (i.e., the approach implemented in CRMs). Second, for each gas considered, the estimated plasma density and electron temperature have been validated against the measurements performed on an Inductively Coupled Plasma (ICP) [138]. Different datasets of cross-sections have been used in order to assess their influence on the results and, in turn, on the agreement between experiments and simulations. Finally, the reaction rate coefficients resulting from the combination of datasets have been analytically fitted for each gas and explicitly presented in Appendix A.

3.2 Methodology

In argon, neon, krypton and xenon discharges the species considered are electrons, singly-charged ions, neutrals, and excited states within the fine-structure of the $1s$ and $2p$ energy levels (Paschen notation). In low pressure discharges these species present the highest number-density [115]. The effect of higher excitation energy levels has been neglected, and the idea behind this assumption is discussed more thoroughly when the comparison between numerical and experimental data is presented. Four sets of reactions have been considered, namely electron ionization, electron excitation/de-excitation, elastic scattering and radiative spontaneous emission [139, 109, 140, 118]. Since a low pressure regime is considered, Penning and heavy species reactions are not treated [115]. It is worth noting that the same transitions have been considered for argon, neon, krypton and xenon provided they are noble gases which share the same electronic configuration of the outermost shell [141].

3.2.1 Modelling of the excited states

Regarding the $1s$ excited state, both resonant (i.e., $1s_4$ and $1s_2$) and metastable (i.e., $1s_5$ and $1s_3$) energy levels are taken into consideration. It is worth specifying that the metastable energy levels are those that do not decay via radiative spontaneous emission. Regarding the $2p$ species, all ten levels of the group are considered. In Tab. 3.1, the excited states and the related energy potentials are summarized for argon, neon, krypton and xenon. The species involved and their transitions are schematically described in Fig.3.1. It is worth pointing out that the transitions among the excited states of the same type (e.g., $2p$) have been neglected while collisional reactions between metastable ($1s_5$ and $1s_3$) and resonant ($1s_4$ and $1s_2$) species have been considered.

For each electron reaction considered (i.e., electron excitation, electron ionization and elastic scattering), the rate coefficients are computed as:

$$K_{ij} = \sqrt{\frac{2q}{m}} \int_0^\infty \varepsilon \sigma_{ij} f_0 d\varepsilon \tag{3.1}$$

where i, j represent respectively the starting lower level and the arriving higher energy level, q and m are the elementary charge and the electron mass; σ_{ij} is the electron-impact cross-section for the transition from the lower state i to the upper state j, ε is the electron

Excited states

Level	Paschen config.	Ar U_i [eV]	Ne U_i [eV]	Kr U_i [eV]	Xe U_i [eV]	g_i
1	gs	0	0	0	0	1
2	$1s_5$	11.55	16.62	9.92	8.32	5
3	$1s_4$	11.62	16.67	10.03	8.44	3
4	$1s_3$	11.72	16.72	10.56	9.45	1
5	$1s_2$	11.83	16.85	10.64	9.57	3
6	$2p_{10}$	12.91	18.4	11.30	9.58	3
7	$2p_9$	13.08	18.56	11.44	9.69	5
8	$2p_8$	13.09	18.58	11.45	9.72	7
9	$2p_7$	13.15	18.61	11.53	9.79	3
10	$2p_6$	13.17	18.64	11.55	9.82	5
11	$2p_5$	13.27	18.69	11.67	9.93	1
12	$2p_4$	13.28	18.70	12.1	10.96	3
13	$2p_3$	13.30	18.71	12.14	11.05	5
14	$2p_2$	13.33	18.73	12.14	11.07	3
15	$2p_1$	13.48	18.97	12.26	11.14	1
16	ion	15.76	21.56	14.00	12.13	

Table 3.1: Argon, neon, krypton, xenon energy states in Paschen notation with related energy levels and statistical weights [141].

energy expressed in eV, and f_0 is the electron energy distribution function (EEDF). In the following, a Maxwellian EEDF has been assumed; in case more accurate experimental measurements of the EEDF are available [142], they can be easily inserted in Eq. (3.1). The analytical expression of the Maxwellian EEDF reads [143],

$$f_0(\varepsilon) = 2\sqrt{\left(\frac{1}{T_e^3 \pi}\right)} \exp\left(- \frac{\varepsilon}{T_e}\right) \tag{3.2}$$

To compute the rate coefficients for the reverse transitions (i.e., electron de-excitation), the *principle of detailed balancing* (DBP) was assumed. The required cross-sections read [105]

$$\sigma_{ji}(\varepsilon - \Delta U_{ij}) = \frac{g_i}{g_j} \frac{\varepsilon}{\varepsilon - \Delta U_{ij}} \sigma_{ij}(\varepsilon) \tag{3.3}$$

where σ_{ji} represents the inverse cross-section, $\Delta U_{ij} = U_j - U_i$ is the energy difference between the two states, along with g_i and g_j are the statistical weights which represent the degeneracy of respectively the lower and the higher energy level. The inverse cross-section is then introduced in Eq. (3.1) to obtain the rate coefficient.

Regarding the radiative transitions only spontaneous emission is taken into consideration. The radiative spontaneous emission is associated to a resonant species at the energy level j that decays towards a lower level i with a rate proportional to the *Einstein* coefficient A_{ji}. In particular, a correction factor Λ_{ji} called *escape factor*, is adopted to account for the self-absorption of the radiation by the plasma. The model proposed by

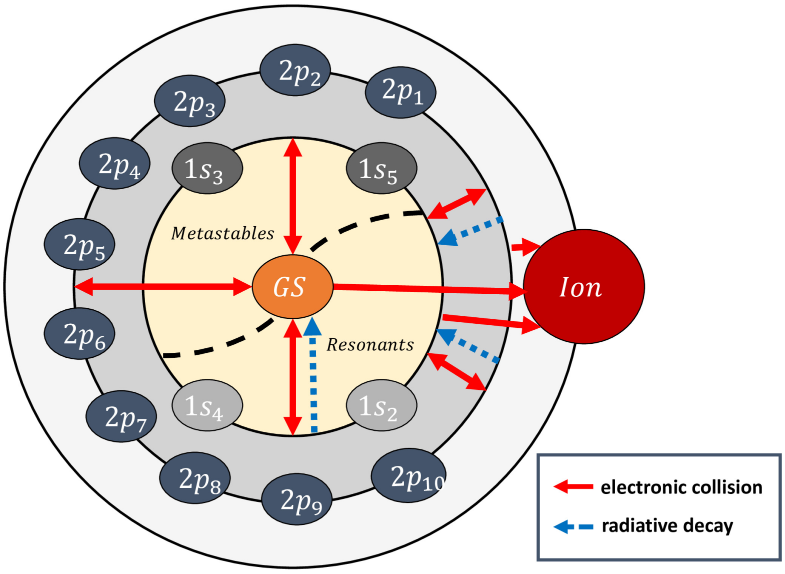

Figure 3.1: Species and transitions considered in this work: the solid arrows represent the excitation/de-excitation and ionization transitions by means of electron collisions, the dashed arrows indicate the radiative transitions, and the dashed lines describe the population exchange between metastable and resonant $1s$ species.

Mewe [144] has been adopted. Under the hypothesis of uniform distribution of emitting and absorbing particles, Λ_{ji} reads

$$\Lambda_{ji} = \frac{2 - e^{-\rho\beta_{ji}/1000}}{1 + \rho\beta_{ji}} \tag{3.4}$$

where ρ is the characteristic length of the geometric domain, and β_{ji} is the reabsorption coefficient for the transition $j \to i$. Since low temperature plasma is considered (i.e., $T_e < 20$ eV), the Doppler broadening is the main significant mechanism of reabsorption [139], hence β_{ji} reads

$$\beta_{ji} = \frac{g_j}{g_i} \frac{\lambda_{ji}^3}{8\pi^{3/2}} n_i A_{ji} \sqrt{\frac{M}{2k_B T_0}} \tag{3.5}$$

where λ_{ji} is the wavelength corresponding to the optical transition $j \to i$, n_i is the number density of the $i - th$ excited state, M is the particle mass, k_B is the Boltzmann constant, and T_0 is the gas temperature (expressed in Kelvin).

Statistical weights, energy levels, and Einstein coefficients are taken from the *National Institute of Standard and Technology* (NIST) database [141]. The cross-sections for the collisional transitions considered are discussed in Sec. 3.3.

3.2.2 Lumping of the energy levels

Following the dynamics of all the excited species (namely, accounting for the fine structure) involves a large number of balance equations to be solved, which leads to an unmanageable computational requirement when fluid (or hybrid) strategies are considered for simulating a plasma discharge. Thus, in order to reduce the number of equations to solve, a novel lumping procedure based on the assumption of Local Thermodynamic Equilibrium (LTE) [145] has been introduced. The LTE hypothesis is not in general verified in low pressure discharges [145, 120] but, according to McWhirter's formula [145], species whose energy is within a certain energy range can be considered in LTE whenever

$$n_e > 10^{19} T_e^{0.5} (\Delta U)^3 \tag{3.6}$$

where n_e is the electron density, T_e the electron temperature and ΔU the energy gap between different excited levels. For a low temperature plasma (say below 20 eV) this condition is satisfied for $n_e > 10^{16}$ m^{-3} for the fine energy levels of both the $1s$ and $2p$ excited states.

Considering an electronic collision transition from a lumped level I to a higher level J

$$X_I + e \rightarrow X_J + e \tag{3.7}$$

the population density increment in time for the lumped states J reads

$$\begin{aligned} &\frac{dn_J}{dt} = K_{IJ} n_I n_e = \sum_i^{N_i} \sum_j^{N_j} K_{ij} n_i n_e \\ &i = 1, ..., N_i; \quad j = 1, ..., N_j \end{aligned} \tag{3.8}$$

where n_I and n_J are the number densities of the lumped states I and J, i and j span the fine-structure of the lumped states that group respectively N_i and N_j electronic energy levels, K_{IJ} is the lumped rate coefficient, and K_{ij} accounts for transitions at fine-structure level. In particular K_{IJ} reads

$$K_{IJ} = \frac{\sum_i^{N_i} \sum_j^{N_j} K_{ij} n_i}{\sum_k^{N_I} n_k} \tag{3.9}$$

Since we consider that LTE holds between the fine-structure energy levels of a lumped state, the Boltzmann relation holds true, namely

$$\frac{n_k}{n_i} = \frac{g_k}{g_i} exp\left(- \frac{U_k - U_i}{k_B T_0} \right) \tag{3.10}$$

where the indices k and i refer to generic levels of the fine-structure. Rearranging Eq. (3.9) in terms of Eq. (3.10), K_{IJ} reads

$$K_{IJ} = \sum_i^{N_i} \left[\frac{\sum_j^{N_j} K_{ij}}{\sum_k^{N_i} \frac{g_k}{g_i} exp\left(- \frac{U_k - Ui}{k_B T_0} \right)} \right] \tag{3.11}$$

The lumped rate coefficient for the inverse transition K_{JI} is obtained combining Eq. (3.9), Eq. (3.10) and the DBP; it reads

$$K_{JI} = \sum_j^{N_j} \left[\frac{\sum_i^{N_i} K_{ij} g_i exp\left(- \frac{U_i}{k_B T_0} \right)}{\sum_k^{N_j} g_k exp\left(- \frac{U_k}{k_B T_0} \right)} \right] \tag{3.12}$$

Moreover, the energy potential associated to the lumped states I reads

$$U_I = \frac{\sum_i^{N_i} g_i U_i}{\sum_i^{N_i} g_i} \tag{3.13}$$

and the lumped statistical weight

$$g_I = \sum_i^{N_i} g_i \tag{3.14}$$

Regarding the radiative transitions

$$X_J \rightarrow X_I + h\nu \tag{3.15}$$

the decay rates have been lumped, similarly to Eq. (3.9), as

$$A_{JI}\Lambda_{JI} = \frac{\sum_i^{N_i} \sum_j^{N_J} n_j A_{ji} \Lambda_{ji}}{\sum_k^{N_j} n_k} \tag{3.16}$$

The excited species have been grouped into three lumped levels, namely $1s_M$, $1s_R$, $2p$. The species considered are listed in Tab. 3.2, while lumped reactions in Tab. 3.3. Finally, it is worth noting that, technically, the lumping methodology has not been applied to the electron impact ionization reactions since the cross-sections found in literature concern the lumped states $1s$ and $2p$, not their fine structure.

Lumped species	Detailed states
gs	ground state
$1s_M$	$1s_5, 1s_3$ (metastable)
$1s_R$	$1s_4, 1s_2$ (resonant)
2p	$2p_{10}, 2p_9, 2p_8, 2p_7, 2p_6, 2p_5, 2p_4, 2p_3, 2p_2, 2p_1$
ion	1^{st} ionization
e	electron

Table 3.2: Species considered; the excited species are grouped in lumped states.

Reactions	Reaction type
$gs + e \rightleftharpoons 1s_M + e$	Excitation / de-excitation
$gs + e \rightleftharpoons 1s_R + e$	Excitation / de-excitation
$gs + e \rightleftharpoons 2p + e$	Excitation / de-excitation
$1s_M + e \rightleftharpoons 1s_R + e$	Excitation / de-excitation
$1s_M + e \rightleftharpoons 2p + e$	Excitation / de-excitation
$1s_R + e \rightleftharpoons 2p + e$	Excitation / de-excitation
$gs + e \rightarrow gs + e$	Elastic scattering
$1s_M + e \rightarrow 1s_M + e$	Elastic scattering
$1s_R + e \rightarrow 1s_R + e$	Elastic scattering
$2p + e \rightarrow 2p + e$	Elastic scattering
$gs + e \rightarrow ion + e$	Electron impact ionization
$1s_M + e \rightarrow ion + e$	Electron impact ionization
$1s_R + e \rightarrow ion + e$	Electron impact ionization
$2p + e \rightarrow ion + e$	Electron impact ionization
$1s_R \rightarrow gs + h\nu$	Decay towards lower state
$2p \rightarrow 1s_M + h\nu$	Decay towards lower state
$2p \rightarrow 1s_R + h\nu$	Decay towards lower state

Table 3.3: Reactions that involve lumped excited states.

3.3 Results

The ICP reactor characterized by Schwabedissen [146] provides a realistic numerical setup to: (i) benchmark the lumping methodology against a detailed analysis of the fine-structure energy levels of the excited species as done in CRMs, (ii) validate the lumping methodology against experiments, (iii) quantify the influence that the cross-section datasets have on the results. The *Global Model* described in Sec. 2 has been used to simulate the ICP when operated with argon, neon, krypton and xenon gases. The species tracked are electrons, singly-charged ions, neutrals at ground state, and excited (i.e., $1s_M$, $1s_R$, and $2p$ lumped energy levels). Moreover, a preliminary analysis has been accomplished to identify the transitions between excited levels that mainly affect the numerical results. To this end, three different cases have been simulated: (i) purely collisional case in which radiative transitions have been neglected; (ii) collisional case with the addition of the $1s$ radiative decay, (iii) collisional-radiative case where all the transitions involving both $1s$ and $2p$ have been accounted for. The latter case, which gives the more complete description of the plasma dynamics, has been used to benchmark and validate the lumping methodology. It is worth highlighting that the variance of the plasma parameters obtained combining different cross-sections depends on the choice of the datasets. The one used in this work include, but are not limited to, the datasets mentioned in the seminal reviews by Pitchford [135], Bordage [136] and Alves [137] which cover a significant portion of the literature.

The Schwabedissen's setup consists in an ICP reactor derived from the GEC RF Reference Cell proposed by Miller [138]. Accordingly to the description reported in [138, 146]: (i) the setup comprises a cylinder discharge chamber with inner diameter 165 mm and length 40.5 mm, (ii) there is no applied magneto-static field, (iii) the gas pressure at standard ambient temperature, namely before plasma ignition, is equal to 20 mTorr. The antenna is realized with five turn spiral coils of outer diameter 100 mm made of 3 mm copper tubing. The antenna is powered at a frequency of 13.56 MHz through a matching network made of two air-dielectric variable capacitors [138]. A Langmuir probe realized with a tungsten wire of radius 75 μm has been used to characterize the source in terms of plasma density and temperature. The measurements considered in this work are taken along the discharge axis, 12 mm above the lower base of the cylindrical chamber. The source has been tested for different values of the deposited power (i.e., power coupled to the plasma) which has been estimated comparing the impedance of the system at plasma off and plasma on [146]. The gases considered are argon, neon, krypton and xenon. The input parameters used in the *Global Model* are synthetically summarized in Tab. 3.4.

Parameter	Value
Diameter	165 mm
Length	40.5 mm
Magneto-static field	0 T
Gas pressure	20 mTorr

Table 3.4: Input parameters of the Global Model used to simulate the ICP reactor.

3.3.1 Benchmark of the lumping strategy

A benchmark case is presented in order to demonstrate the correctness and robustness of the lumping methodology [147, 148, 149]. To this end, the plasma properties (density and temperature) predicted through the lumping methodology have been compared against the ones obtained treating each fine-structure energy level of the excited states as an individual species [150] (see Tab. 3.1). The Schwabedissen's ICP reactor operated with argon gas was simulated with the GM presented in Chapter 2. The two approaches differ mainly for the number of species treated and for the formulation of Eqs. (2.1-2.2), namely for what the mass and power generation/loss terms are concerned. According to the lumping methodology, Eqs. (2.1-2.2) are computed for the set of reactions shown in Tab. 3.3. Instead each fine-structure transition is considered while solving the dynamics of the excited species with the approach implemented in CRMs [115]. The rate constants proposed by Zhu [115] have been employed for this analysis. Electron density (n_e) and temperature (T_e) predicted through the lumping or the detailed methodology present the same trends (see Fig. 3.2a): n_e increases with the deposited power (P) while T_e mildly decreases. In order to quantify the relative error between the two approaches, the quantity $Error = 2|x_{detailed} - x_{lumped}|/(x_{detailed} + x_{lumped})$ has been depicted in Fig. 3.2b in function of P. Regardless the value of P, the percent error between steady state values of n_e and T_e is generally below 1%. This proves the reliability and the robustness of the proposed

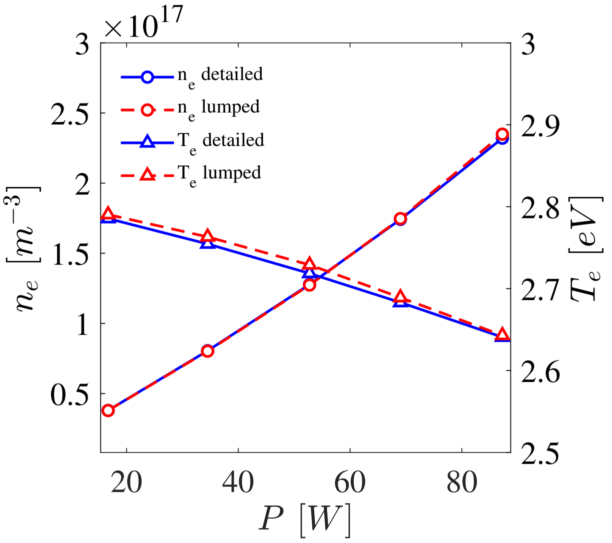

(a)

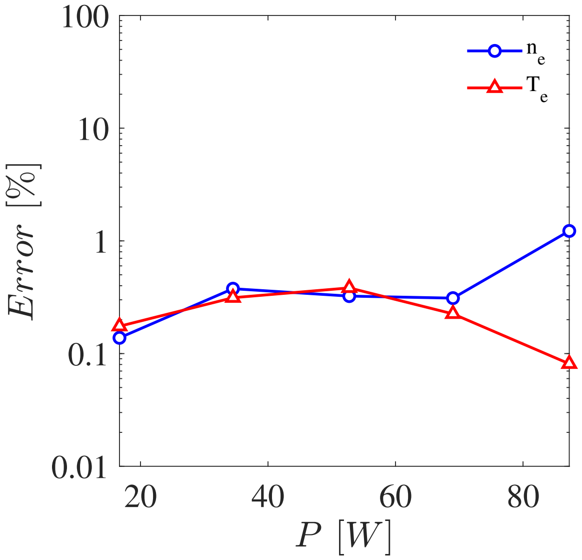

(b)

Figure 3.2: (a) Electron density (n_e) and electron temperature (T_e) in function of the deposited power (P), data are obtained with the lumping strategy or the detailed simulation of the excited states, (b) percent error between n_e and T_e calculated with the detailed and the lumping methodologies.

lumping methodology.

3.3.2 Argon

Excitation	Database reference
$gs + e \rightarrow 1s + e$	[151, 152, 153, 154, 155, 156, 157, 158]
$gs + e \rightarrow 2p + e$	[151, 152, 153, 154, 155, 156, 157, 159]
$1s + e \rightarrow 1s + e$	[155, 156, 160]
$1s + e \rightarrow 2p + e$	[155, 156, 160, 161, 162]

Table 3.5: Datasets of argon cross-sections for excitation reactions.

Elastic scattering	Database reference
$gs + e \rightarrow gs + e$	[163, 151, 164, 153, 154, 155, 156, 157, 165]
$1s + e \rightarrow 1s + e$	[163, 151, 164, 153, 154, 155, 156, 157, 165]
$2p + e \rightarrow 2p + e$	[163, 151, 164, 153, 154, 155, 156, 157, 165]

Table 3.6: Datasets of argon cross-sections for elastic scattering reactions.

Ionization	Database reference
$gs + e \rightarrow ion + e$	[163, 151, 166, 167, 152, 153, 154, 155, 156, 157, 165]
$1s + e \rightarrow ion + e$	[168, 169]
$2p + e \rightarrow ion + e$	[168, 169]

Table 3.7: Datasets of argon cross-sections for ionization reactions.

In Fig. 3.3 numerical data are compared against experiments when the ICP reactor is operated with argon gas. The electron density is depicted as a function of the deposited power (see Fig. 3.3a). Only the average value of the electron temperature is reported (see Fig. 3.3b) since it is almost independent on the deposited power [146]. Measurements have been sampled along the axis of the discharge with a Langmuir probe [146]; the uncertainty

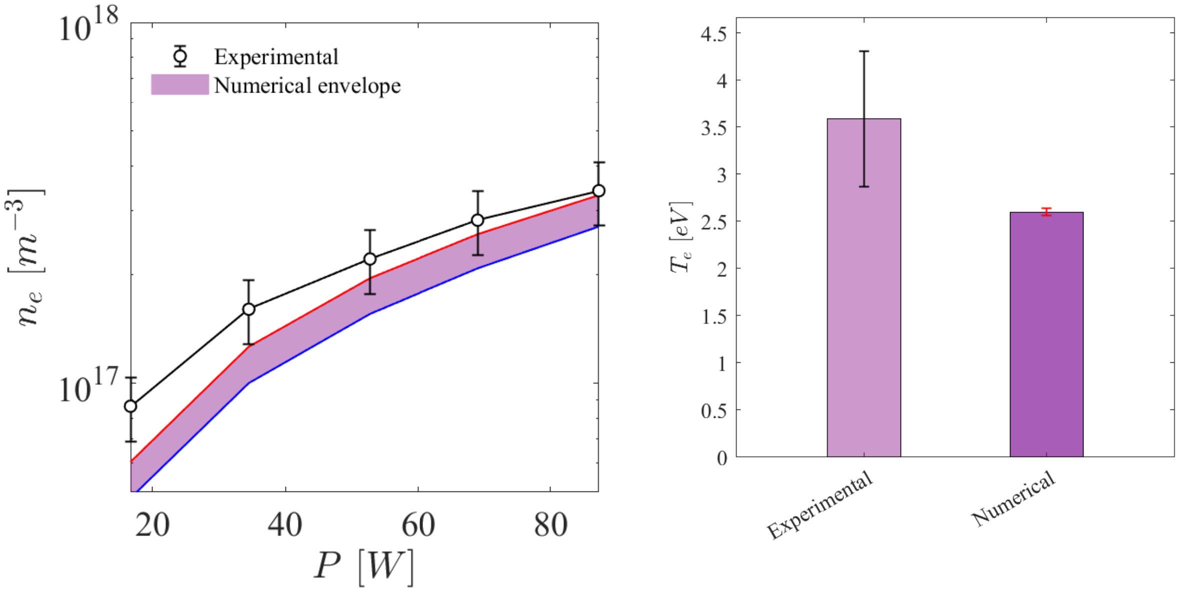

(a)

(b)

Figure 3.3: Comparison between numerical and experimental data when the ICP reactor is operated with argon gas. (a) Electron density n_e as a function of the deposited power P (b) average electron temperature T_e. The numerical envelope refers to results obtained with cross-sections from different datasets. Measurements reported with an uncertainty band of ±20%.

on both n_e and T_e is in the order of 20% [146]. The numerical results have been computed using the cross-section datasets listed in Tab. 3.5-3.7. All the possible combinations of cross-sections have been considered. Therefore numerical results are depicted as an envelope of data comprised between two boundary values, namely they are affected by an error bar related to the uncertainty on the cross-sections. Numerical predictions of n_e underestimate the experimental data by 12%; the numerical error bar is about 20%. The electron temperature is underestimated by 29%. The lowest (highest) values of plasma density correspond to highest (lowest) electron temperatures, the latter differ by 1.5%.

In order to preliminary investigate the role played by transitions between excited species, density of electrons (n_e) and excited species (n_{1s_M}, n_{1s_R}, and n_{2p}), along with electron temperature (T_e) have been reported in Fig. 3.4. Three cases have been compared: purely collisional, collisional plus $1s$ radiative decay, and collisional-radiative (i.e., the one used for the validation). For the sake of brevity, results are discussed only for $P = 70$ W. In the collisional-radiative case n_e is about 40% lower with respect to the purely collisional case, instead T_e increases of about 0.3 eV. The $1s$ radiative decay affects mildly the population of the excited states. Instead the $2p$ radiative decay causes a drop

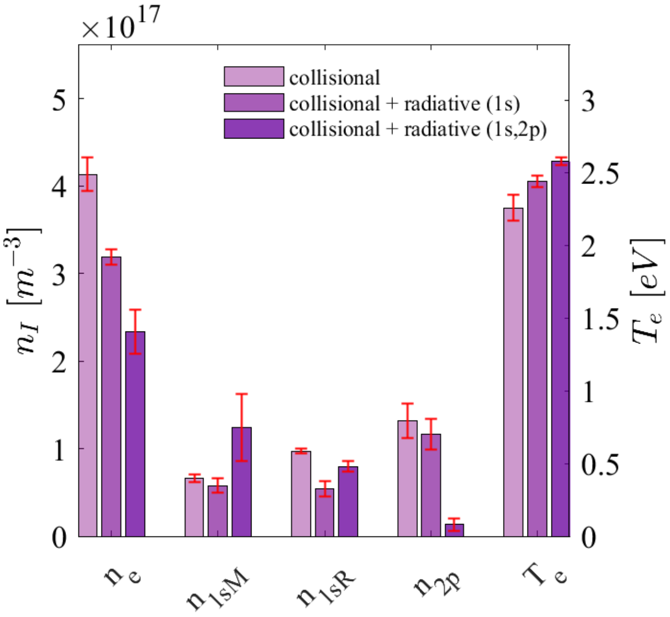

Figure 3.4: Argon gas, deposited power $P = 70$ W. Numerical predictions of density n_I ($I = e$, $1s_M$, $1s_R$, $2p$ for the electrons and the excited species respectively) and electron temperature T_e. Error bars associated to the uncertainty on the cross-sections.

in n_{2p} of more than one order of magnitude. In the collisional-radiative case n_{2p} is more then one order of magnitude lower with respect to n_e; instead n_{1s_M}, n_{1s_R} and n_e are of the same order of magnitude.

3.3.3 Neon

In Fig. 3.5, numerical and experimental data are compared when the ICP reactor is operated with neon gas. The electron density is depicted as a function of the input power (see Fig. 3.5a), only the average value of the electron temperature is reported (see Fig. 3.5b). As in the argon case, the uncertainty on the measures is 20% for both n_e and T_e [146]. Cross-section datasets used for the computation are listed in Tab. 3.8-3.10. The electron density is underestimated by 8% while highest and lowest values differ for about 10%. A disagreement of 2 eV (i.e., a deviation of about 30%) is registered between measures and estimations of the electron temperature. The numerical envelope is quite narrow being the variance of T_e equal to 0.5%.

Results obtained in the collisional, collisional plus $1s$ radiative, and collisional-radiative cases at $P = 110$ W are depicted in Fig. 3.6. The radiative decay causes a reduction of n_e by 29% with respect to the purely collisional case and an increase of T_e by 1 eV. The

$1s$ radiative decay causes a drop of one order of magnitude in n_{1s_R}. This is partly due to having neglected the excitation reaction $1s + e \to 1s + e$ provided that the authors found no data concerning cross-sections in literature. Likewise, the $2p$ radiative decay causes a drop in n_{2p} of more than one order of magnitude. In the collisional-radiative case n_e and n_{1s_M} are of the same order of magnitude while n_{1s_R} and n_{2p} are respectively one and two orders of magnitude smaller.

Excitation	Database reference
$gs + e \to 1s + e$	[153, 155, 156, 157, 165, 152]
$gs + e \to 2p + e$	[153, 155, 156, 157]
$1s + e \to 1s + e$	-
$1s + e \to 2p + e$	[170]

Table 3.8: Datasets of neon cross-sections for excitation reactions.

Elastic scattering	Database reference
$gs + e \to gs + e$	[153, 167, 155, 156, 157, 165, 163]
$1s + e \to 1s + e$	[153, 167, 155, 156, 157, 165, 163]
$2p + e \to 2p + e$	[153, 167, 155, 156, 157, 165, 163]

Table 3.9: Datasets of neon cross-sections for elastic scattering reactions.

Ionization	Database reference
$gs + e \to ion + e$	[155, 156, 163, 166, 153, 167, 157, 165, 152]
$1s + e \to ion + e$	[168]
$2p + e \to ion + e$	[168]

Table 3.10: Datasets of neon cross-sections for ionization reactions.

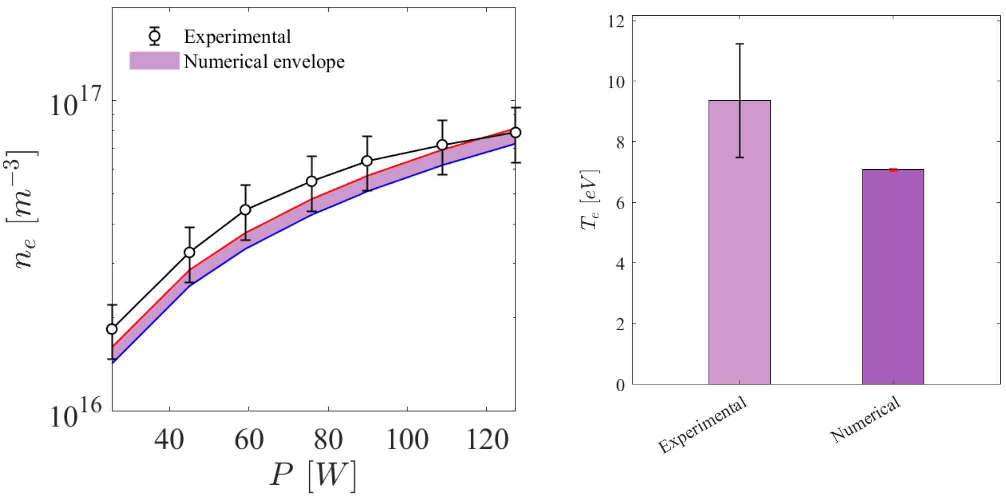

(a)

(b)

Figure 3.5: Comparison between numerical and experimental data when the ICP reactor is operated with neon gas. (a) Electron density n_e as a function of the deposited power P (b) average electron temperature T_e. The numerical envelope refers to results obtained with cross-sections from different datasets. Measurements reported with an uncertainty band of ±20%.

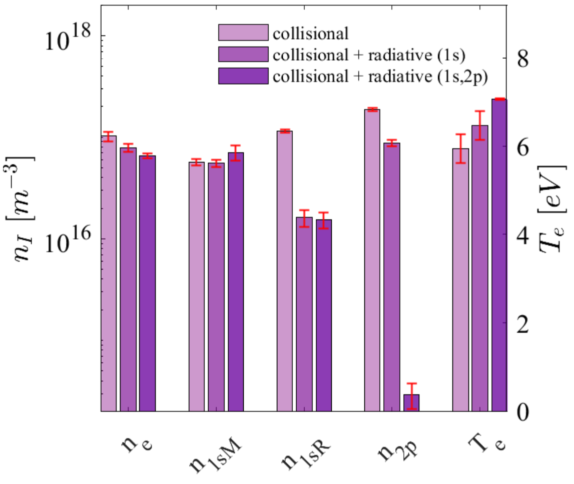

Figure 3.6: Neon gas, deposited power $P = 110$ W. Numerical predictions of density n_I ($I = e$, $1s_M$, $1s_R$, $2p$ for the electrons and the excited species respectively) and electron temperature T_e. Error bars associated to the uncertainty on the cross-sections.

3.3.4 Krypton

The comparison between numerical and experimental data when the ICP reactor is operated with krypton is reported in Fig. 3.7. The uncertainty on the measure of n_e is 30% due to the impossibility of operating the Langmuir probe for $n_e > 6 \times 10^{17}$ m^{-3} to avoid damages [146]. At the same time, uncertainty on T_e is 20% [146]. Datasets of cross-sections used for the computations are reported in Tab. 3.11-3.13. A large span in the envelope of n_e can be noticed being experimental values underestimated by 14% or 46% considering highest or lowest density respectively. T_e is underestimated by 26% and the numerical error bar is about 5%.

Excitation	Database reference
$gs + e \rightarrow 1s + e$	[160, 155, 156, 157]
$gs + e \rightarrow 2p + e$	[160, 155, 156, 157]
$1s + e \rightarrow 1s + e$	[160]
$1s + e \rightarrow 2p + e$	[160]

Table 3.11: Datasets of krypton cross-sections for excitation reactions.

Elastic scattering	Database reference
$gs + e \rightarrow gs + e$	[164, 167, 155, 156, 157, 165, 163]
$1s + e \rightarrow 1s + e$	[164, 167, 155, 156, 157, 165, 163]
$2p + e \rightarrow 2p + e$	[164, 167, 155, 156, 157, 165, 163]

Table 3.12: Datasets of krypton cross-sections for elastic scattering reactions.

Ionization	Database reference
$gs + e \rightarrow ion + e$	[163, 167, 157, 165]
$1s + e \rightarrow ion + e$	[168]
$2p + e \rightarrow ion + e$	[168]

Table 3.13: Datasets of krypton cross-sections for ionization reactions.

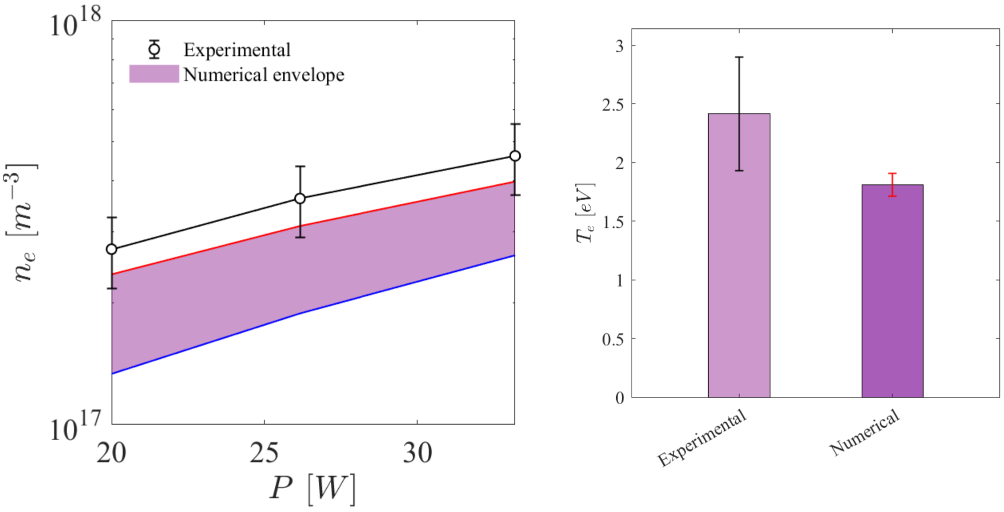

(a) (b)

Figure 3.7: Comparison between numerical and experimental data when the ICP reactor is operated with krypton gas. (a) Electron density n_e as a function of the deposited power P (b) average electron temperature T_e. The numerical envelope refers to results obtained with cross-sections from different datasets. The uncertainty band is ±30% for n_e measures, ±20% for T_e measures

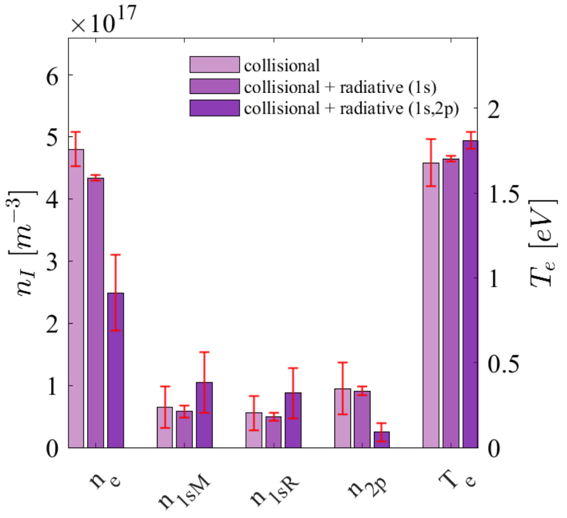

Figure 3.8: Krypton gas, deposited power $P = 26$ W. Numerical predictions of density n_I ($I = e$, $1s_M$, $1s_R$, $2p$ for the electrons and the excited species respectively) and electron temperature T_e. Error bars associated to the uncertainty on the cross-sections.

Data obtained in the collisional, collisional plus $1s$ radiative, and collisional-radiative cases for $P = 26$ W are depicted in Fig. 3.8. The radiative decay causes a reduction in n_e by more than 50% and an increase of T_e by 0.2 eV. As for argon, the $1s$ radiative decay has a mild influence on the dynamics of the excited species. Instead the $2p$ radiative decay causes a drop in n_{2p} of about one order of magnitude. In the collisional-radiative case n_{2p} is one order of magnitude smaller than n_e, n_{1s_M} and n_{1s_R}.

3.3.5 Xenon

Excitation	Database reference
$gs + e \rightarrow 1s + e$	[153, 155, 156, 157]
$gs + e \rightarrow 2p + e$	[155, 156, 157]
$1s + e \rightarrow 1s + e$	[118, 171]
$1s + e \rightarrow 2p + e$	[118]

Table 3.14: Datasets of xenon cross-sections for excitation reactions.

Elastic scattering	Database reference
$gs + e \rightleftharpoons gs + e$	[164, 153, 154, 167, 155, 156, 157, 165]
$1s + e \rightleftharpoons 1s + e$	[164, 153, 154, 167, 155, 156, 157, 165]
$2p + e \rightleftharpoons 2p + e$	[164, 153, 154, 167, 155, 156, 157, 165]

Table 3.15: Datasets of xenon cross-sections for elastic scattering reactions.

Ionization	Database reference
$gs + e \rightarrow ion + e$	[163, 167, 152, 153, 154, 157, 165]
$1s + e \rightarrow ion + e$	[168]
$2p + e \rightarrow ion + e$	[168]

Table 3.16: Datasets of xenon cross-sections for ionization reactions.

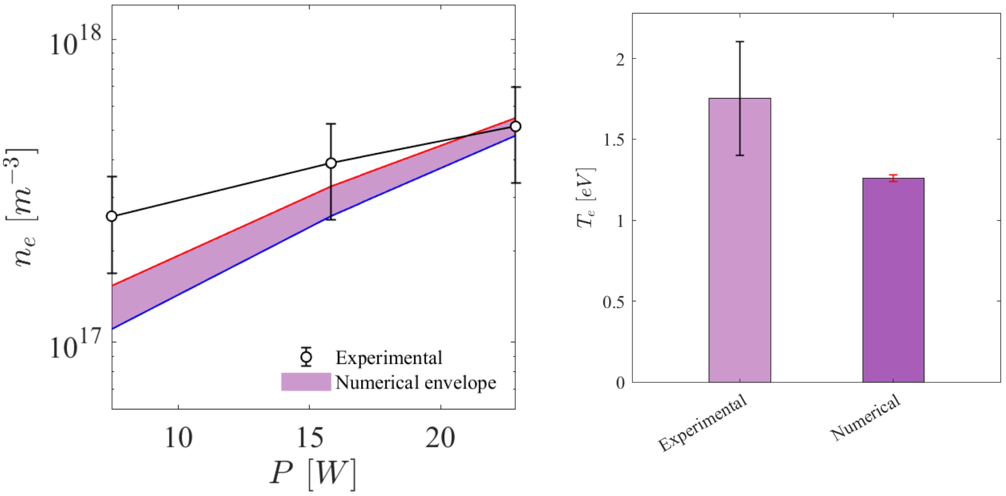

(a)

(b)

Figure 3.9: Comparison between numerical and experimental data when the ICP reactor is operated with xenon gas. (a) Electron density n_e as a function of the deposited power P (b) average electron temperature T_e. The numerical envelope refers to results obtained with cross-sections from different datasets. The uncertainty band is ±30% for n_e measures, ±20% for T_e measures

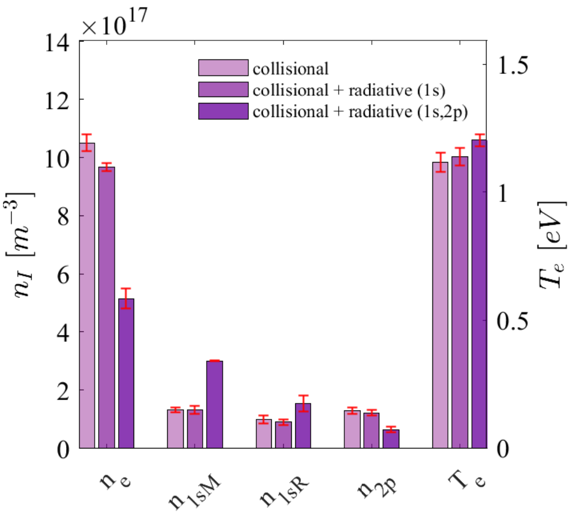

Figure 3.10: Xenon gas, deposited power $P = 23$ W. Numerical predictions of density n_I ($I = e$, $1s_M$, $1s_R$, $2p$ for the electrons and the excited species respectively) and electron temperature T_e. Error bars associated to the uncertainty on the cross-sections.

Results obtained when the working gas is xenon are reported in Fig. 3.9. As for krypton, the uncertainty on the measures is 30% and 20% for n_e and T_e respectively [146]. Datasets of cross-sections used for the computation are reported in Tab. 3.14-3.16. Numerical predictions underestimate n_e by 13%; highest and lowest density differ for about 20%. The electron temperature is underestimated by 29% with a variance on T_e of 1%. Data obtained in the collisional, collisional plus $1s$ radiative, and collisional-radiative cases for $P = 23$ W are depicted in Fig. 3.10. Xenon is the gas for which the radiative decay causes the highest reduction of n_e, namely more than 60%; instead T_e increases by 0.1 eV. The $1s$ radiative decay affects mildly the excited species while the $2p$ radiative decay causes n_{2p} to halve. In the collisional-radiative case n_e, n_{1s_M}, and n_{1s_R} are of the same order of magnitude, while n_{2p} is about one order of magnitude smaller.

3.3.6 Discussion

First, the lumping strategy has been benchmarked against the detailed solution in which the dynamics of each fine structure energy levels is tracked. The error between electron density and temperature predicted with the two approaches is generally less than 1%. Second, the results obtained implementing the lumping strategy on the *Global Model* have been validated against experiments. For what electron density is concerned, numerical results are in fairly good agreement with measurements provided that the numerical envelope overlaps the experimental uncertainty band for all the gases. More precisely, the agreement between numerical predictions and experiments is poorer for krypton and xenon with respect to argon and neon. This might be due to two aspects: (i) in larger atoms the energy of the fine structure levels are more spread, so the LTE hypothesis is progressively less robust; (ii) the Langmuir probe adopted by Shwabedissen failed for $n_e > 6 \times 10^{17}$ m^{-3} [146], so the uncertainty of the measures might be higher than 30% getting closer to this limit. Similar considerations hold true for the electron temperature. The difference between numerical and experimental values is between 19% and 29% in face of a 20% uncertainty band of the measures. Nonetheless, T_e predicted by the *Global Model* is a volume averaged quantity, which is not subject to assumptions on spatial profiles as n_e. This is a possible justification of the mild difference between numerical and experimental estimations of T_e since measures are performed on the axis of the discharge [146]. In addition numerical results, both in terms of n_e and T_e, are affected by other assumptions as the sheath model. Expressions for Γ_{wall} and P_{wall} presented in Chapter 2 are quite general provided that secondary electron emission and elastic reflection have been modelled. In addition, the ICP reactors has no electrodes in contact with the plasma and is realized with materials whose behaviour in vacuum is well known (e.g., quartz) [105, 125]. Nonetheless the sheath model is expected to be another moderate source of uncertainty (in the order of 10% [14, 131]). In conclusion, the lumping strategy involving only $1s$ and $2p$ energy levels is proven to predict plasma density and temperature with an uncertainty lower than 30% regardless the gas. This is considered acceptable for a preliminary design tool as the *Global Model* in several applications concerning low pressure plasma discharges [172, 173].

The choice of the cross-section dataset affects significantly the numerical results. Plasma density presents a variance up to 32% considering krypton gas. Such a large value is not unexpected provided that the R_{chem} and P_{chem} terms (see Eq. 2.1) depend linearly form the cross-sections. Similar considerations hold true also for the electron temperature, the maximum variance of which, is registered again for krypton (value of 5%). According to the previous results, there is not a set of cross-sections that provides an output closer to experiments in general, namely it is not possible to identify a priori a dataset optimal for each scenario. For this reason, in Appendix A analytical expressions for the rate coefficients adopted in the highest and lowest density cases (i.e., the bounds of the uncertainty band associated to cross-sections) have been reported for each gas.

The analysis performed with the *Global Model* can give some insights into how transitions between excited species affect the dynamics of a plasma discharge. The main effect produced by radiative decay is the reduction of the population of excited species that can be ionized with a lower amount of energy with respect to neutrals. In other words, the radiative decay produces an increase of the P_{chem} term provided that collisional de-excitation and step-wise ionization reactions are less frequent. An increase in the reaction energy losses results in the reduction of the internal energy of the discharge $n_\varepsilon = \frac{3}{2} n_e T_e$. Regardless the gas type, n_ε decreases of 25-35% from the collisional case to the radiative-collisonal in response to an increase of P_{chem} of about 20-30%. Consequently, it is not surprising that the radiative decay causes an increase of T_e being the drop of n_e about 30-50% and of n_ε only 25-35%. Finally, the population of the excited species has been estimated to be lower with respect to electrons. Depending on the gas, n_{1s_M} and n_{1s_R} are up to one order of magnitude smaller than n_e; n_{2p} up to two. This is in agreement with previous analyses performed on ICP reactors [174, 115].

Chapter 4

Iodine fed HPT

This chapter is devoted to the analysis of the performance of a Helicon Plasma Thruster fed with iodine propellant. Iodine (I_2) propellant presents several advantages with respect to more traditional propellants like Xenon for electric propulsion systems. Iodine can be stored in solid state and being three time denser than Xenon [141] provides a higher total impulse for given volume: this feature extends the thruster's capability to larger total Delta-V missions, enabling new and different mission scenarios and interplanetary flights. Moreover, it can be stored at ambient condition [175], which means that no cryogenic system is required; its procurement cost is very low (e.g., 90% lower than Xenon [82]) and presents no transportation issue since the tank would not need a pressurization system. Solid Iodine has been already successfully tested in orbit as propellant for electric propulsion systems such as the the GIT of Thrustme [176] and T4i's REGULUS [12, 23].

In this chapter we show a numerical simulation of the iodine fed HPT $REGULUS$ [12]. A chemistry model compatible with low pressure ($< 50\ mTorr$) Helicon discharges working with iodine propellants such as $REGULUS$ has been considered and implemented in the GM shown in Chapter 2 in order to predict the plasma properties of the source chamber. A 2D3V Particle-In-Cell (PIC) [86, 87] code has been used for the analysis of the plume and *Magnetic Nozzle* effect, and the performance indicators such as Thrust and Specific Impulse have been computed as well.

4.1 Iodine chemistry model

The species present in the iodine discharge are molecular iodine I_2, atomic iodine I, singly-charged positive and negative atomic ions, namely I^+ and I^-, positive molecular iodine ions I_2^+, and electrons. Double-charged ions and excited species are not considered. Although the negative ions are not expected to have a great population compared to the positive ions, their influence may affects the diffusion process within the discharge chamber. Since in proximity of the walls a sheath is formed with an associated potential drop, the negative ions are repelled and confined into the bulk regions of the discharge. Nevertheless, in an electronegative plasma the flux of positive ions entering the sheath may be influenced by the negative ions, thus enhancing the wall losses [177]. Both electron impact reactions and heavy species collisions are considered in this work. An iodine molecule can

dissociate by electron impact through direct dissociation, dissociative ionization or attachment, with the latter being the main source of negative ions [177]. The latter can undergo detachment of the surplus electron by means of electron impact. Atomic iodine resulting from the dissociation, can either elastically scatter or ionize by electron impact producing atomic positive ions, which are subject to Coulomb scattering. Molecular iodine can either scatter elastically against the electrons or ionize by electron impact producing molecular ions, which can dissociate or undergo to Coulomb collisions. Concerning the heavy species collisions, the neutralization of positive and negative ions are considered. Moreover, positive atomic ions and molecular iodine are subject to charge exchange. Lastly, the surface recombination at the walls of the atomic iodine into molecular iodine is taken into consideration.
The species involved, the reactions considered and the related cross-sections are schematically summarized in Tab. 4.1. In Tab. 4.2, the energy thresholds related to the iodine transitions considered are reported.

Reactions	Reaction type	Cross-section
Electron impact		
$I_2 + e \longrightarrow I_2 + e$	Elastic scattering	[177]
$I_2 + e \longrightarrow I_2^+ + 2e$	Electron impact ionization	[177]
$I_2 + e \longrightarrow I^- + I$	Dissociative attachment	[177]
$I_2 + e \longrightarrow 2I + e$	Dissociation	[177]
$I_2 + e \longrightarrow I^+ + I + 2e$	Dissociative ionization	[177]
$I + e \longrightarrow I + e$	Elastic scattering	[177]
$I + e \longrightarrow I^+ + 2e$	Electron impact ionization	[177]
$I_2^+ + e \longrightarrow I^+ + I + e$	Dissociation	[177]
$I^- + e \longrightarrow I + 2e$	Detachment	[177]
$e + e \longrightarrow e + e$	Coulomb scattering	[178]
$I^+ + e \longrightarrow I^+ + e$	Coulomb scattering	[178]
$I_2^+ + e \longrightarrow I_2^+ + e$	Coulomb scattering	[178]
Heavy species collisions		
$I^- + I_2^+ \longrightarrow I + I_2$	Neutralization	[177]
$I^- + I^+ \longrightarrow 2I$	Neutralization	[177]
$I_2 + I^+ \longrightarrow I_2^+ + I$	Charge exchange	[177]
Surface reaction		Recombination Coeff.
$2I \longrightarrow I_2$	Surface recombination	[177]

Table 4.1: Reactions involved in the iodine plasma and related cross-sections.

Reactions	Energy thresholds [eV]	Reference
I_2 elastic scattering	$3\frac{m}{2M}T_e$	[97]
I_2 ionization	9.31	[177]
I_2 dissociative attachment	$1.5T_e$	[177]
I_2 dissociation	1.567	[177]
I_2 dissociative ionization	10.9	[177]
I elastic scattering	$3\frac{m}{M}T_e$	[97]
I excitation	0.95	[177]
I ionization	11.6	[177]
I_2^+ dissociation	2.1768	[177]
I^- electron detachment	4	[177]

Table 4.2: Energy thresholds associated with each reaction.

For each electron impact reaction considered i.e., ionization, elastic scattering, dissociative attachment, dissociation, dissociative ionization and detachment, the rate coefficients are computed as in Eq. 4.1:

$$K = \sqrt{\frac{2q}{m}} \int_0^\infty \varepsilon \sigma f_0 d\varepsilon \tag{4.1}$$

where q and m are the elementary charge and the electron mass; σ is the electron-impact cross-section for a generic transition, ε is the electron energy expressed in eV, and f_0 is the electron energy distribution function (EEDF) which is assumed to be a Maxwellian EEDF. The analytical expression of the Maxwellian EEDF reads [143],

$$f_0(\varepsilon) = 2\sqrt{\left(\frac{1}{T_e^3 \pi}\right)} \exp\left(-\frac{\varepsilon}{T_e}\right) \tag{4.2}$$

Regarding the heavy species collisions, i.e., neutralization and charge exchange, the rate coefficient is treated as in [179]. In order to predict the population density for every species and the electron temperature within the source chamber, the GM presented in Chapter 2 has been adopted.

4.2 Particle In Cell

The plasma expansion in the magnetic nozzle has been simulated by means of Starfish, a 2D3V axisymmetric fully kinetic Particle-In-Cell (PIC) code [180]. Ions, electrons and neutrals are modelled by means of macro-particles, and their dynamics is solved through the *leap-frog* Boris algorithm [181]:

$$\frac{\Delta \mathbf{v}^{t+1/2}}{\Delta t} = \frac{q}{m}\left(\mathbf{E}^t + \mathbf{v}^t \times \mathbf{B}\right), \quad \frac{\Delta \mathbf{r}^{t+1}}{\Delta t} = \mathbf{v}^{t+1/2} \tag{4.3}$$

where $\mathbf{r}^t$ is the particle position at time t with velocity $\mathbf{v}^t$, Δt is the time-step, $\mathbf{E}$ is the electric field, and $\mathbf{B}$ is the magnetic field. Assuming the RF power deposition in the acceleration stage to be negligible [182], allows the plasma potential field to be solved via the Poisson's equation of Eq. 4.4. This is achieved through an explicit Gauss-Seidel (SOR) scheme,

$$\epsilon_0 \nabla^2 \phi = -\rho \tag{4.4}$$

where $\rho = q(n_{I^+} + n_{I_2^+} - n_e)$ is the charge density, $n_{I^+}, n_{I_2^+}$ and n_e are the atomic and molecular ions and electron number density respectively. The electric field for the subsequent time-step is then evaluated from the potential as $\mathbf{E} = -\nabla\phi$. Regarding boundary conditions, the thruster outlet is given the reference potential $\phi_0 = 0$, while at the external boundaries, the following Robin condition is set:

$$\left.\frac{\partial \phi}{\partial \hat{\mathbf{n}}}\right|_b^t + \frac{\hat{\mathbf{n}}_b \cdot \mathbf{r}_b}{\mathbf{r}_b \cdot \mathbf{r}_b}\left(\phi_b^t - \phi_\infty^t\right) = 0 \tag{4.5}$$

where $\mathbf{r}_b$ is the vector distance between the centre of the thruster and the boundary face while $\hat{\mathbf{n}}$ is the unit vector normal to the surface and directed inwards, and ϕ_∞ is the plasma potential at infinity. In particular, the value of ϕ_∞ is updated each time step by means of Eq. 4.6:

$$\phi_\infty^{t+1} = \phi_\infty^t + \frac{1}{C}(I_{I^+B}^t + I_{I_2^+B}^t + I_{eB}^t)\Delta t, \tag{4.6}$$

where C is a virtual free-space capacitance and I_{jB}^n is the current of the j^{th} species leaving the open boundaries at time t. This method ensures the current-free condition of the plasma once at steady-state. For further details on the PIC methodology implemented, the reader is referred to references to [183, 184].

Regarding collisions, the following interactions are considered: electron-neutral elastic scattering, ion-neutral scattering, charge exchange, and Coulomb collisions. Collisions between different species are solved by means of the Monte Carlo Collision (MCC) methodology [185], whereas, collisions involving the same species are solved with the full Direct Simulation Monte Carlo (DSMC) [186] method. Anomalous transport is included via means of an equivalent enhanced collision frequency, based on the empirical model of Bohm [184], $\nu_{an} = 0.01 \cdot \omega_{ce}$, where ω_{ce} is the gyro-frequency.

4.3 Validation against the REGULUS thruster

Measurements performed at the *High Vacuum Facilities* of the University of Padova over REGULUS, the T4i thruster, have been considered [83] in order to validate the methodology proposed in Sec. 4.1-4.2. The experimental facility consists of a vacuum chamber of radius 0.3 m and length of 2 m, mantained at 10^{-5} mbar. The iodine propellant has been introduced in the source chamber with a massflow of 0.1 mg/s, through a tailored fluidic subsystem. The latter consist of a tank which has been maintained at the iodine sublimation temperature by means of heaters, and a manifold enclosing the flow controllers [83]. The thruster has been connected through a coaxial line to the power generator consisting of a Spin HFPA-300 linear amplifier (1.8-30 MHz, power up to 300 W) driven by an HP 8648B signal generator [83]. However, the RF frequency was kept to 2 MHz and the input power in the range 15-60 W. Concerning the performance characterization, a thrust balance tailored for small-to-medium size thrusters [187], has been used. Voltage and current have been measured with a RF probe [11]. The measurements uncertainty associated to

the thrust is about 15-20%, while the uncertainty associated to the power and massflow are respectively of 10% and 10-15%.
Concerning the thruster's parameters used for setting up the GM and PIC simulations, they are synthetically summarized in Tab. 4.3.

Parameter	Value
Diameter	15 mm
Length	80 mm
Peak magnetic field	600 G
Input power	10, 30, 50 W
Base pressure	10 mbar

Table 4.3: Input parameters of the GM + PIC used to simulate the REGULUS HPT.

The GM and the PIC described respectively in Chapter 2 and Sec. 4.2 have been used to simulate the iodine fed HPT according to the chemistry model presented in Sec. 4.1. For what concerns the GM, the species of interest are singly-charged atomic (positive and negative) and molecular (positive) ions, neutral atoms and molecules at the ground state, and electrons. Regarding the PIC, the same species as the GM are tracked, except for negative atomic ions. This is reasonable as I^- population predicted with the GM is negligible with respect to the population of positive ions ($\sim$ 3 order of magnitudes) and considering that at the source's outlet the potential drop associated with the magnetic nozzle region confines them back to the chamber. In Fig. 4.1, the number density of the molecular and atomic iodine ions, and the electrons are shown. It can be noticed that generally the number density of atomic ions are greatly larger with respect to the molecular ions (~2-3

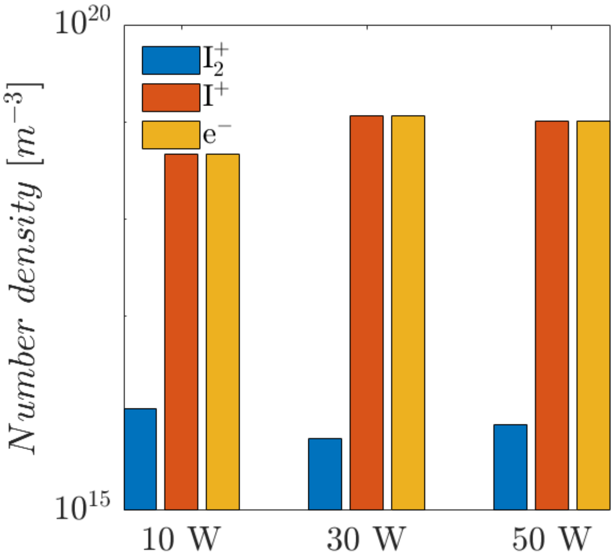

Figure 4.1: Number density of the I_2^+, I^+ and electrons versus the input power P_w predicted by the GM.

order of magnitudes), and it is comparable to the electron density therefore respecting the plasma neutrality. Furthermore, increasing power from 10 to 30 W the population density of I_2^+ drops as the dissociation mechanisms by electron impact are enhanced with increasing electron temperature. Nevertheless, at 50 W a slight increase is registered.
The PIC simulations were conducted for a time interval of approximately 9 μs, after which steady state condition was achieved. Fig. 4.2 shows the evolution of the total species energy in the domain (normalised by the steady-state value), as well as the plasma potential at infinity for the $P_w = 50$ W case. It is quite evident how the convergence speed of atomic ions and electrons is quite similar, which is mainly related to the coupling between the electrons and the ion beam; molecular ions are characterised by a slightly slower transient. This is due to their higher mass, which finally results in a lower acceleration.

In Fig- 4.3, the envelope of performance, namely thrust T and specific impulse I_{sp}, is depicted as a function of the input power P_w. Three different operating powers were simulated and compared to the experimental measures. It can be seen that the numerical prediction of thrust always lies within the experimental uncertainty, and that the measured points also lie within the assumed numerical error. The estimated specific impulse I_{sp} also agrees well, with the maximum deviation around 15-20 %.

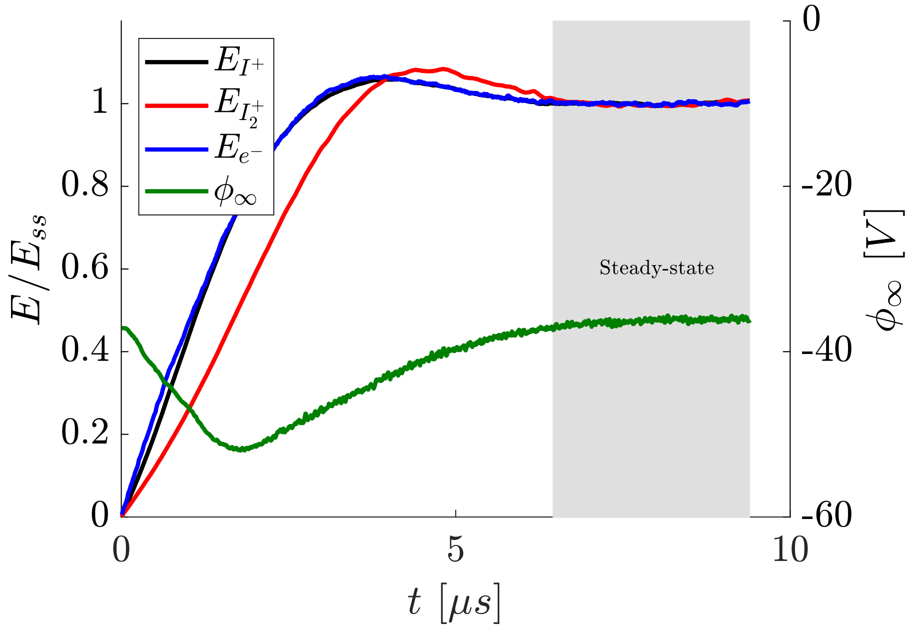

Figure 4.2: Normalised energy convergence at $P_w = 50$ W and electric potential at infinity.

In Fig. 4.4 the contributions of the different species to the total thrust are shown with respect to the input power. It can be noticed immediately how molecular iodine (both neutral and ionised) has little contribution to the overall HPT performance. When operating the thruster at low power (i.e. $P_w = 10$ W), the contribution to the propulsive performance is almost equally split among neutrals and ions. This changes as the power increases, resulting in the ions providing more than 80% of the final thrust. Lastly, the

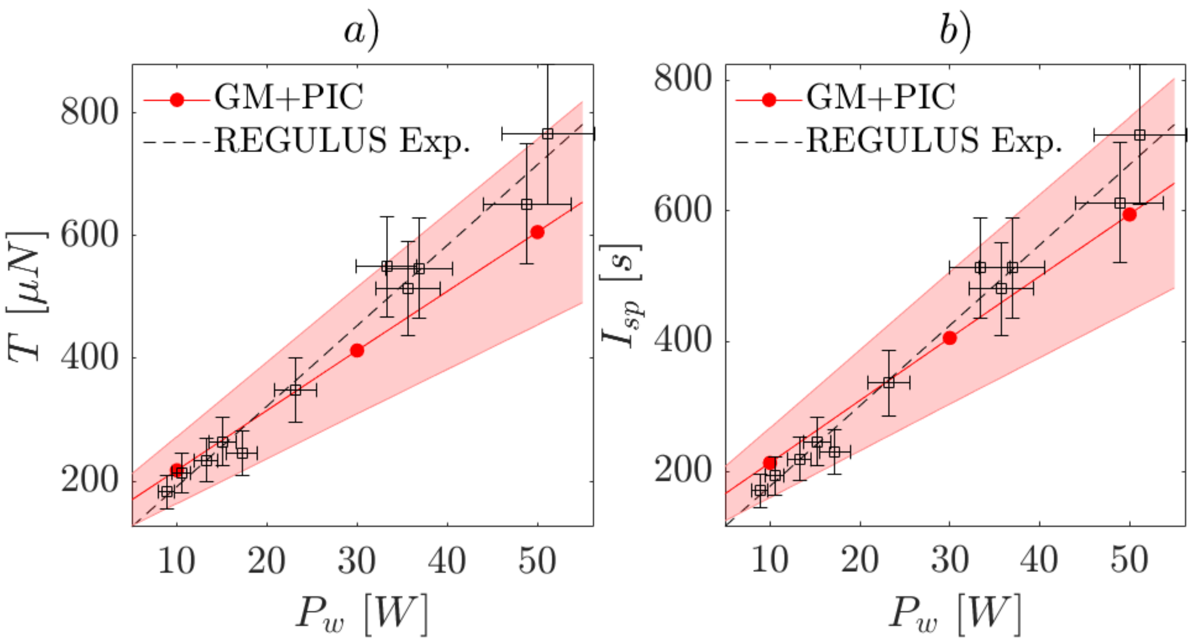

Figure 4.3: Performance predicted by the proposed numerical strategy, namely *GM* + *PIC*, compared against the experimental measures of *REGULUS*. From left to right, a) is the thrust T and b) is the specific impulse I_{sp}.

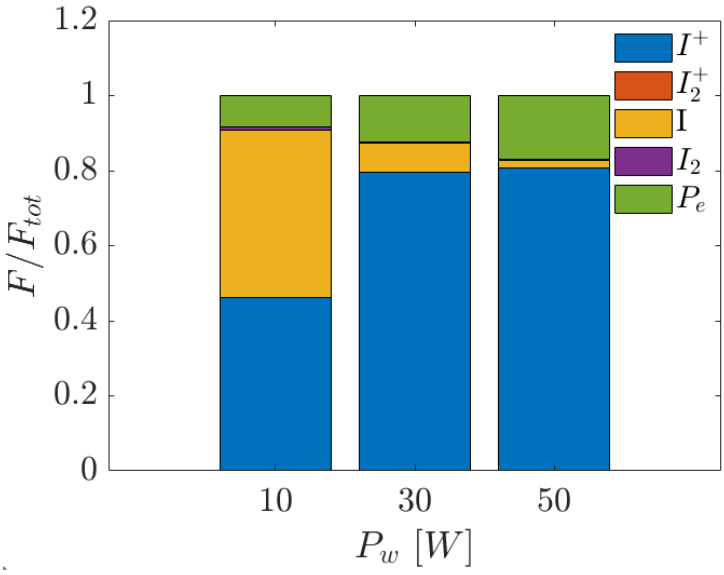

Figure 4.4: Thrust contributions at different power levels.

electron pressure term (P_e) consistently grows as the operating power increases from 10 W to 50 W, due to the higher electron temperature at the inlet of the magnetic nozzle.

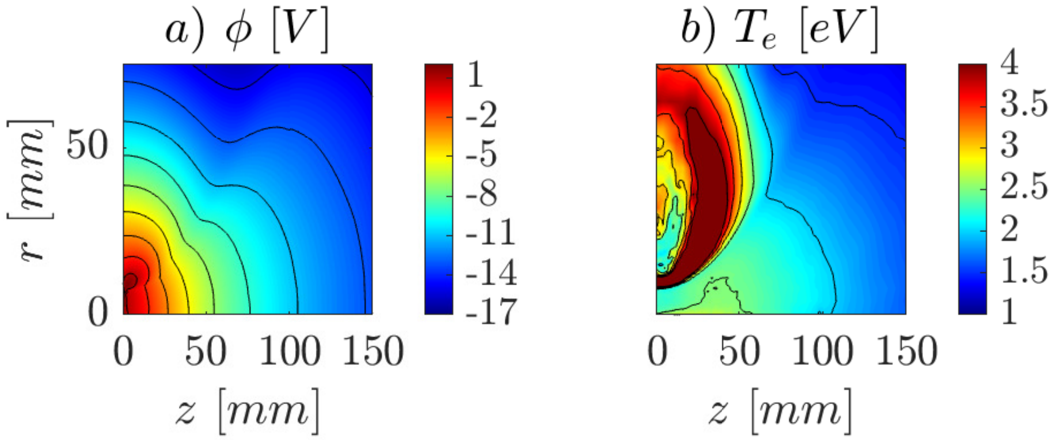

Figure 4.5: 2D profiles of a) plasma potential b) electron temperature computed with the PIC methodology.

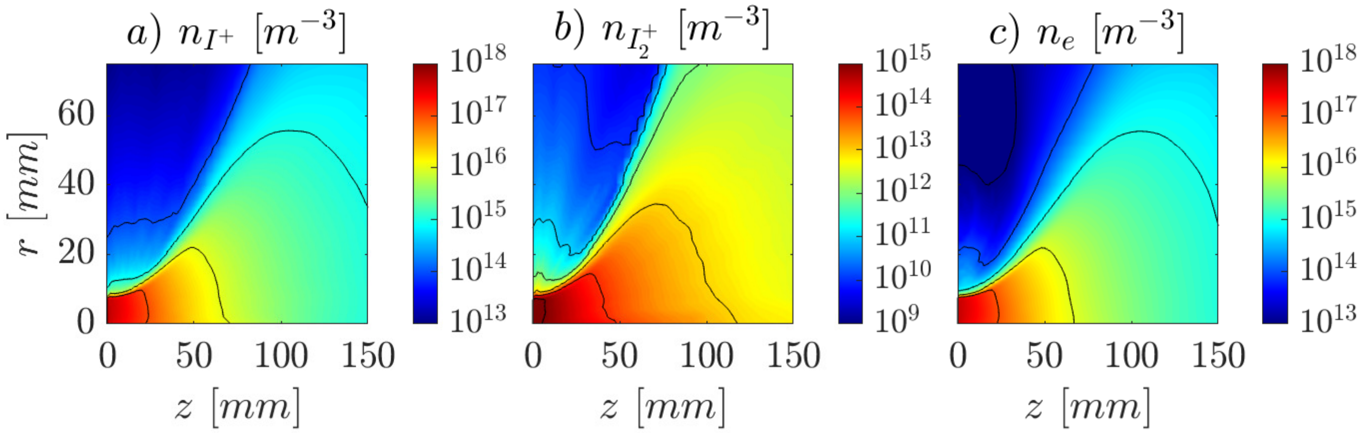

Figure 4.6: 2D profiles of a) atomic ions b) molecular ions c) electrons computed with the PIC methodology.

Fig. 4.5-4.7 display the 2D profiles of the number density n_j for each species considered, the electrostatic potential ϕ and the electron temperature T_e. 2D fields are evaluated at operating power $P = 10$ W, since the higher collisionality at this level highlights important features. In Fig. 4.5 (a), the presence of an ion-confining potential peak is clearly visible. The related electric field topology is a key element in the confinement of ions, since it forces

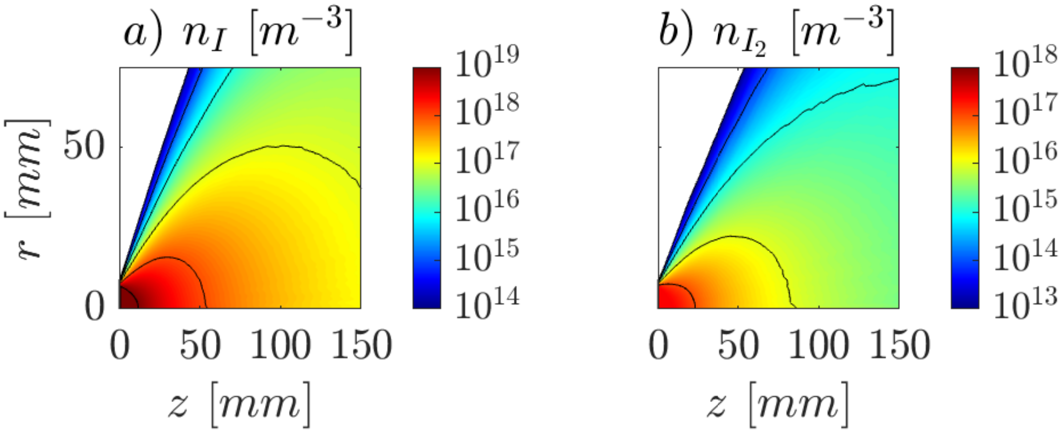

Figure 4.7: 2D profiles of a) atomic neutrals b) molecular neutrals computed with the PIC methodology.

their trajectories into the magnetic nozzle. Fig 4.5 (b) shows the electron temperature distribution. A radial wing of highly-energetic electrons is present outside of the outermost field line connected to the thruster outlet, however, as evinced from Fig 4.6 (c), such collection of particles only represents a small fraction of the overall electron population as it coincides with the high energy tail of the Maxwellian distribution. Since the number density of atomic ions (Fig. 4.6 (a)) exceeds the molecular one (Fig. 4.6 (b)) of several orders of magnitude ($n_{I^+} \sim 10^{18}$ and $n_{I_2^+} \sim 10^{15}$) it is fairly reasonable to assume that the MN structure is mainly sustained by the atomic iodine ions and electrons. It is important to note also the pronounced secondary expansion of I_2^+, whose trajectory is less affected by the potential field due to their heavier nature. Fig. 4.7 shows both the atomic and molecular neutral fields, which are consistent with a free molecular expansion.

Chapter 5

Air-breathing HPT

The *Air-Breathing Electric Propulsion* (ABEP) technology is an enabler for unlocking innovative space mission scenarios such as Very Low Earth Orbit (VLEO) missions which are beneficial for remote sensing and telecommunications. The main challenge posed by these missions is due to the residual atmosphere that drags down the satellite at lower altitudes. The mission lifetime can be dramatically increased employing the ABEP systems, which consist of an electric propulsion system combined with an intake that collects the thermosphere's particles (e.g., molecular nitrogen N_2 and atomic oxygen O) which in turn are employed as propellant. The most evident advantage of such a system is that the satellite does not need a propellant tank as the propellant is retrieved directly from the atmosphere[188]. In Fig. 5.1 the schematic of an ABEP system based on the HPT technology is reported. The intake guides the particles into the discharge channel of the thruster. In the latter, the gas particles are ionized and accelerated to produce thrust.

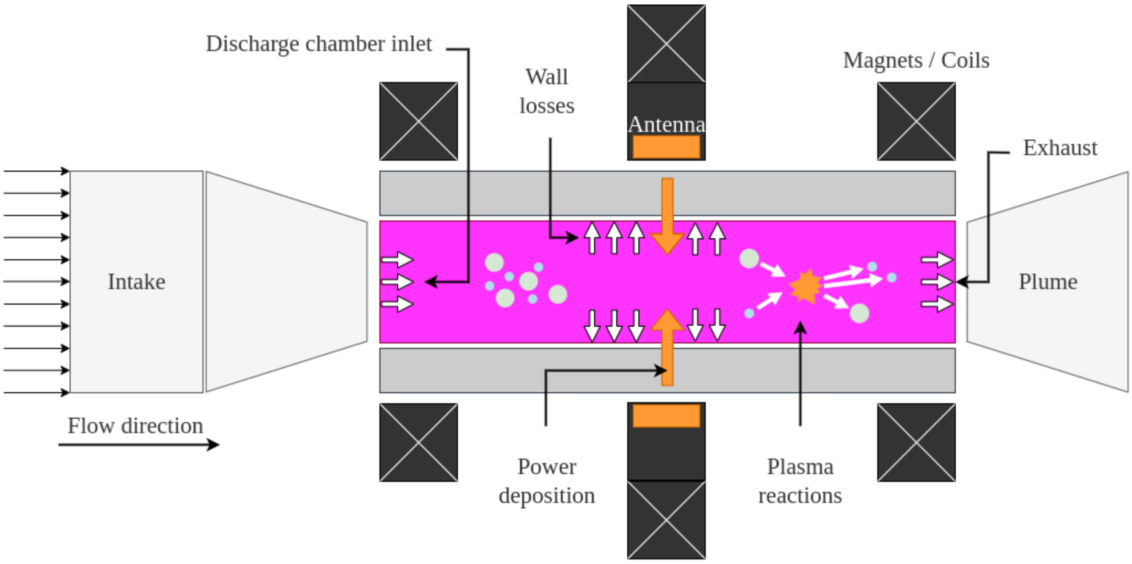

Figure 5.1: Schematics of the ABEP-HPT system and main phenomena occurring within the discharge chamber.

Several research groups are actively working on ABEP systems; among the main ABEP projects it is worth reporting the ESA's RAM-EP [189], MABHET [190] held by Busek Co., ABIE [191] which is being developed at JAXA, and DISCOVERER [192] at the University of Stuttgart.

In order to assess the feasibility of a ABEP system powered by a HPT an accurate chemistry model is needed to assess the performance at varying altitudes and air compositions. Atmospheric particles are not homogeneous and vary significantly with altitude [193] which makes it difficult to predict the thruster performance. In this chapter, a chemistry model suitable for ABEP applications is shown. The model have been implemented in the GM presented in Chapter 2 and validated against numerical simulations taken from literature. A proper validation against experimental data has not been possible due to the lack of experimental measurements in the state-of-the-art. For this reason, the setup of an experimental campaign on an actual ABEP based on the HPT technology developed at the University of Stuttgart [78] is proposed in Sec. 5.3. The experimental activities currently undergoing are presented. It is worth noting, that at the moment the experimental campaign has not been concluded yet, therefore only the setup and calibration of the measurement systems are presented.

5.1 Air chemistry model

Air is a mixture of several gases with a composition that greatly varies with altitude. As a consequence, some species and/or reactions shall be of importance depending on the altitude at which the HPT is operating. In Fig. 5.2, the density variation with respect to the height from sea level is shown for the main species present in air, i.e., oxygen and nitrogen in both atomic (O, N) and molecular (O_2, N_2) form [194]. Nonetheless, other species may be produced within the ionization chamber as a result of heavy particles collisions. In fact, molecules like nitric oxide (NO), nitrogen dioxide (NO_2) and nitrous oxide (N_2O) may have a non-negligible effect to the plasma dynamics within the thruster, especially in lower orbits, where the atmosphere is denser. In this work, the species considered are electron, atomic and molecular neutral species, namely N,N_2,O,O_2,NO,N_2O,NO_2, excited state, and single-charged atomic and molecular ions. In Fig. 5.3, a schematic of the reactions involved in the model is shown. A and B represent two generic interacting species. Positive and negative ions are respectively indicated with apex $^+$ and $^-$ while * represents an excited species. Transitions represented in red correspond to collisions between heavy species, whereas blue transitions represents electronic collisions. In Tab. 5.1 a summary of the chemistry model considered is shown, and the complete set of reactions and related rates is presented in Appendix B as well as the cross-sections employed in this work. It

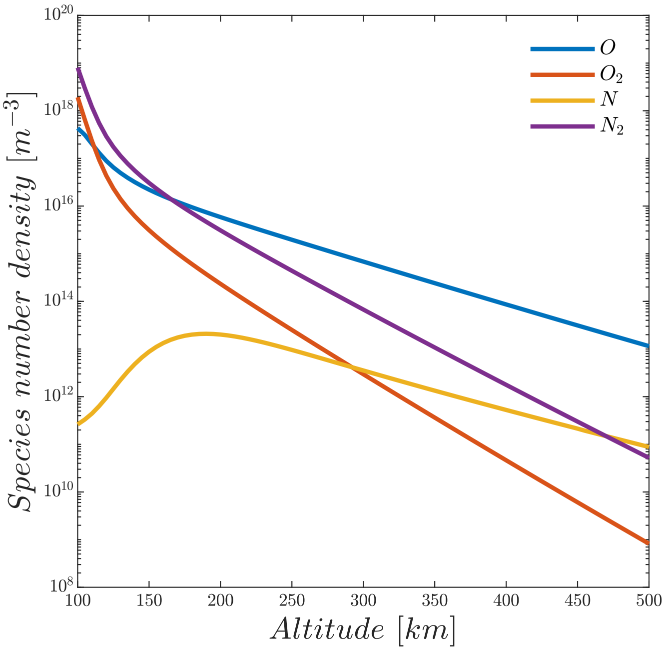

Figure 5.2: Atmospheric species' number density as a function of the orbit altitude (latitude = 38.91° and longitude = 77.04°), NRLMSISE-00 atmospheric model: F10.7, Ap = 15, moderate solar activity [194].

is worth noting that in the present model the excited states of oxygen and nitrogen are assumed to radiative decay toward the ground states immediately after their generation and therefore they are considered as a mere lumped sink term in the GM energy balance.

Table 5.1: Summary of the reactions involved in the air chemistry model.

#	Reaction	Name
1	$e + A \longrightarrow A + e$	Atomic Elastic Scattering
2	$e + A \longrightarrow A^* + e$	Atomic Excitation
3	$e + A \longrightarrow A^+ + e + e$	Atomic Ionization
4	$e + A^- \longrightarrow A + e + e$	Atomic Detachment
5	$e + A^+ \longrightarrow A$	Atomic Neutralization
6	$e + A \longrightarrow A^-$	Atomic Attachment
7	$e + AB \longrightarrow AB + e$	Molecular Elastic Scattering
8	$e + AB \longrightarrow AB^* + e$	Molecular Excitation
9	$e + AB \longrightarrow AB^+ + e + e$	Molecular Ionization
10	$e + AB \longrightarrow A + B^+ + e + e$	Molecular Dissociative Ionization
11	$e + AB \longrightarrow A + B^-$	Molecular Dissociative Attachment
12	$e + AB \longrightarrow A + B + e$	Molecular Dissociation
13	$e + AB^+ \longrightarrow A + B^+ + e$	Molecular Ion Dissociation
14	$e + AB^+ \longrightarrow AB$	Molecular Neutralization
15	$e + AB \longrightarrow AB^-$	Molecular Attachment
16	$e + AB^+ \longrightarrow A + B$	Molecular Dissociative Neutralization
17	$e + AB^- \longrightarrow AB + e + e$	Molecular Detachment
18	$A^+ + B \longrightarrow A + B^+$	Charge Exchange
19	$A^+ + B^- \longrightarrow A + B$	Mutual Neutralization
20	$A + B \longrightarrow AB$	Recombination
21	$A + B^+ \longrightarrow AB^+$	Ion recombination
22	$A + B^- \longrightarrow AB + e$	Associative Detachment
23	$A^+ + B^- \longrightarrow AB$	Associative Neutralization

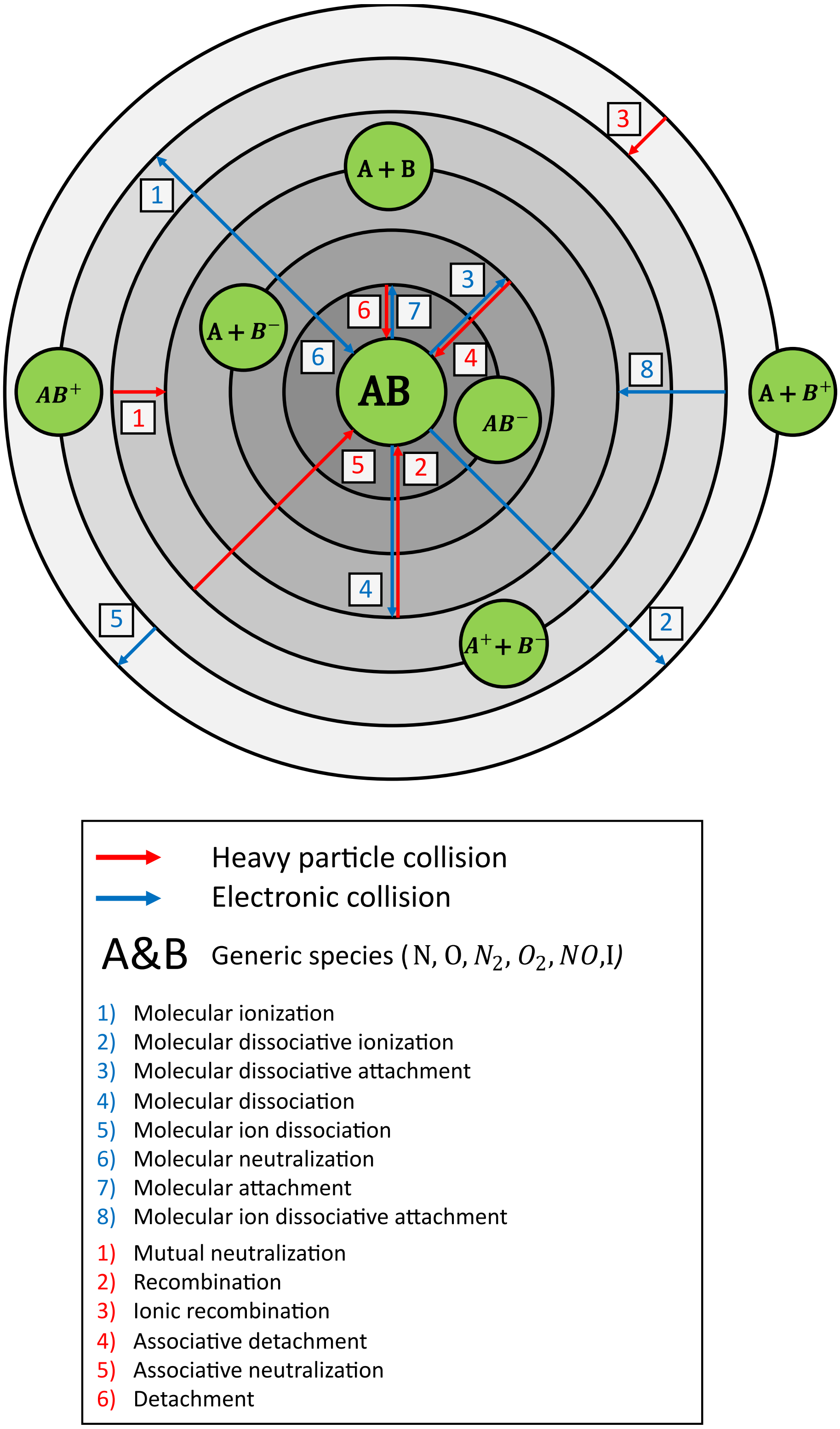

Figure 5.3: Reaction set considered for an air fed HPT.

5.2 Verification of the GM

For the sake of verification the GM with the chemistry model of Sec. 5.1 have been employed and compared against the simulations of an ABEP system presented in the work of Taploo [195]. The simulation case consists in a spacecraft orbiting in VLEO between $80 - 110\ km$. A one meter long cylindrical discharge chamber has been considered and the simulation time is about $0.125\ ms$ i.e. the average time needed for a particle to traverse the discharge channel at those orbital altitudes. It is worth noting that Taploo assumed the mean electron energy within the discharge rather than solving for the energy balance [195]. Different configurations of orbit altitude and mean electron energy in the discharge were considered. The ranges considered are respectively $80, 90, 100$ and $110\ km$ for the altitudes and $1 - 200\ eV$ for what concerns the electron energy. In particular, two specific configurations have been selected for the verification purpose, namely I) at orbital altitude of $80\ km$ and mean electron energy of $30\ eV$, and II) at orbital altitude of 100 km and mean electron energy of $100\ eV$. In Fig. 5.4-5.5, the density evolution for each

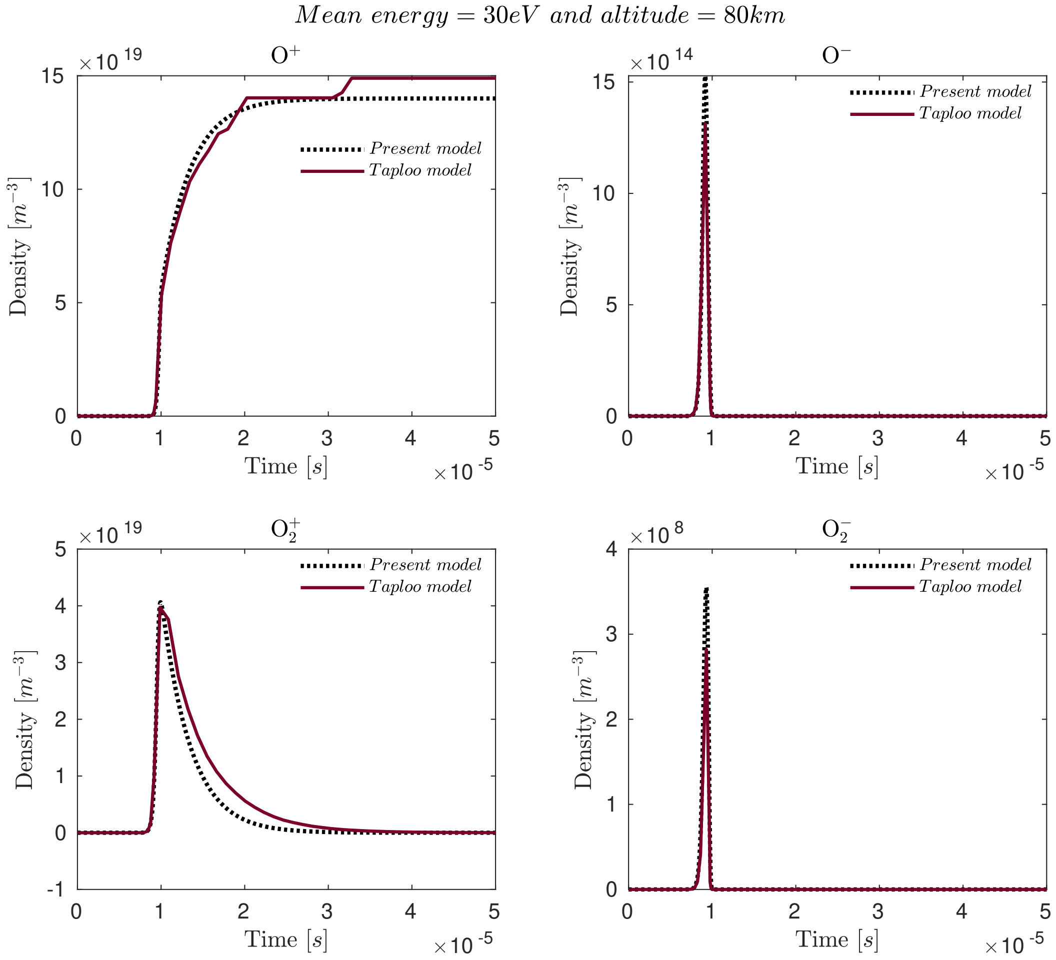

Figure 5.4: Comparison against Taploo's results [195] for a mean electron energy of 30 eV and 80 km altitude. Plots are related to density of O^+, O^-, O_2^+ and O_2^-

species involved in the model in the first configuration are shown and compared against the numerical predictions of Taploo, whereas in Fig. 5.6-5.7, the ones related to the second configuration are shown as well.

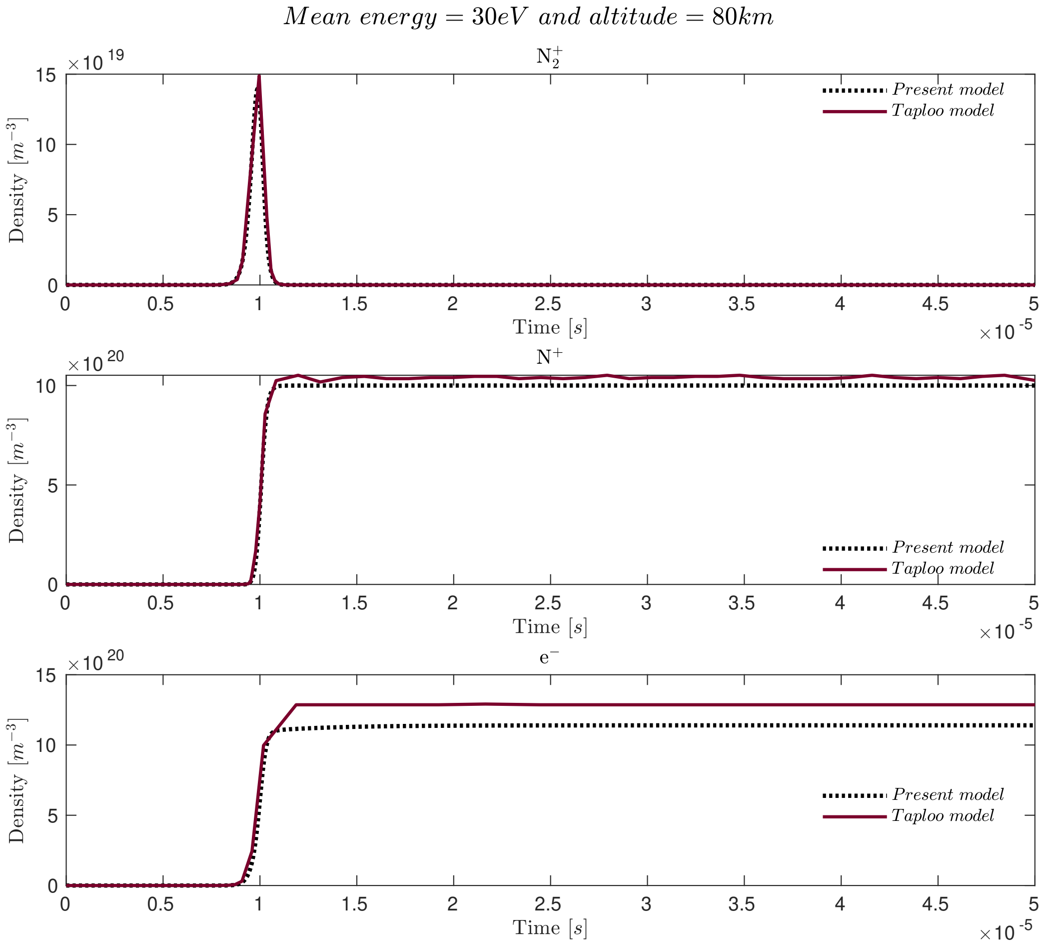

Figure 5.5: Comparison against Taploo's results [195] for a mean electron energy of 30 eV and 80 km altitude. Plots are related to density of N_2^+, N^+ and e^-

The model shows a good agreement with Taploo's predictions in terms of physical trends. Nevertheless the registered deviation for each species density never goes above 25%. The difference between the two models may be linked to several factors. First, in the chemistry model proposed in this work the dissociation, excitation and ionization of molecular nitrogen are considered whereas Taploo does not. The same applies for the excitation of atomic oxygen and several elastic scattering reactions of both atomic/molecular oxygen and nitrogen. In addition, in Taploo's work no further details have been given on the diffusion assumptions employed which may be an additional source of deviation. Finally, the GM equations may be solved with different ODE strategies which may add an additional source of deviation on the results. Some interesting physical consideration may be drawn analysing the GM simulations for both the configurations considered. The most evident physical consideration is that different altitudes and therefore different in-

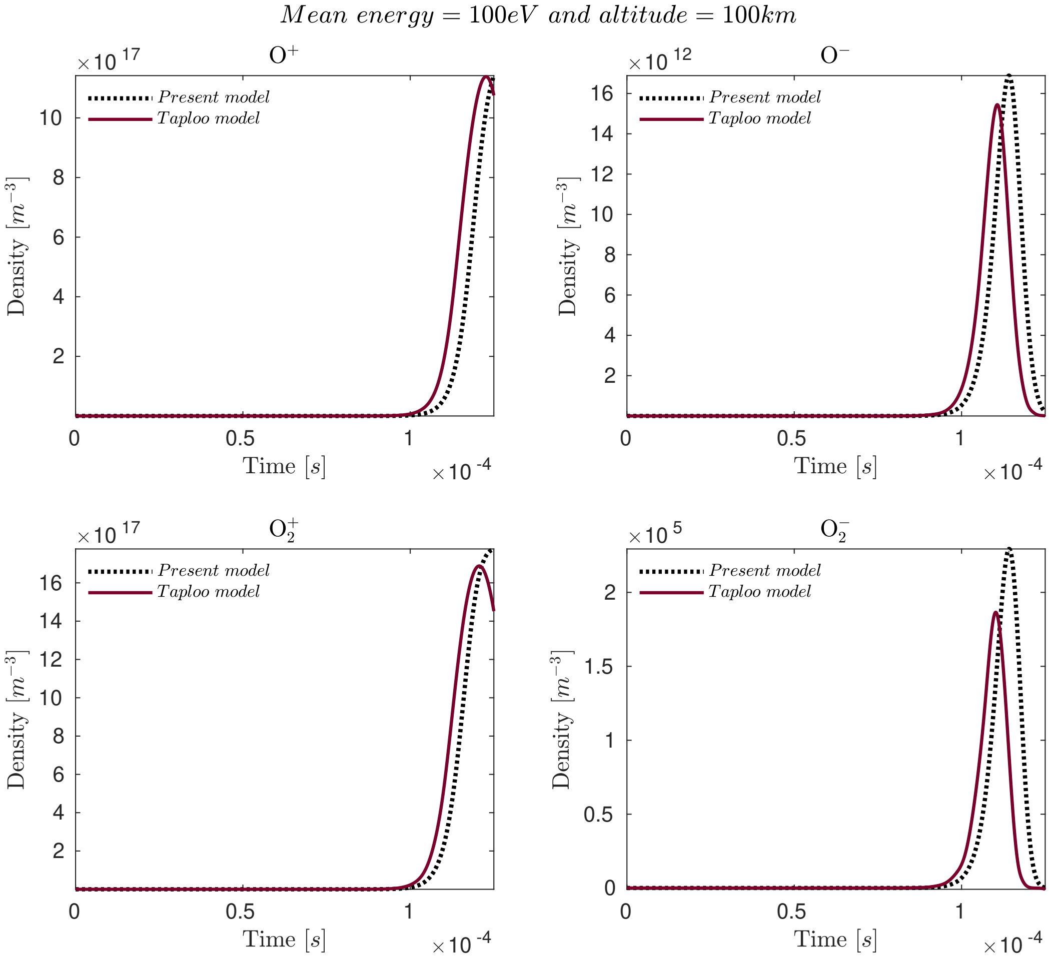

Figure 5.6: Comparison against Taploo's results [195] for a mean electron energy of 100 eV and 100 km altitude. Plots are related to density of O^+, O^-, O_2^+ and O_2^-

flow air mixtures lead to dramatically diverse plasma compositions. In fact, it can be seen as in the second configuration the population of ionized molecules is proportional to the one of atomic ions, whereas in the first configuration the latter have a population density one order of magnitude greater with respect to molecular ions. This is of great importance since a high presence of molecular species in plasma plumes may be associated with lower propulsive performances as it has been discussed in Sec. 4.3. Nevertheless, a proper validation against experimental data is required for validating the GM and the physical phenomena predicted.

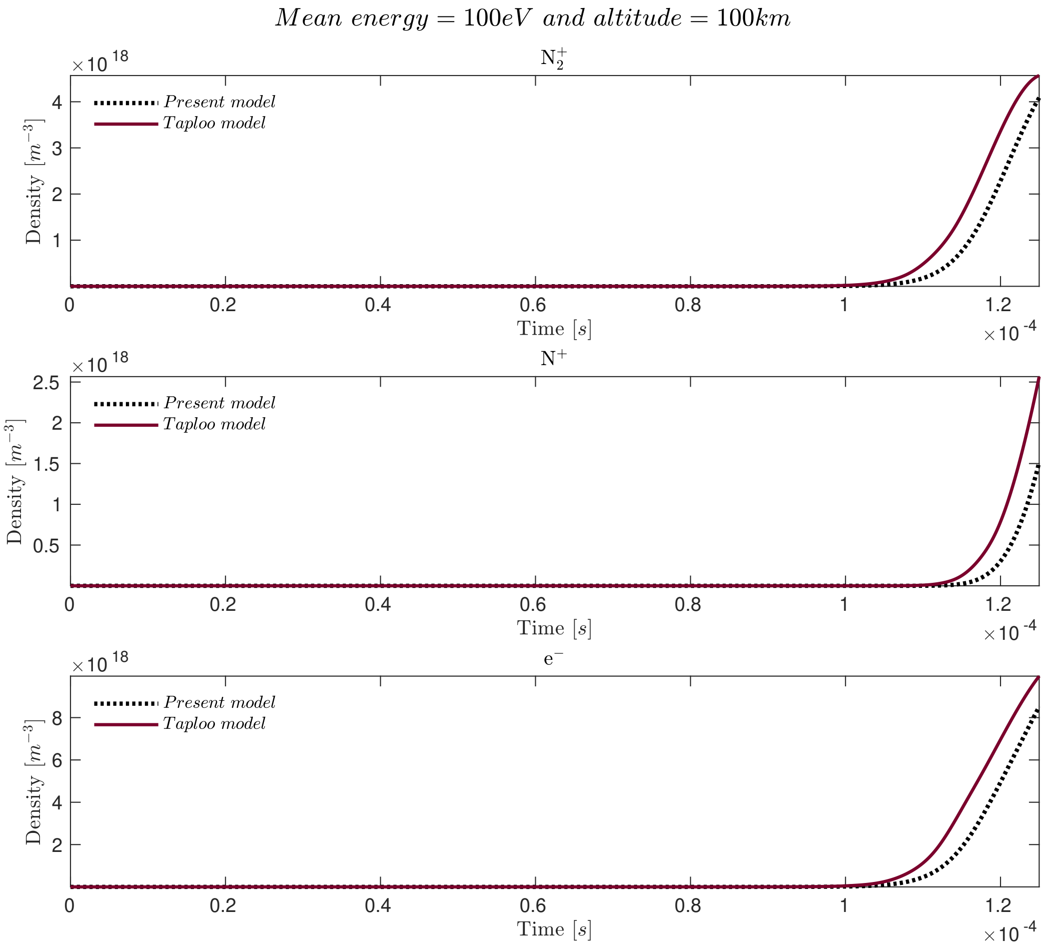

Figure 5.7: Comparison against Taploo's results [195] for a mean electron energy of 100 eV and 100 km altitude. Plots are related to density of N_2^+, N^+ and e^-

5.3 Experimental activities for validation of the GM

For the sake of validating the air chemistry model presented in Sec. 5.1, an experimental investigation is currently being carried out on an ABEP employing a HPT developed at the Institute of Space Systems (IRS) of the University of Stuttgart (see Fig. 5.8) in the frame of the EU-funded DISCOVERER project [192]. Two measurement methods have been adopted. First, the plume's momentum-flux is measured through a torsional-pendulum in order to obtain the thruster's performance parameters such as thrust and specific impulse. Then, a B-dot probe developed by Romano [192] has been calibrated to allow three-axis-magnetic-induction measurements of time-varying magnetic fields in order to characterize the propagation of *Helicon* waves within the thruster. In this section, the set-up and calibration of the two probes are presented. Future measurements resulting from such calibrations will allow the validation of the numerical models presented in this work.

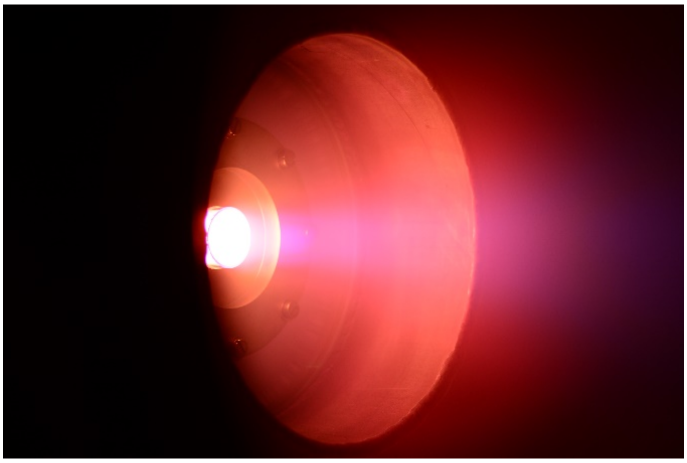

Figure 5.8: Firing test of the HPT of University of Stuttgart.

5.3.1 IRS RF Helicon-based Plasma Thruster Design

The HPT developed at IRS has undergone an ignition test campaign, using successfully argon, nitrogen and oxygen as propellants. In Fig. 5.9, the HPT concept is shown [192]. The schematic presents all the features necessary for the implementation of a thruster that is compatible with an ABEP system for a VLEO mission. The primary components of the thruster are: propellant injector, discharge channel, birdcage antenna, Faraday shield, external solenoid, support structure(s) such as frequency fine-tuning mechanism. Being still a laboratory model, see Fig. 5.10, the thruster is mounted externally to the vacuum chamber for flexibility and passive cooling, facilitating the experiments.

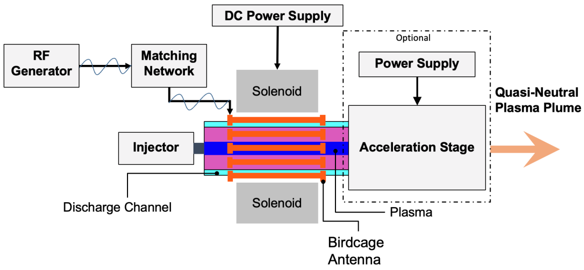

Figure 5.9: HPT concept for an ABEP system [78].

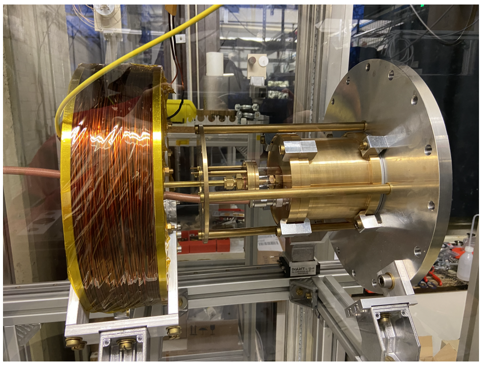

Figure 5.10: HPT lab model with solenoid on the left [78].

Within the HPT, the gas is delivered into the discharge channel through an injector acting at simulating the intake. The discharge channel is surrounded by a birdcage antenna [196] where the ionization of the propellant takes place. The required input power to the antenna is given by the RF generator through a matching network. The main peculiarity of the birdcage antenna lies in the fact that it ensures a good impedance matching and can couple Helicon waves [197]. The external solenoid is responsible of producing the necessary magnetic field for both confinement within the discharge and for generating the magnetic nozzle effect at the outlet. The purpose of the RF auto-matching network is to match antenna impedance to the RF-generator's one in order to maximize the coupling efficiency. The currently developed laboratory model carries an optimized antenna, operating at a frequency of 40.68 MHz delivered by the RF generator and the matching network. The discharge channel has an inner diameter of 37 mm. The external solenoid produces a maximum magnetic field of 70 mT at a current of 15 A. The support structure is made of brass to mitigate the effects of Eddie currents due to RF fields as well as the interactions with the external magnetic field by the solenoid. The Faraday shield acts as an isolation of the EM fields by the antenna with the ambient environment. The thruster is operated at powers of 50-100 W, with a maximum of 300 W tested so far. More details on the design and the operational envelope are provided in [196],[198],[199].

5.3.2 Momentum Flux Probe Design

A momentum flux probe (MFP) has been employed to characterize the plasma plume of the thruster. Thrust can be extracted indirectly by measuring the momentum flux on a target placed in the exit plane of the HPT. Thrust is expected to be in the range of µN with the maximum to be close to 1 mN [200]. The probe type employed is a torsional pendulum, featuring a baffle plate as a target. The selection of this measurement approach is mainly due to the fact that the HPT is mounted externally to the vacuum chamber. Moreover, this type of pendulum features gravity independence, high sensitivity and sufficient stability and ease of implementation.

The design of the MFP features two main parts: the support structure and the pendulum as shown in Fig. 5.11. The support structure act as the interface between the pendulum and the moving table of the test facility. The pendulum (1) is not fixed directly on the support structure but there is an intermediate plate (4) as interface. The displacement sensor (2) is mounted on the support structure made of aluminium profiles (3). The tilt sensor (5) is mounted as close as possible to the pendulum on the interface plate. Tilt control is achieved using the support structure by adjusting the screws (6). Moreover, the design incorporates vibration damping to counteract the vibrations acting on the test facility. This is achieved by using four dampers (7). To improve the damping, a brass plate (8) is used to increase the weight. The pendulum is the main part of the MFP (see Fig. 5.12). It features all the moving parts as well as the connection interface (bearing and sockets) to the support structure. The L-shape design facilitates the moving range of the probe closer to the thruster's exit plane while keeping the rest of the parts not only protected from the plasma plume but also not altering its magnetic field. The length of the shaft is 150 mm and is mounted on the arm using a dowel pin and a fitting screw. The main beam is set to 200 mm, facilitating the detection of low momentum flux. The target material is required to have a high absorption rate for recording an accurate thrust measurement, since the reflected particles can add additional momentum. For this purpose, two candidate materials were considered: graphite which has a low sputtering yield and high temperature resistance [201] and micanite which has been used previously in Helicon thrusters experiments [202]. For the first iteration, graphite was chosen. The

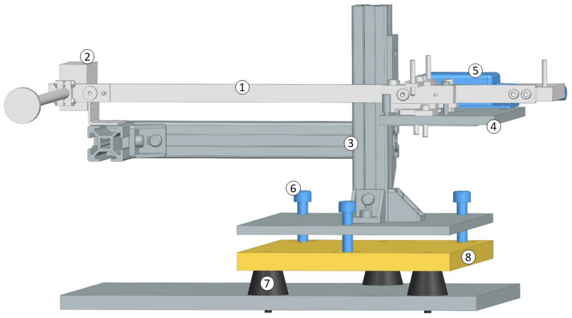

Figure 5.11: MFP design: Light grey (technically not part of mounting structure): Pendulum (1) and displacement sensor (2), Grey: Aluminium parts and Bosch profiles (3), Blue: Tilt control (sensor 5, screws 6), Black: Dampers (7), Yellow: Brass plate (8) [78].

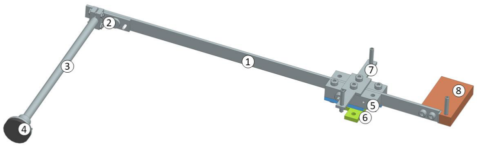

Figure 5.12: MFP pendulum design: main beam (1), clamp (2), shaft (3), target holder & target (4), mounting (5), sockets (blue - moving, green - fixed) (6), balancing mount (7), counterweight (8) [78].

target is glued on a holder which is then fixed on the main beam by two set screws. Due to the shape of the arm, the centre of gravity is not aligned with the rotational axis. For this reason, a counterweight and balancing mounts were added on the pendulum, making it possible to balancing the pendulum post-manufacturing and -assembling. This keeps the design flexible in case of a target change. The counterweight is made of copper and is attached on the aluminium support structure via a PVC part to avoid galvanic erosion. The bearing chosen and mounted on the rotational point of the probe is a frictionless flexural pivot bearing which is used both as a bearing and as a provider of restoring force. The selected bearing can withstand all axial and radial loads by the pendulum as well as minimizing the spring constant for the set lever and thus resolution.

As mentioned, the probe features a target that is guided into the plume and thus measuring a small part of it. This results in a momentum flux reading for a given position. By moving the probe inside the plume and perpendicular to the thruster's axis, a radial profile of the momentum flux can be obtained. Integrating the momentum flux recordings, a value of the total thrust can be extracted. This measurement technique was selected over the full plume detection due to the requirement of using a big target in diameter. This has been considered impractical since a big target would eventually influence the discharge behaviour, increasing the required distance from the exit plane while it would increase the gravity influence at the same time. An assembled version of the probe is shown in Fig. 5.13. To protect all parts from the plasma plume and avoid any unwanted deflection the MFP incorporates a shield, leaving only the target plate in direct contact. This is shown in Fig. 5.14 where the MFP is attached on the moving platform inside the vacuum chamber.

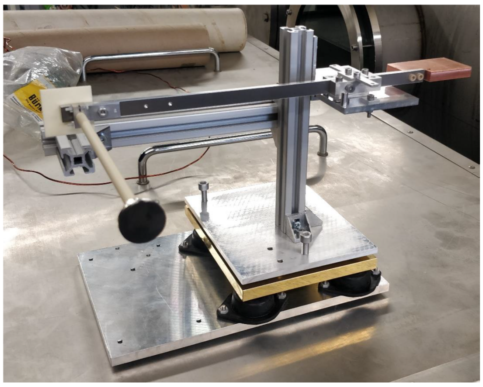

Figure 5.13: Momentum Flux Probe assembly without electrostatic comb for calibration and sensors [78].

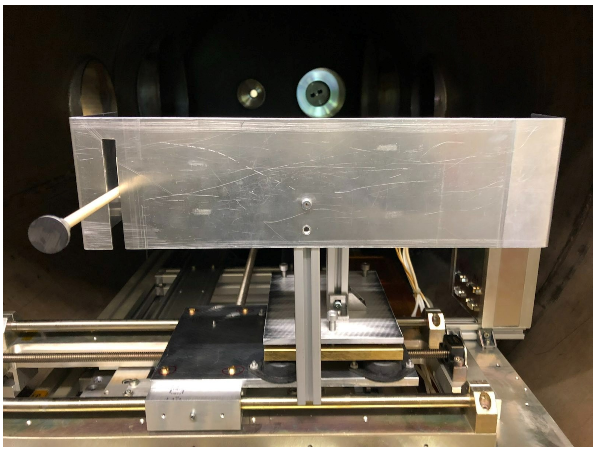

Figure 5.14: MFP with shield mounted on test facility [78].

The MFP design is based on a maximum expected measured thrust close to 1 mN in comparison with thrust levels of existing thrusters [203]. Aluminium is the primary choice as used material on MFP's parts in order to avoid any influence on the discharge region due to magnetism [204]. Other materials such as brass, copper, alumina and plastics (e.g. PTFE or PVC) are also used.

5.3.3 Momentum Flux Calibration

Calibration of the MFP is done through a known electrostatic force, which is a frequently employed technique for measuring forces in the range of micro-newtons. This is done by using an electrostatic comb (ESC) as shown in Fig. 5.15. It consists of two metal plates with fins in a comb-like configuration. By applying a certain voltage to the two parts, they start attracting each other with a force independent of the exact distance between the plates, while being proportional to V^2 [205]. The target's diameter is 20 mm to resolve the HPT plume while the plume diameter is estimated around 150 mm, at the measurement position. Thus, the expected force on the target is calculated about 17.8 µN, assuming

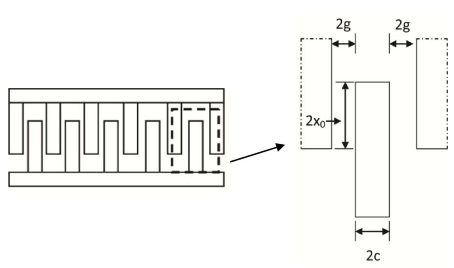

Figure 5.15: Illustration of the ESC geometry [78].

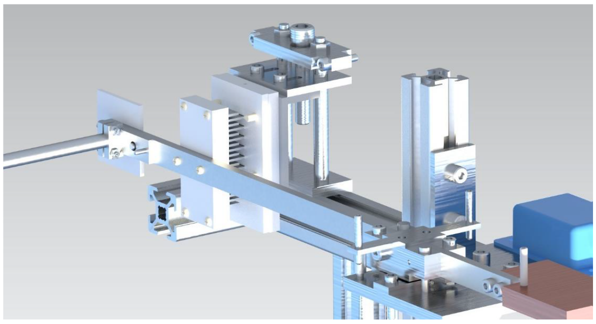

Figure 5.16: MFP calibration with ESC mounted on the pendulum [78].

a symmetric and homogenous plume, see Eq. 5.1 , [200]. This implies that the MFP needs to detect values by one or two orders of magnitude smaller to sufficiently resolve the measured thrust.

$$F_{\text{target}} = F_{\text{total}} \cdot \frac{D^2_{\text{target}}}{D^2_{\text{plume}}} \tag{5.1}$$

The calibration process consists of two main steps. First step is to calibrate the ESC before mounting it on the pendulum and the second step is to calibrate the arm with the ESC mounted as shown in Fig. 5.16-5.17. Calibration set-up for the ESC was prepared and is shown in Fig. 5.18-5.19. The set-up uses a Shimadzu AUW220D precision scale. One part of the comb is mounted on the 3D-printed base attached on the scale, while the other part is mounted on a 3D-printed lid placed on top. Above the lid a 3D-printed structure is mounted with the purpose of allowing the upper part of the comb to move in three directions so that it can be aligned and properly positioned with respect to the lower part of the comb. In this configuration, there is no interference between the scale electronics and the high voltage applied on the ESC. The test was performed connecting the ESC to a high voltage power supply, a Testec TT-SI 9010 voltage probe and an oscilloscope. Different measurement sets conducted and the data recorded are plotted in Fig. 5.20.

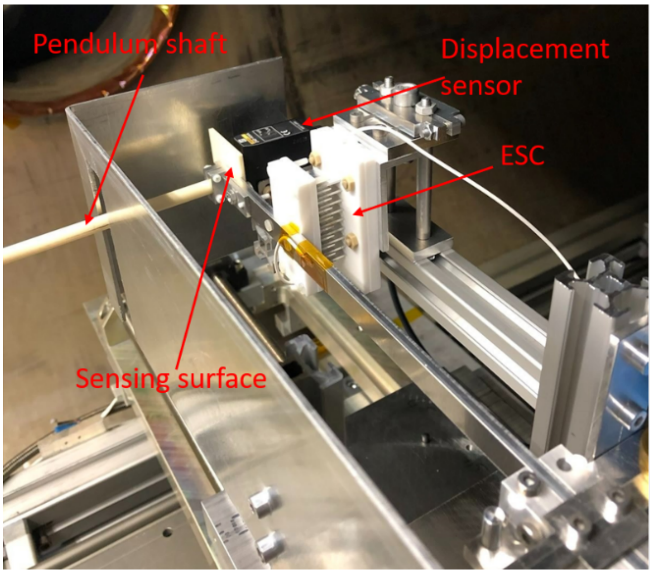

Figure 5.17: MFP calibration set-up with ESC mounted on the pendulum.

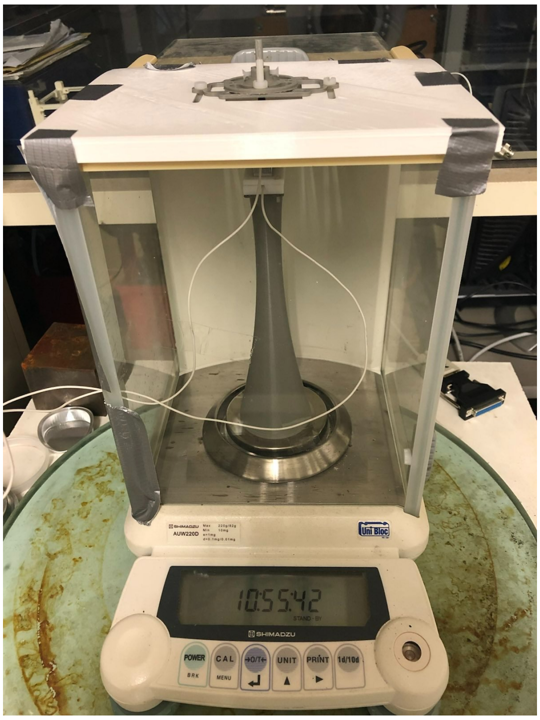

Figure 5.18: ESC calibration set up: front view.

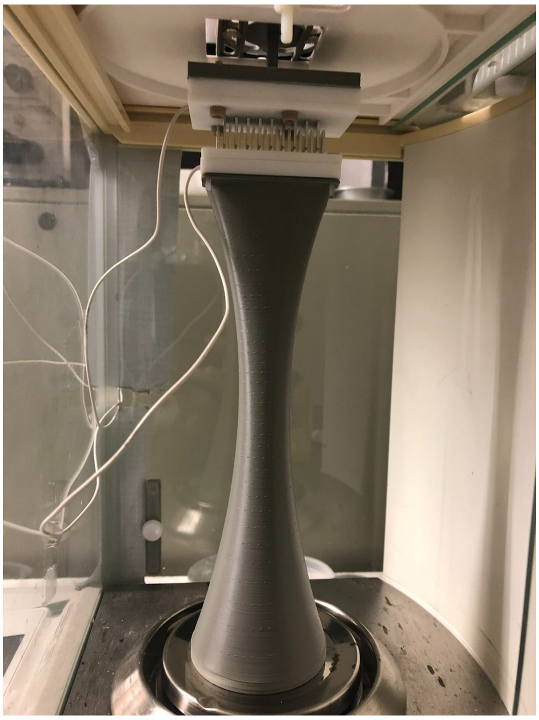

Figure 5.19: ESC calibration set up: side view.

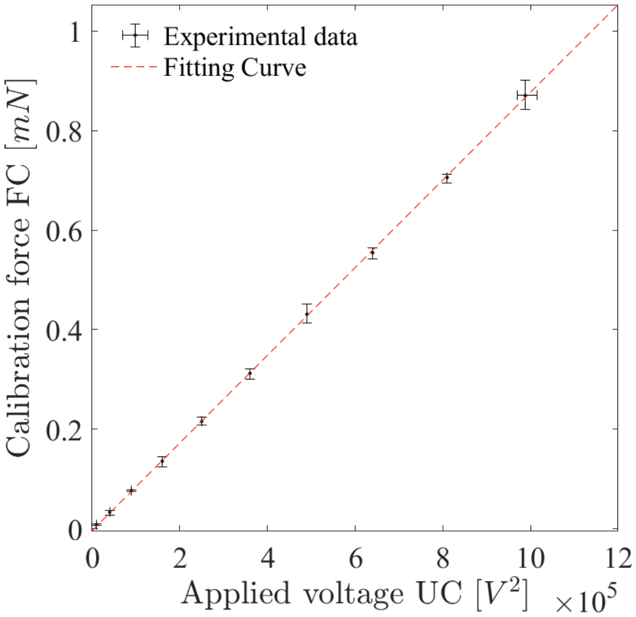

Figure 5.20: ESC calibration results and fitting curve of the measurement data using the precision scale.

The fit line plotted in the data, indicates linearity of the force with respect to V^2. Five different measurement sets were conducted in different moments and with different recording procedures. Some datasets were recorded using five voltage points while others with ten voltage points. For each voltage point the measurement was repeated three times. Another differentiation was that for some datasets the force was calculated by subtracting the measurement from the reference value while for other datasets the scale was tared (zeroed) before the measurement and the net value was recorded. The environment's influence has been minimized as much as possible by ensuring all the openings on the scale were closed, the cables are properly routed so that there was not any resistance on the ESC and the room area was closed and secured to avoid any external disturbances. The results show repeatability among the different datasets, showing a linear trend between force and V^2. The measurements were taken in a voltage range of 0–1000 V, resulting to forces of 0–0.9 mN.

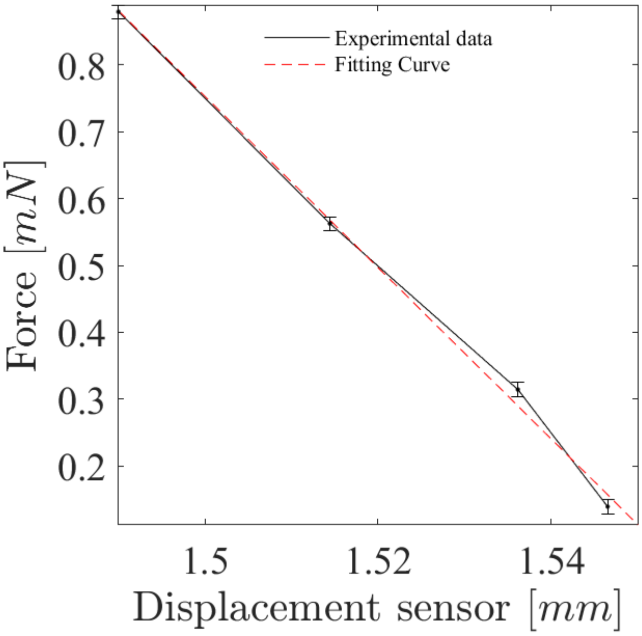

Figure 5.21: Momentum Flux Probe calibration results.

Next step in the calibration process is the mounting of the ESC on the pendulum and the support structure (see Fig. 5.16-5.17). Calibration of the pendulum is performed in vacuum conditions. The relation between voltage and displacement of the arm is extracted. After the stabilization of the pressure inside the chamber, the voltage range is applied on the ESC and the displacement LED sensor data are recorded. By translating the displacement data into force, the results are plotted in Fig. 5.21. A fitting line in the data shows the linear behaviour of the results. This step concludes the construction of the final calibration curve as well as closes the calibration process. Then, the set-up is prepared for performing the momentum flux measurements of the HPT. To assess thermal influence on the probe, thermo elements were positioned at each sensors location and in front of the shield. During operation of the thruster, the temperature stabilized at 25 °C, hence, no significant thermal drift is to be expected. Next, the sensors were mounted on the MFP and the HPT was used to make initial tests to check the functionality of the probe in the presence of the plasma plume. The first test was conducted by placing the graphite target in a distance of 40 cm and the HPT was firstly operated using only cold gas flow (i.e. HPT power off) and then ignited at an input power of 60 W, solenoid current of 6.5 A and mass flow of 0.8-1.2 mg/s. The MFP was experiencing a small movement while putting different cold gas flows which recorded by the displacement sensor. However, it was concluded that the distance from the plume is still large to provide an accurate measurement when the HPT was ignited. The next test attempt was conducted by first moving the target very close to the HPT exit plane, so that the target is able to absorb most of the plume area and by operating the HPT at higher power levels. The power levels were in the range of 150-250 W while the applied solenoid current was adjusted from 10 A down to 4 A. While the post-processing of the data is currently ongoing, some observations were made. The adjustment of the solenoid current to lower levels created a more collimated plasma plume at the expense of higher power reflection but also caused a brightness jump which probably indicates the transition in the *Helicon* mode regime. In the following test activities, measurements at different distances from the plasma plume will be investigated, checking their potential influence in the HPT discharge behaviour. Also, the potential reflection disturbances of the shield on the pendulum will be examined.

5.3.4 Inductive Magnetic B-dot Probe Set-up

Finally, to evaluate the discharge behaviour of the HPT a set-up for an inductive magnetic B-dot probe has been employed [192]. This type of probe is used for the detection of the rotating magnetic field of *Helicon* waves inside the plasma plume. The operational principle of the B-dot probe is based on Faraday's law of induction, given by the Eq. 5.2, where ϵ is the electromotive force and ϕ_B is the magnetic flux.

$$\epsilon = -\frac{d\phi_{\mathrm{B}}}{dt} \tag{5.2}$$

A conductive wire loop is the sensing element of the probe. Three coils are used to get measurements in three directions. The magnetic field induces a voltage on the coils, given in Eq. 5.3, which is used to estimate the amplitude of the B-field. The NA is the calibration factor where N is the number of loops, A is the area enclosed by the loop and ω is the angular frequency.

$$V = -NA\left|\frac{dB_{tot}}{dt}\right| = -NA\omega|B| \tag{5.3}$$

The working frequency of the HPT is at 40.68 MHz and the maximum loops for each coils is chosen equal to N=5. The cross section of the conductive wire is Aw = 0.2mm. The wire loop around the x–axis is A_x = 16mm, around the y–axis is A_y = 25mm, and around the z–axis is A_z = 36mm. The main material of the probe is PEEK and a borosilicate glass tube encloses the probe to minimize contact with the plasma. The design layout is depicted in Fig. 5.22. The sensing signal on the coils passes through the cabling inside the

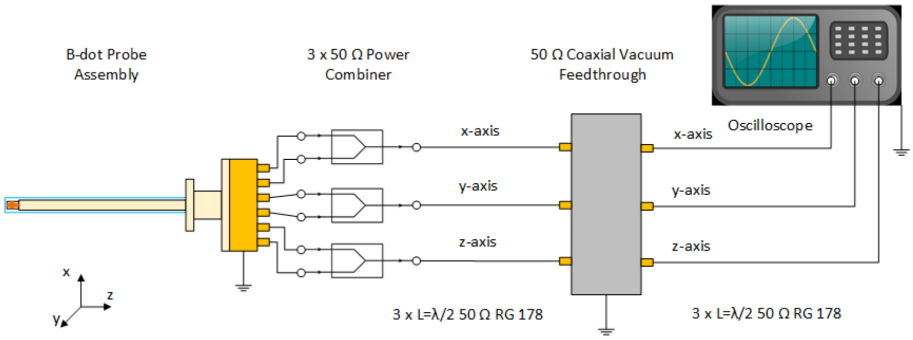

Figure 5.22: Schematics of the B-dot probe [78].

tube, ending up in an RF power combiner for each axis to remove the capacitive pick-up voltage that arises between coils and plasma. An oscilloscope is attached downstream of a vacuum feedthrough to record the measurements.

Two set-ups were developed to calibrate the probe over a broad range of frequencies. For what concerns low frequencies, a Helmholtz coil is used. The set-up prepared for low-frequency calibration of the probe is shown in Fig. 5.23. Each coil is made of N=27 loops with a copper wire of 1 mm in diameter. The coils are mounted on a PA base. The base and the probe are mounted on 3D-printed parts to facilitate the alignment.

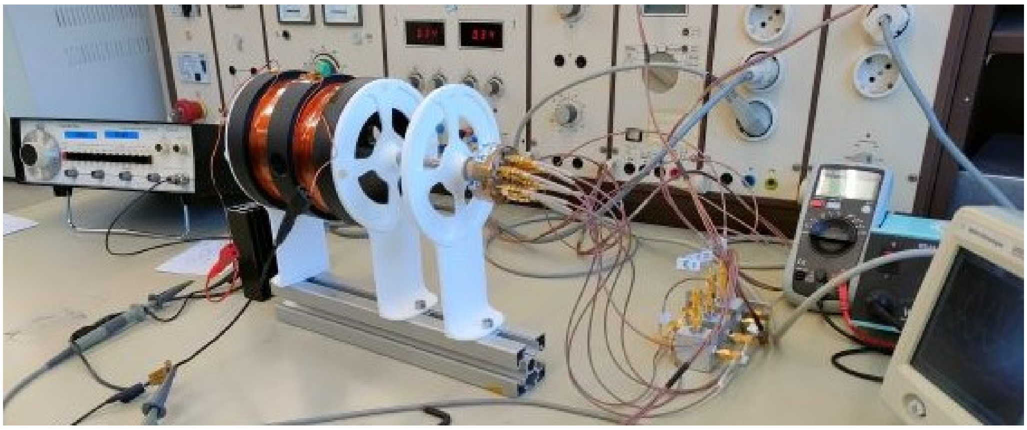

Figure 5.23: B-dot probe low frequency calibration set-up [78].

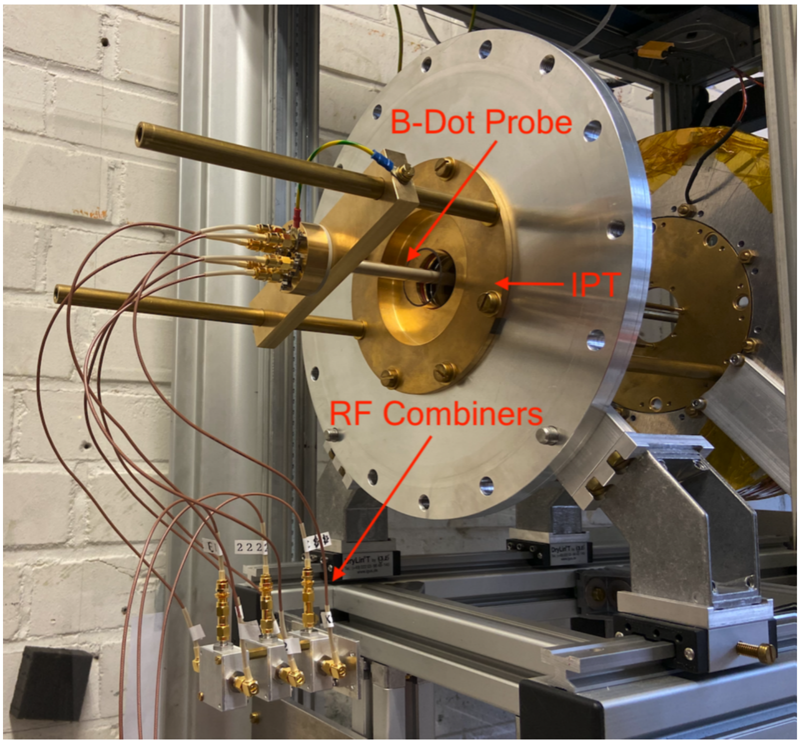

Figure 5.24: B-dot probe high frequency calibration set-up [78].

High frequency calibration uses the HPT itself. The homogeneous and linear polarized magnetic field inside the thruster is used in this case to calibrate the probe. The set-up is shown in Fig. 5.24. A function generator is connected to the probe, providing a set of different voltages at the resonant frequency of the HPT, i.e. 40.68 MHz. The output signal is recorded via an oscilloscope. The rotating magnetic field can be reconstructed with further data post-processing and analysis of the measurements. The calibration of the probe is currently undergone and will be followed by the measurements in the plasma plume.

Part II

Fluid modelling of a HPT

The accurate simulation of the plasma transport in Helicon sources is a key aspect to improve the design of Helicon Plasma Thrusters (HPT) both in terms of propulsive performance and manufacturability of the source. For this reason, the development of numerical codes capable of predicting thrusters performance in an accurate and computationally efficient way, is a subject growing a great deal of interest in the scientific community.

Chapter 6

Plasma fluid model

When it comes to optimizing the design of a HPT, it is fundamental to simulate in an accurate manner the plasma generation and transport within the thruster. In this regard, the development of numerical tools is required to grasp all the physical phenomena governing a HPT [8]. Many numerical methods have been used in literature for modelling the plasma transport; in Sec. 1.2.2, an extensive literature review of these methods has already been presented. Nevertheless, we recall the most important approaches are the fluid [15, 206], kinetic [50, 207, 16], Particle-In-Cell with Monte-Carlo Collisions (PIC-MCC) [51, 208], and hybrid [49, 54, 53]. The starting point of the work presented in this chapter is based on the numerical strategy proposed by the author [209] and Magarotto *et al* [70]. More specifically, a numerical suite consisting of several subroutines that solves self consistently the wave propagation and the plasma transport in a Helicon source [13] is presented with a particular emphasis on the development of a plasma transport code that encompasses the fluid approach [88, 39, 209, 70].

6.1 Numerical strategy

To properly describe a Helicon discharge, the RF antenna, the plasma discharge, and any additional component (e.g., dielectric tube, coils/magnets, shields), either metallic or dielectric are carefully modelled. The model presented in this work is not based on any specific shape of the antenna or discharge chamber since the code solves self-consistently both the wave propagation and the plasma transport in a 3D domain, so as a consequence the antenna and the discharge chamber can have any shape and mutual orientation. To obtain a self consistent prediction of the plasma dynamics within HPT, both the plasma-wave coupling and each species transport within the discharge chamber must be resolved. Specifically, the RF antenna, which is fed with a voltage in the range of tenths of MHz (e.g. 1 - 30 MHz), emits EM waves which propagate within the plasma, and are ultimately absorbed by the latter; such phenomena have time scales in the order of 10^{-6} s. Consequently, the plasma configures itself under the forcing action of the deposited power, with characteristic times of approximately 10^{-3} s [64, Tab.(2.1)]. From a physical standpoint, the independent solution of the plasma-wave coupling, and the transport phenomena is justified since the two physical processes are well separated.

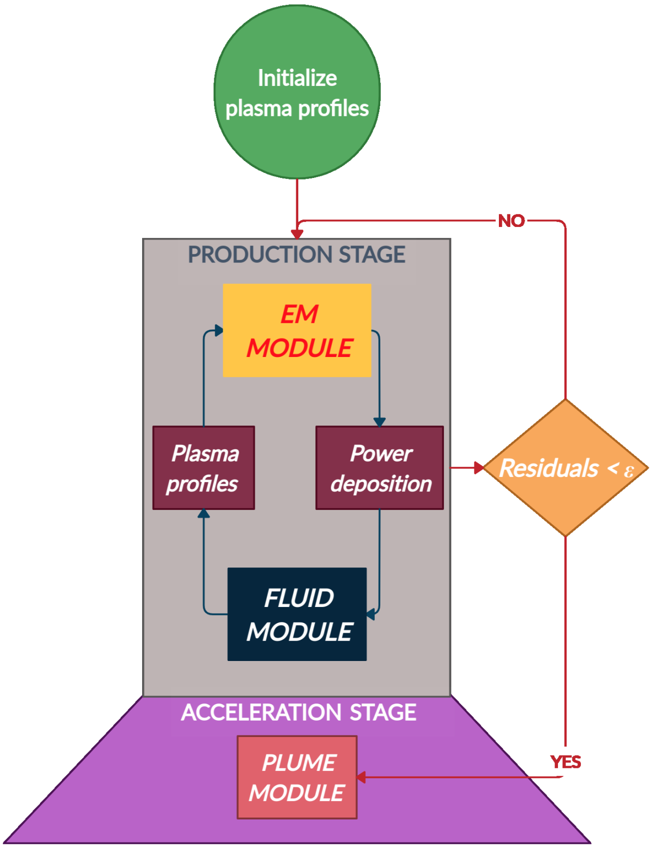

Figure 6.1: HPT simulation strategy.

In Fig. 6.1, the proposed numerical strategy for handling a HPT is shown. In the production stage, the main subroutines of the tool consist of two mutually coupled modules: the first one, namely the EM module, solves the EM wave propagation and thus the power coupled into the plasma by the antenna; the second is the FLUID module which handles the plasma transport. The former relies on the ADAMANT code [57] to solve for the EM fields that propagate inside the discharge, and the power deposition therein for a given distribution of the density, and temperature of the plasma species. The latter takes as input the deposited power profile from the EM module and handles the plasma transport giving as output the local profiles of each species density and plasma temperature. More specifically, it comprises for each species a set of governing equations based on the fluid approach [88] and implemented according to the finite-volume methodology [210]. After being initialized with uniform values of the plasma parameters, the two modules have been coupled by means of an iterative procedure until convergence of the plasma parameters to find out the equilibrium conditions. From the numerical standpoint, the EM (FLUID) module relies on an unstructured (structured) mesh; therefore, the power deposition that is computed by the EM module is interpolated on the structured mesh of the FLUID module, while the plasma parameters that are evaluated by the FLUID module are interpolated on the unstructured mesh of the EM module. To verify that a converged solution has been found, the code checks that the residual of the electron density of two consecutive iterations is lower than a prescribed threshold ($\epsilon_{\max}$)

$$\max_j \left(\frac{n_{e,j}^{i+1} - n_{e,j}^{i}}{n_{e,j}^{i}} \right) \leq \epsilon_{\max} \quad , \quad j = 1, \dots, N_F \tag{6.1}$$

in which j, and N_F are the node index, and the number of nodes, respectively, in the structured mesh, whereas i indicates the iteration step. Finally, once the solution of the production stage is obtained, two possibilities can be executed, namely

- directly integrating the plasma profiles in the plume region to obtain an estimation of the propulsive performance such as Thrust and Specific Impulse
- input the plasma profiles to the PLUME module which is responsible to compute the propulsive performance through dedicated models

Regarding the latter, both the simplified propulsion model presented in Sec 2.2 and the PIC model presented in Sec. 4.2, can be used. The former is needed for fast but rough estimations of the propulsive performance, whereas the latter (more computationally expensive) can be used to have an accurate estimation of both the propulsion data and information related to plume-satellite interactions; regarding the latter, more details are provided in [211, 87].

Considering more into details the EM module, the EM fields traveling through the plasma have been computed in the frequency domain by means of the ADAMANT code [57], which provides a local solution of the polarization currents ($\mathbf{J}_\mathrm{p}$) and the electric flux density ($\mathbf{D}_\mathrm{p}$) into the plasma. Knowing local values of the fields and currents, the local coupled RF-power into the plasma ($\mathcal{E}_{pow}$) can be calculated integrating the electric work [57, Eq.(12)]. It is worth to recall that in ADAMANT the plasma discharge is treated as an anisotropic medium described through a relative dielectric permittivity tensor by means of the Stix theory [212], which provides a reasonable description of the electric behavior of a magnetized plasma, and therefore of the deposited power, provided that non-linearities and non-local effects of wave-particle interaction can be neglected [56]. Hence, waves dumping is assumed to be caused only by collisional effects [39, Chap. 4], neglecting other mechanisms of power deposition such as i) Landau dumping [213], and ii) parametric decay instabilities [214], since the former has been proved to play a minor role in a typical Helicon discharge [213], while the latter is the responsible of the anisotropy on ion temperature measured in the range of the lower hybrid frequency [214]. The computed power delivered to the plasma is then used as an input for the FLUID module.

For what concerns the FLUID module, the discharge is considered to be filled with a non-homogeneous weakly-ionized argon plasma, that is modelled as multi-fluid mixture of electrons, and heavy species (i.e., ions, excited and neutral particles). Each species is assumed to present a Maxwellian distribution function so that the transport problem could be solved with the fluid approach [88]. Early experiments on Helicon sources [34] showed high energy tails of electrons distribution function. Nonetheless in [213], Chen stated that deviations from the Maxwellian distribution are not such to have strong influence on the dynamics of the discharge. Conversely, assuming the Maxwellian distribution assumption for the ions is not generally correct. As a matter of fact, the experiments shown in Scime *et al.*, [215] highlighted: i) a significant anisotropy between the ion temperature parallel and across the magnetic field lines, with the former being up to an order of magnitude greater than the latter, and ii) perpendicular ion temperature reaching up to 1 eV. Nevertheless, these effects are shown to be significant in correspondence of the lower hybrid frequency [214], thus assuming a Maxwellian distribution also for the ions is expected to have a negligible effect on numerical simulations except for the lower hybrid frequency range. In addition, this assumption is enforced by the good agreement between the experimental measurements and the numerical results obtained with a simplified fluid model that neglect the anisotropy of ions temperature and reported in [216]. Finally, the development of the numerical strategy has been performed considering the chemistry model shown in Chapter 3 which is suitable for low pressure (< 50 mTorr) discharges fed with noble gases such as argon, neon, krypton and xenon. This is reasonable as most of the electric propulsion applications are fed with xenon or krypton [7]. Nevertheless, argon has been specifically chosen for the development of the model due to the abundance of experimental data of Helicon discharges in the literature [10], which is crucial for an accurate validation of the codes in terms of the physical assumptions considered.

6.2 Fluid model

The plasma is treated as a mixture of different species, therefore a multi-fluid approach is considered. Specifically, a set of transport equations for each species is considered. The main assumptions employed are

- Maxwellian distribution function for each species
- non-magnetized ions
- electrons transport can be described according to the Drift-Diffusion approximation

The rationale behind the first assumption has been already discussed in Sec. 6.1, and is at the basis of the fluid description of the plasma species. However, it is worth recalling that the Maxwellian distribution assumption is employed also for the calculation of the transport coefficients and notably also of the terms related to the plasma chemistry as discussed in Chapter 3. For what concerns ions, given the typical dimensions, magnetic field, and neutral pressure values in HPT sources [217, 218] the non-magnetization hypothesis is justified by the fact that the ions Larmor radius is proportional to the characteristic scale-length of the discharge. Lastly, the Drift-Diffusion (DD) approximation for electrons was adopted instead of the full momentum equation [219], since the magnitude of the electrons' collision frequency is higher than its estimated velocity gradient [220]. However, this approximation might not be strictly respected by heavy species at low pressure [220], therefore their general momentum equations must be considered.

6.2.1 Transport equations

The general set of governing equations consists in the balance of mass, momentum and energy for each species present in the plasma. For what concerns electrons, the equations read,

$$\frac{\partial n_e}{\partial t} + \nabla \cdot \overline{\Gamma}_e = R_e \tag{6.2a}$$

$$\frac{\partial}{\partial t}\left(\frac{3}{2} q n_e T_e\right) + \nabla \cdot \left(\frac{5}{2} q T_e \mathbf{\Gamma}_e + \overline{\overline{k}}_e \nabla T_e\right) + q\, \boldsymbol{E} \cdot \mathbf{\Gamma}_e = R_\varepsilon + P_\varepsilon \tag{6.2b}$$

$$\varepsilon_0 \nabla^2 \phi = -q(n_i - n_e) \tag{6.2c}$$

where n_e is the electron density, T_e is the electron temperature (in eV). Eq. 6.2c, is the *Poisson* equation, where ϕ is the electrostatic potential, q is the elementary charge, ε_0 is the vacuum permittivity, n_i the ion density, and $\boldsymbol{E} = -\nabla\phi$. Regarding the latter, it is worth recalling that $\boldsymbol{E}$ is not related to the electrostatic component of the EM waves excited by the RF antenna, but rather to the electrostatic field arising from the charge unbalance due to the plasma diffusion and not to the oscillating electric field due to the RF power coupling [221]. According to the DD approximation of the momentum equation [221, 222], the particles fluxes read

$$\overline{\Gamma}_e = \overline{\overline{\mu}}_e n_e \mathbf{E} - \overline{\overline{D}}_e n_e \frac{\nabla p_e}{p_e} \tag{6.3}$$

where p_e is the electron pressure, $\overline{\overline{\mu}}_e$ and $\overline{\overline{D}}_e$ are the transport coefficients, namely the mobility and the diffusivity respectively. The expression of the transport coefficients for magnetized species takes the tensor form,

$$\overline{\overline{\mu_e}} = \mu_e \overline{\overline{\overline{T}}}_r, \quad \overline{\overline{\overline{D_e}}} = D_e \overline{\overline{\overline{T}}}_r \tag{6.4}$$

where, $\mu_e = q/m_e \nu_c$ is the isotropic mobility, m_e is the electron mass, and ν_c is the collision frequency [223]. The isotropic diffusivity is given by the *Einstein* relation which reads $D_e = \mu_e T_e$ (with T_k in eV) [39, 88, 47]. $\overline{\overline{\overline{T}}}_r$ is the transport tensor, which is defined as

$$\overline{\overline{\overline{T}}}_r = \frac{1}{1 + |\chi_c|^2} \begin{pmatrix} 1 + \chi_x^2 & \chi_x \chi_y - \chi_z & \chi_x \chi_z + \chi_y \\ \chi_x \chi_y + \chi_z & 1 + \chi_y^2 & \chi_y \chi_z - \chi_x \\ \chi_x \chi_z - \chi_y & \chi_y \chi_z + \chi_x & 1 + \chi_z^2 \end{pmatrix} \tag{6.5}$$

where $\boldsymbol{\chi}_c = (\boldsymbol{\chi}_x, \boldsymbol{\chi}_y, \boldsymbol{\chi}_z)$ is the Hall parameter vector expressed as function of the intensity of the magnetic field along the axes (x, y, z) respectively [224]. The sink/source terms (R_e and R_ε) come from the plasma chemistry model. P_ε is the RF power deposited by the antenna calculated by the EM module (i.e., through ADAMANT [71]), it reads

$$\varepsilon_{\text{power}} = \frac{1}{2} Re\{\boldsymbol{J}_P^* \cdot \boldsymbol{E}_P\} \tag{6.6}$$

where $\boldsymbol{J}_P$ and $\boldsymbol{E}_P$ are the polarization current and the local value of electric field inside the plasma respectively. Finally, it is worth noting that the electron energy equation (Eq. 6.2b) does not rely on the quasi-isotherm hypothesis enforced in previous works [70, 13, 14].

Specifically, the electron heat flux is considered through the *Fourier* law (see Eq. 4.2) and the thermal diffusivity reads $\overline{\overline{k_e}} = 5/2n_e\overline{\overline{D_e}}$ [221, 88, 53]. Nevertheless, a deeper analysis of the effects of the hypothesis of quasi-isotherm electron energy is discussed in Chapter 7.

Regarding the ions, the transport equations read,

$$\frac{\partial n_i}{\partial t} + \nabla \cdot n_i \mathbf{u_i} = R_i \tag{6.7a}$$

$$\frac{\partial}{\partial t}\left(n_i \mathbf{u_i}\right) + \nabla \cdot \left(n_i \mathbf{u_i}\right) = -\nabla p_i + q n_i \boldsymbol{E} - m_i n_i \nu_i \mathbf{u_i} \tag{6.7b}$$

$$\frac{\partial}{\partial t}\left(\frac{3}{2}p_i\right) + \nabla \cdot \left(\frac{5}{2}p_i \mathbf{u_i} + k_i \nabla T_i\right) - \mathbf{u_i} \cdot \nabla p_i = R_{\varepsilon_i} \tag{6.7c}$$

and the neutrals and exciteds species read,

$$\frac{\partial n_0}{\partial t} + \nabla \cdot n_0 \mathbf{u_0} = R_0 \tag{6.8a}$$

$$\frac{\partial}{\partial t}\left(n_0 \mathbf{u_0}\right) + \nabla \cdot \left(n_0 \mathbf{u_0}\right) = -\nabla p_0 - m_0 n_0 \nu_0 \mathbf{u_0} \tag{6.8b}$$

$$\frac{\partial}{\partial t}\left(\frac{3}{2}p_i\right) + \nabla \cdot \left(\frac{5}{2}p_0 \mathbf{u_0} + k_0 \nabla T_0\right) - \mathbf{u_0} \cdot \nabla p_0 = R_{\varepsilon_0} \tag{6.8c}$$

where n_*, T_* are respectively the ion, neutrals and excited densities and temperatures (expressed in K), R_* and R_{ε_*} the species particles and energy sink/source terms obtained from the chemistry model (see Sec. 6.2.2); m_*, ν_*, k_* are the particles mass, the momentum exchange collision frequency and the thermal diffusivity. The latter reads $k_* = -\frac{5}{2}\frac{n_* k_B^2 T_*}{m_* \nu_*}$ [221, 88, 53], where k_B is the *Boltzmann* constant. Finally, it is worth noting that the conservative formulation of the fluid equations is enforced [210].

Under certain conditions it is possible to assume the DD formulation also for the heavy species. This is true when the momentum collisional terms in the momentum equations (see Eqts. 6.7b-6.8b) are proportional or greater than the convective terms [39], which happens when dealing with discharges at a moderate pressure where a diffusive regime is dominant. In addition, several authors have employed simplified models such as the polytropic [45] or the isotherm [70, 39] hypothesis for the heavy species instead of solving the full energy equation. Under this assumptions, the Eqts 6.7-6.8 can be written as

$$\frac{\partial n_k}{\partial t} + \nabla \cdot \mathbf{\Gamma}_k = R_k \tag{6.9a}$$

$$\mathbf{\Gamma}_k = \pm \mu_k n_k \boldsymbol{E} - D_k \nabla n_k \tag{6.9b}$$

where n_k, is the density of the k-th species and μ_k, D_k are the transport coefficients, namely the mobility (which is null for neutral particles) and the diffusivity respectively. The latter can be expressed as [225]

$$D_k = \frac{3}{8}\frac{\sqrt{\pi k_B T_0/M}}{\pi \sigma_D^2 \Omega_D}\frac{1}{n_0 + n_s + n_i} \quad , \quad k = 0, s, i \tag{6.10}$$

in which σ_D, and Ω_D depend on Lennard-Jones parameters that can be inferred from [226], while for what concerns ion mobility follows from the Einstein's relation $\mu_i = D_i/T_i$. Nevertheless, more details on the diffusion model are provided in Sec. 2.1. In Chapter 7, a deeper analysis of the DD assumption against the full momentum solution, is shown and the validity of the hypothesis is discussed. Nonetheless, the validity of the isotherm formulation against the solution of the full energy equation is discussed in Sec. 7.2 in the frame of the model validation.

Reactions	
$Ar_{\mathrm{GS}} + e \rightleftharpoons Ar_{\mathrm{1sM}} + e$	excitation
$Ar_{\mathrm{GS}} + e \rightleftharpoons Ar_{\mathrm{1sR}} + e$	excitation
$Ar_{\mathrm{GS}} + e \rightleftharpoons Ar_{\mathrm{2p}} + e$	excitation
$Ar_{\mathrm{1sM}} + e \rightleftharpoons Ar_{\mathrm{1sR}} + e$	excitation
$Ar_{\mathrm{1sM}} + e \rightleftharpoons Ar_{\mathrm{2p}} + e$	excitation
$Ar_{\mathrm{1sR}} + e \rightleftharpoons Ar_{\mathrm{2p}} + e$	excitation
$Ar_{\mathrm{GS}} + e \rightleftharpoons Ar_{\mathrm{GS}} + e$	elastic scattering
$Ar_{\mathrm{1sM}} + e \rightleftharpoons Ar_{\mathrm{1sM}} + e$	elastic scattering
$Ar_{\mathrm{1sR}} + e \rightleftharpoons Ar_{\mathrm{1sR}} + e$	elastic scattering
$Ar_{\mathrm{2p}} + e \rightleftharpoons Ar_{\mathrm{2p}} + e$	elastic scattering
$Ar_{\mathrm{GS}} + e \rightarrow Ar_{+} + 2e$	ionization
$Ar_{\mathrm{1sM}} + e \rightarrow Ar_{+} + 2e$	ionization
$Ar_{\mathrm{1sR}} + e \rightarrow Ar_{+} + 2e$	ionization
$Ar_{\mathrm{2p}} + e \rightarrow Ar_{+} + 2e$	ionization
$Ar_{\mathrm{1sR}} \rightarrow Ar_{\mathrm{GS}} + h\nu$	radiative decay
$Ar_{\mathrm{2p}} \rightarrow Ar_{\mathrm{1sM}} + h\nu$	radiative decay
$Ar_{\mathrm{2p}} \rightarrow Ar_{\mathrm{1sR}} + h\nu$	radiative decay

Table 6.1: Reactions considered in the CRM.

6.2.2 Plasma chemistry

In Chapter 3, a collisional-radiative model (CRM) has already been presented with the aim of reproducing the dynamics of an argon plasma when the excited levels are considered. Specifically, the 1s and 2p excited levels along with the ground state and the first ionized level have been considered. Taking into account only 1s and 2p excited species is justified since the working pressure of typical HPTs is sufficiently low (i.e., tenths of mTorr or lower) that the density of higher excitation levels is negligible according to experiments [227]. The excited species (reported in Chapter 3) have been lumped into three equivalent states, namely 1s metastable ($1s_{\mathrm{M}}$), 1s resonant ($1s_{\mathrm{R}}$), and 2p in order to reduce the number of fluid equations [223]. The reactions considered are summarized in Tab. 6.1. The procedure to calculate the reaction rates, the diffusion coefficients, along with the source/sink terms in Eq. 4.1 and Eq. 4.2 in case of a Maxwellian electron distribution function has been thoroughly discussed in Chapter 3.

6.2.3 Anomalous diffusion

The anomalous transport is an empirically observed discrepancy between the values of the diffusion coefficients computed classically (see Sec. 6.2.1) and the ones measured in experiments. This phenomenon can be attributed to the establishment of turbulence which is broken down by instabilities of the magnetic field [228]. The classical definition of the electron diffusion coefficient across a magnetic field reads [229]

$$D_{\perp} = \frac{qT_e\nu_c}{m_e{\omega_B}^2} \sim \frac{1}{B^2} \tag{6.11}$$

where ω_B is the cyclotron frequency [229]. Bohm found that the upper limit of the diffusion coefficient behaves rather like [105],

$$D_{Bohm} = \frac{1}{16}\frac{T_e}{B} \sim \frac{1}{B} \tag{6.12}$$

In order to account for this phenomenon, Boeuf [230] suggested to modify the collisional frequency in the momentum equation adding a term proportional to the cyclotron frequency

$$\nu_{\mathrm{Bohm}} = \nu + \alpha\omega_C \tag{6.13}$$

where α is an empirical coefficient that should be adjusted to match experiments. Assuming an axially oriented magnetic field $\boldsymbol{B_0} = (0, 0, B_z)$, this methodology leads to the following formulation of the transport matrix:

$$\overline{\overline{T_r}} = \frac{1}{{\chi_z}^2 + (1+\alpha\chi_z)^2}\begin{pmatrix} 1+\alpha\chi_z & -\chi_z & 0 \\ \chi_z & 1+\alpha\chi_z & 0 \\ 0 & 0 & {\chi_z}^2 + (1+\alpha\chi_z)^2 \end{pmatrix} \tag{6.14}$$

In case of a generically oriented magnetic field, the transport matrix is obtained via the tensor rotation approach suggested in Sanchez-Villar [53].

6.2.4 Boundary conditions

In proximity of the walls, the charged particles fluxes are such that an electrically unbalanced sheath forms [88, 39]. To model this phenomena, the Bohm sheath criterion [97] is the one most commonly employed for a wide variety of discharges and wall materials. When solving the fluid equations presented in Sec. 6.2.1, the boundaries of the fluid problem are limited at the pre-sheath, i.e., the sheath region is not directly solved, but rather assumed imposing the fluxes at the sheath-edge. In addition, the current-free condition [70] is enforced when prescribing the charged fluxes at the walls. In each boundary of the domain, a Robin condition is assumed for the electron (and ions if DD is employed) continuity equation to enforce the Bohm criterion [221],

$$\pm(\mu_k \mathbf{E}) \cdot \hat{\mathbf{k}}\, n_k - (D_k \nabla n_k) \cdot \hat{\mathbf{k}} = \Gamma_\perp \tag{6.15}$$

in which $\Gamma_\perp = \Gamma_e = \Gamma_i = \sqrt{qT_e/M} n_i$ for ion, and electron fluxes, and $\hat{\mathbf{k}}$ is the boundary normal versor. Similarly, for the energy equation (Eq. 6.2b), Bhom sheath criterion [231] has been imposed through a Robin boundary condition that reads

$$-(\mu_\varepsilon \mathbf{E}) \cdot \hat{\mathbf{k}}\, \varepsilon_n - (D_\varepsilon \nabla \varepsilon_n) \cdot \hat{\mathbf{k}} = \Gamma_{\varepsilon,\perp} \tag{6.16}$$

in which $\Gamma_{\varepsilon,\perp} = \left[\frac{T_e}{2}\left(1 + \ln \frac{M}{2\pi m}\right) + 2T_e\right] \Gamma_e$, $\mu_\varepsilon = 5/3\mu_e$, and $D_\varepsilon = \mu_\varepsilon T_e$ according to the *Einstein* relation [39]. For what concerns the thruster's outlet, a constant flux condition is imposed through a Neumann condition to the charged species.

At the walls of the source, excited species diffuse according to the thermal motion while the neutral flux is determined by the recombination of ionized and excited species [221]. A Neumann boundary condition has been imposed, that reads

$$\frac{\partial n_k}{\partial x_\perp} = -\frac{\Gamma_\perp}{D_k} \tag{6.17}$$

in which $\frac{\partial}{\partial x_\perp}$ is the derivative along the $\hat{\mathbf{k}}$ boundary normal versor. For the excited species, the boundary condition depends on the particles thermal flux [232], and $\Gamma_\perp = \Gamma_s = \frac{1}{2} v_{th,0} n_s$ in which $v_{th,0} = \sqrt{8k_B T_0/(\pi M)}$ is the average thermal speed of the heavy particles. As for the neutral species boundary condition, all the ions and the excited particles which collide against the wall have been assumed to recombine [221] in accordance with the ions wall reaction $Ar^+ \longrightarrow Ar$, and the exciteds wall reaction $Ar^* \longrightarrow Ar$; so that $\Gamma_\perp = \Gamma_0 = -(\Gamma_i + \Gamma_s)$. For what concerns the momentum, a Neumann condition is employed, namely

$$\frac{\partial \mathbf{u}_k}{\partial x_\perp} = 0 \tag{6.18}$$

At the thruster inlet/outlet the motion of the excited and neutral species is solely due to convection [13].

As per the *Poisson* equation the potential has been considered grounded assuming the boundaries of the computational domain at the sheath edge, therefore

$$\phi = 0 \tag{6.19}$$

which is implemented through a *Dirichlet* condition. Nonetheless, also the thruster outlet is assumed at ground according to Ahedo et al [15].

6.3 Implementation

The plasma transport equations have been implemented by means of the *Finite Volume Method* (FVM) in a *C++* code employing the *OpenFOAM* [72] libraries. The Poisson equation as long with the balance equations for ions, electrons, exciteds and neutrals,

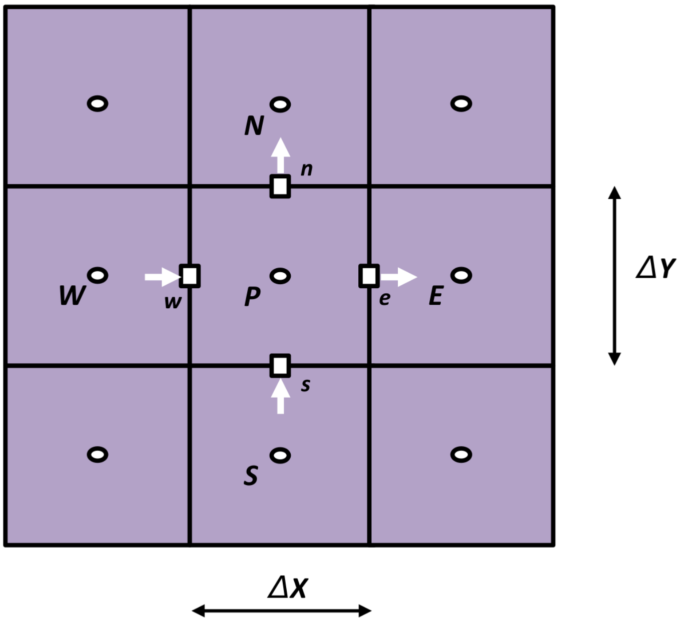

Figure 6.2: Staggered mesh grid for the fluid domain.

have been time integrated in this very order, and spatially discretised on a 3D structured staggered mesh made of hexahedra elements [210]. The peculiarity of the staggered mesh (see Fig. 6.2) consists in performing the computation of the parameters of interest (e.g., density, velocity and temperature) over the cell centers of the mesh, whereas the fluxes transporting those parameters are computed on the face centers. For a deeper review of the staggered mesh and the FVM, the reader is referred to Patankar and Spalding [233, 210].

In order to avoid limiting time step requirements while allowing for stable and accurate solutions when integrating the equations, a number of techniques have been adopted. First, the *Poisson* equation has been implemented employing a semi-implicit scheme in time [234]. Specifically, given the potential ϕ at the time instant $t+1$ the equation has been solved according to,

$$\varepsilon_0 \nabla^2 \phi^{t+1} = -q(n_i^{t+1} - n_e^{t+1}) = -q\left(n_i^t + \Delta t \frac{\partial n_i^t}{\partial t} - n_e^t - \Delta t \frac{\partial n_e^t}{\partial t} \right) \tag{6.20}$$

where Δt is the time step; the electron (n_e^{t+1}), and ion (n_i^{t+1}) densities at the $(t+1)$-th time step are linearized substituting $n_k^{t+1} = n_k^t + \Delta t \frac{\partial n_k^t}{\partial t}$ (with $k = i, e$), in which $\frac{\partial n_k^t}{\partial t}$ is computed at the t-th time step. With this approach, the *Poisson* equation is not influenced by the dielectric relaxation constraint, which can severely limit the time step [234, 222]. Second, the balance equations for each species have been solved by means of an implicit backward marching time integration as shown in Moukalled et al [210]. Thanks to this formulation the *Courant-Friedrichs-Lewy* (CFL) criterion [234, 222] can be avoided. Finally, even though the backward marching time integration is considered, the CFL criterion is still respected, i.e., the *Courant* number is always kept below unity, in order to guarantee the stability and more importantly the accuracy of the solution. For what concerns the spatial discretization, laplacian, divergence and gradient operators have been discretized by means of the *Gauss-Green* theorem and the MUSCL scheme as presented in Moukalled et al [210]. Regarding the boundary conditions, the classical schemes for Dirichlet, Neumann, and Robin conditions [210] are employed. Finally, the solution convergence is obtained once the electron density residuals, i.e., the relative difference between the electron density at two consecutive time steps, is lower than a prescribed threshold ($\epsilon_{F,max}$).

Chapter 7

Numerical results

The scope of this chapter is to quantify the influence that different formulations of the plasma chemistry, the energy equation, and the diffusion model have on the numerical results. Moreover, the validity of the DD hypothesis against the solution of the full momentum equation for the heavy species is discussed as well. To this end, a simplified geometry representative of a medium-low power HPT [8] has been adopted (see Fig. 7.1a) and simulations performed against the results of the previous formulation (herein after referred as OLD) reported in Magarotto et al [70]. The Helicon source has a cylindrical shape of length $L = 0.10$ m and radius $R = 0.05$ m. The magnetic field is generated by Helmholtz coils, as in the prototype proposed by Ziemba [235]. Inside the source, the magnetic field is quasi-axial and the intensity at the thruster outlet is $B_0 = 500$ G [26].

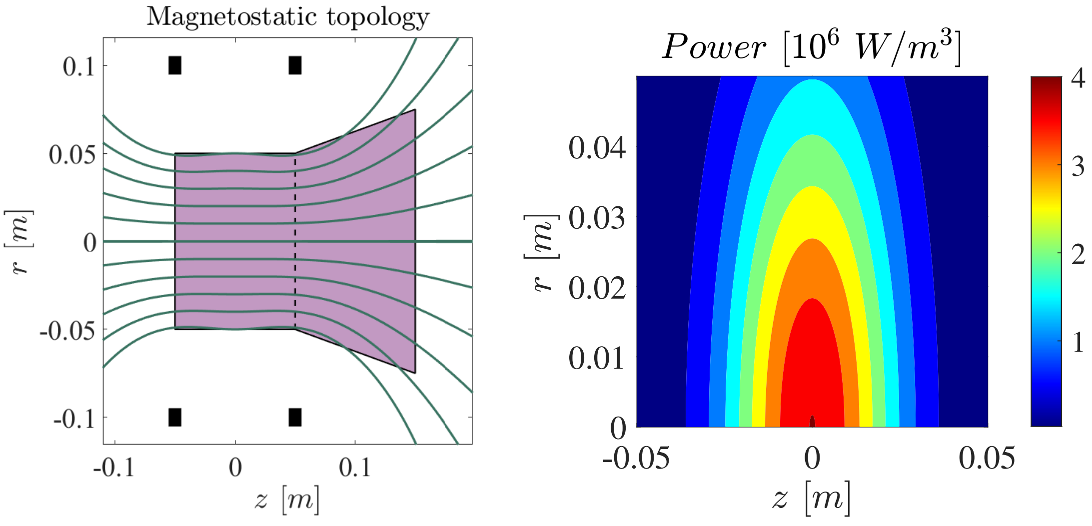

(a) (b)

Figure 7.1: a) Schematic of the simplified HPT considered for the numerical analysis, magnetic field lines and Helmholtz coils have been highlighted. b) Assumed power deposition profile.

The parameters analyzed in the following are the electron density (n_e) and temperature

(T_e) profiles computed with the FLUID module, and thrust (T) and specific impulse (I_{sp}) provided by the analytical plume model of Sec. 2.2. For this analysis, the power deposition profile has been assumed and not computed with the EM module (see Fig. 7.1b) in order to: (i) focus on the effect that each phenomenon (i.e., plasma chemistry, energy equation, and anomalous diffusion) has on the fluid model neglecting the indirect influence of the power deposition profile, (ii) understanding whether these phenomena have a major role on the determination of the propulsive performance. The total power coupled to the plasma is $Pw = 12$ W. The system is fed with argon gas at initial temperature $T_0 = 300$ K. The propellant mass-flow rate ($\dot{m}_0$) has been varied in the range from 0.5 mg/s to 50 mg/s so that the operational neutral density (n_0) is in the range from 10^{19} m^{-3} to 10^{21} m^{-3}. Referring to Fig. 7.1a, the surface at $z = -0.05$ m is considered the thruster inlet while the surface at $z = 0.05$ m is the outlet (boundary conditions are defined coherently). The initial gas convection speed is assumed aligned along the axis of the thruster and its magnitude is $u_0 = 1/4 v_{th}$, where v_{th} is the thermal speed of neutral species. Reaction rates which govern the plasma chemistry are assumed according to Sec. 6.2.2. The discretization of the computational domain consisted of a structured mesh of 31250 hexahedra. The mesh is a 2D axysimmetric one due to the symmetry of the problem and the simplified power deposition used for the physical analysis. The temporal discretization is done with an integration time step of 10^{-8} s. In Tab. 7.1 the parameters used in the simulations of the simplified HPT are shown.

Parameters of the simulations	
R	0.05 m
L	0.10 m
B_0	500 G
Pw	12 W
T_0	300 K
$\dot{m}_0$	0.5 ÷ 50 mg/s
n_0	$10^{19} \div 10^{21}$ m^{-3}

Table 7.1: Parameters used in the simulations of the simplified HPT.

7.1 Plasma chemistry

The results obtained with the plasma chemistry model proposed in Magarotto [70] (i.e., excited condensed in only one equivalent species) have been compared against the ones attained with the formulation discussed in Section 6.2.2. Two versions of the upgraded chemical model have been considered, namely neglecting or considering radiative decay reactions (see Tab. 6.1). Hereinafter, the chemistry model proposed in Magarotto [70] has been referred to as OLD, the new model in which the radiative decay is neglected as CM (collisional model) and the last one as CRM (collisional-radiative model). The assumed mass flow rate is $\dot{m}_0 = 5$ mg/s, namely the operational neutral density is $n_0 \approx 10^{20}$ m^{-3}, the quasi-isotherm formulation of the energy equation is adopted [70], and the anomalous transport has been neglected.

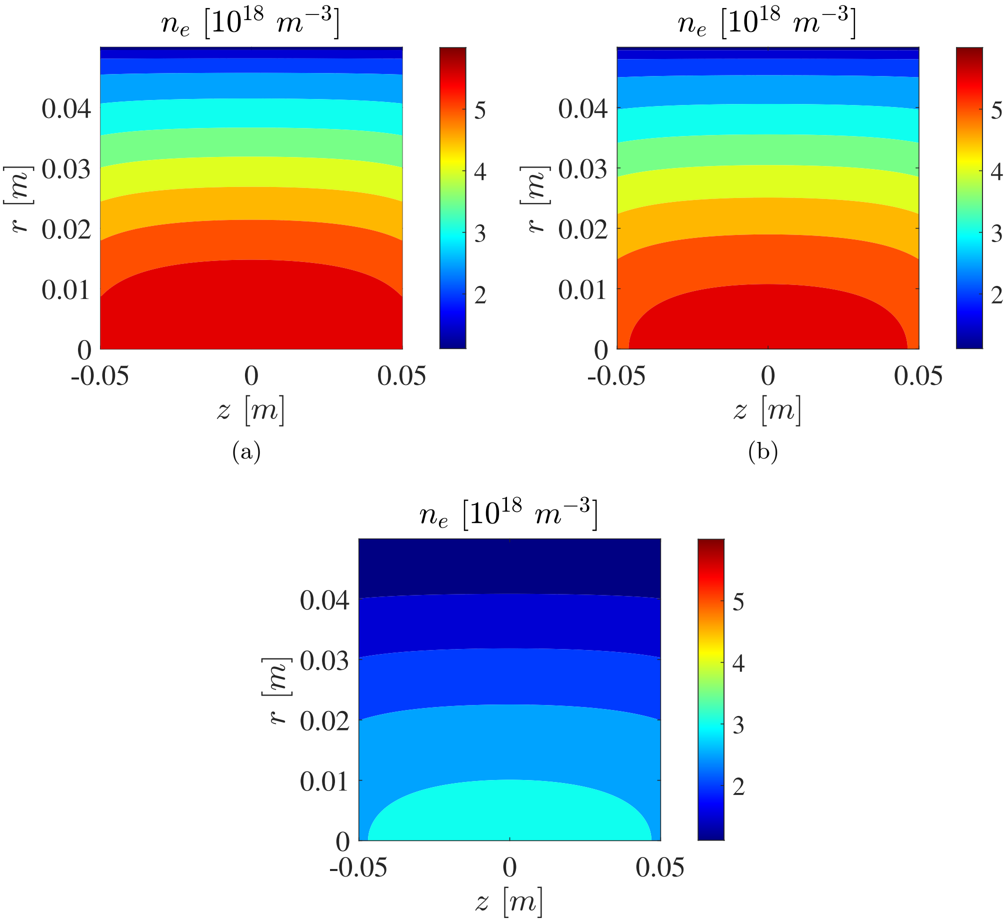

(a) (b) (c)

Figure 7.2: Electron density (n_e) within the Helicon source as a function of the radial (r) and axial (z) coordinates. a) OLD, b) CM, and c) CRM chemical models.

Plasma density and electron temperature profiles obtained with the three formulations of the plasma chemistry are depicted in Fig. 7.2 and Fig. 7.3 respectively. There are no significant differences (lower than 5%) between OLD and CM both in terms of electron density and temperature. On the other hand, the electron density computed with CRM is almost 60% lower with respect to CM and OLD; the temperature peak is 25% higher. This is due to the loss mechanisms associated to the decay of the excited states toward lower energy levels (see Chapter 3). In Table 7.2, the propulsive performance is reported; a significant drop of about 40 % can be seen comparing CRM and CM / OLD.

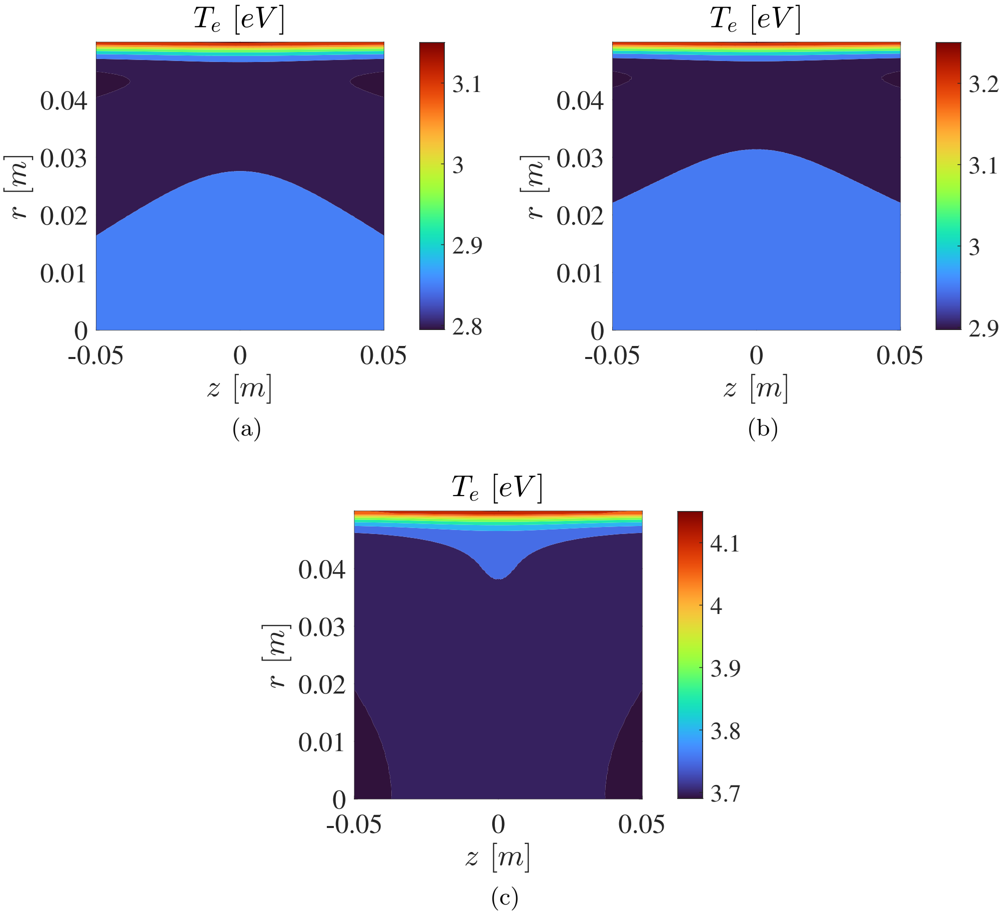

(a) (b) (c)

Figure 7.3: Electron temperature (T_e) within the Helicon source as a function of the radial (r) and axial (z) coordinates. a) OLD, b) CM, and c) CRM chemical models.

Model	T [mN]	I_{sp} [s]
OLD	59.6	1101
CM	59.9	1104
CRM	40.6	741

Table 7.2: Propulsive performance obtained using three different plasma chemistry models.

7.2 Energy equation

In Magarotto [70], the energy equation was determined according to the quasi-isotherm hypothesis. In the model presented in this work, a more general formulation is proposed in which the contribution of the heat flux is taken into account (see Eq. 6.2b). In the following, the plasma chemistry is handled according to *CM*, the anomalous transport is not considered, and the mass flow rate is $\dot{m}_0 = 5$ mg/s ($n_0 \approx 10^{20}$ m^{-3}).

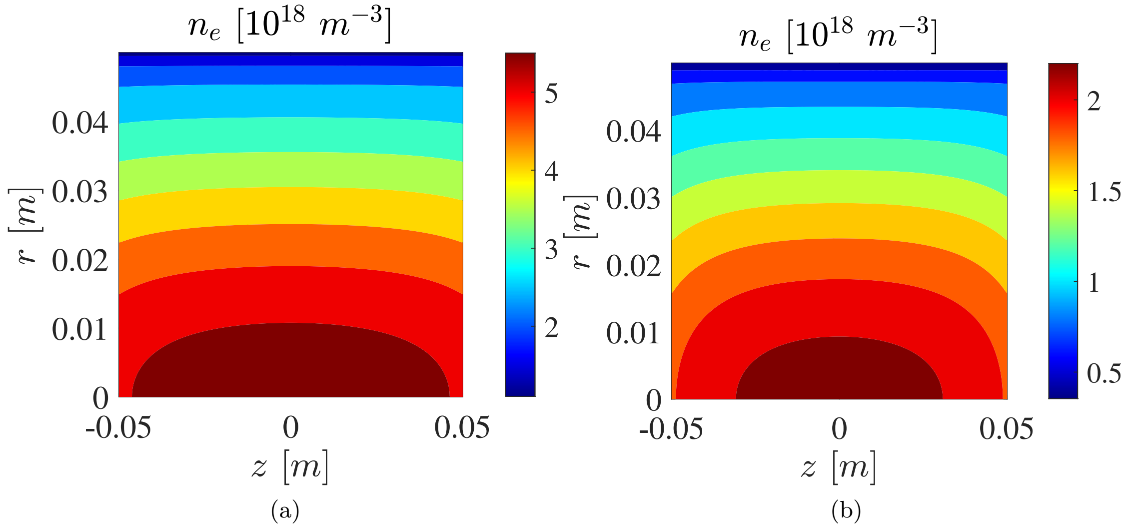

(a) (b)

Figure 7.4: Electron density (n_e) within the Helicon source as a function of the radial (r) and axial (z) coordinates. a) Q-I, and b) FE formulations of the energy equation.

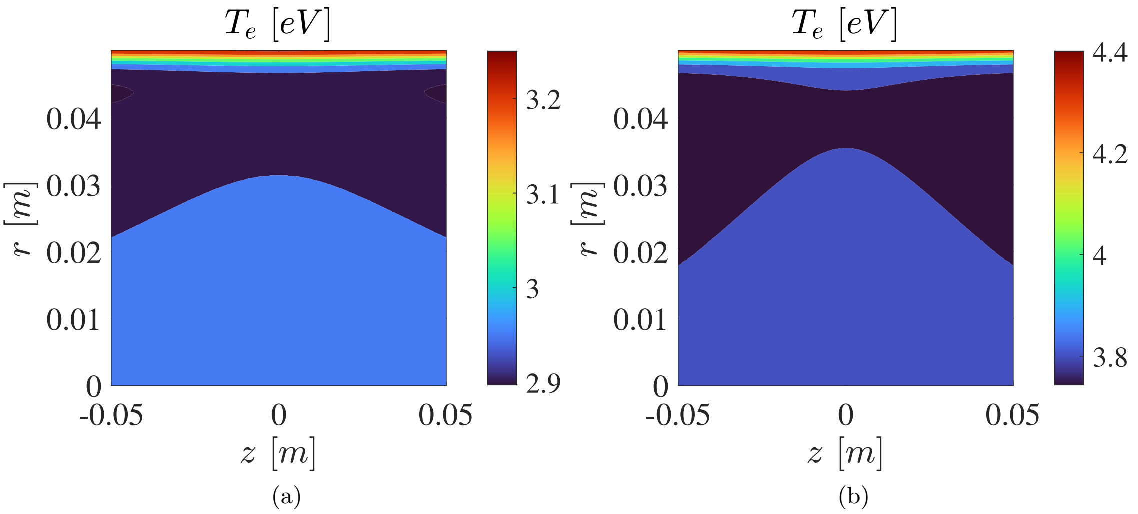

(a) (b)

Figure 7.5: Electron temperature (T_e) within the Helicon source as a function of the radial (r) and axial (z) coordinates. a) Q-I, and b) FE formulations of the energy equation.

In Fig. 7.4 and Fig. 7.5, the electron density and temperature obtained enforcing the quasi-isotherm hypothesis (referred to as Q-I) or solving the full energy equation (referred to as FE) are reported. A non-negligible difference can be seen between the two formulations. Considering FE, n_e decreases of almost 33% with respect to Q-I, and T_e increases of more than 1 eV. This result is associated to a higher energy loss predicted from FE with respect to Q-I with the assumed geometric/magnetic configuration.

7.3 Anomalous diffusion

The effects of the anomalous diffusion have been analyzed via a sensitivity analysis over the parameter α (see Eq. 6.13). The Q-I hypothesis and the CM formulation are assumed along with three different values of the mass flow rate are considered, namely $\dot{m}_0 = 0.5$, 5, 50 mg/s ($n_0 \approx 10^{19}$, 10^{20}, 10^{21} m^{-3}). In Fig. 7.6 results are depicted in terms of peak electron density and temperature, while in Fig. 7.7 thrust and specific impulse are reported. The magnitude of α affects plasma density up to 50% with the minimum in correspondence of $\alpha \approx 1$ and maximum for $\alpha = 0$. Limiting the analysis to $\alpha \leq \alpha_{Bohm} = 1/16$, n_e varies no more than 10% in function of α (the higher $\dot{m}_0$ the lower the influence of α on n_e). T_e is instead affected less than ±0.5 eV by α. This can be explained with a general lower magnetic confinement associated to the anomalous diffusion with respect to the classical formulation [228]. Consequently, the choice of α influences less than 20% the estimation of thrust and specific impulse.

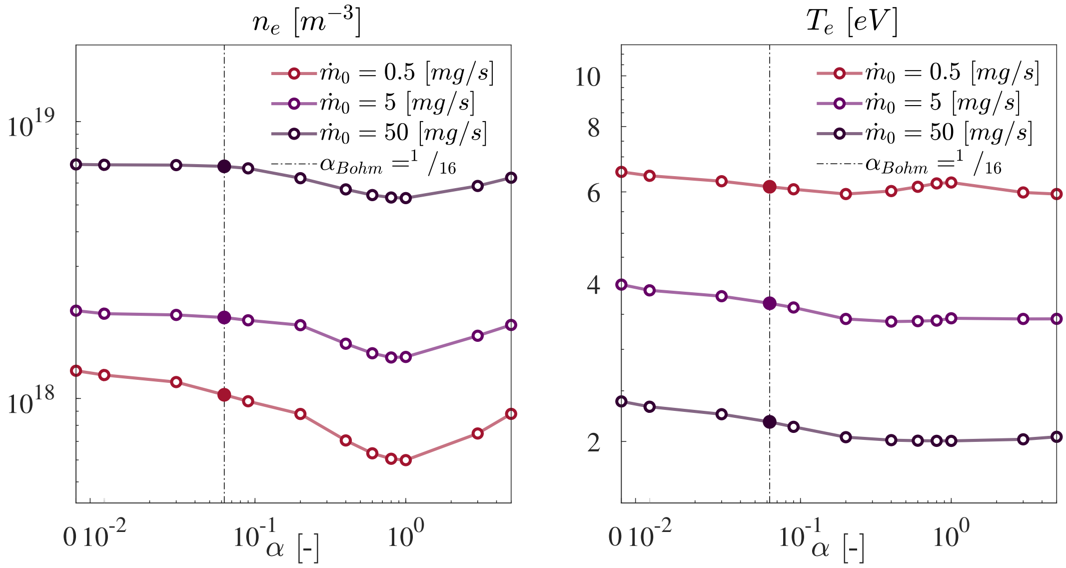

(a) (b)

Figure 7.6: a) Peak electron density n_e, b) peak electron temperature T_e as a function of the anomalous diffusion parameter α. Three values of the mass flow rate $\dot{m}_0$. The dashed line indicates $\alpha_{Bohm} = 1/16$.

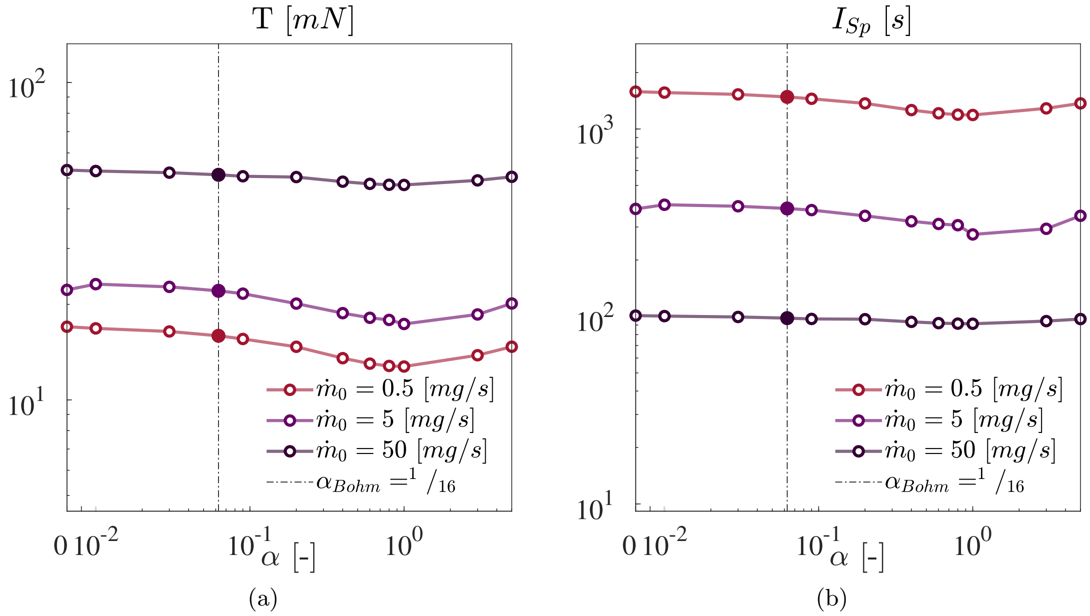

(a) (b)

Figure 7.7: a) thrust T, and b) specific impulse I_{sp} as a function of the anomalous diffusion parameter α. Three values of the mass flow rate $\dot{m}_0$. The dashed line indicates $\alpha_{Bohm} = 1/16$.

7.4 Heavy species momentum equation

In this section, several numerical approaches for the solution of the balance of mass, momentum and energy are considered for the neutrals and charged particles. Three numerical approaches to solve the heavy species mass and momentum balance equations are proposed; the first consists in the solution of the approximated Drift-Diffusion (DD) problem [39, 236], the second an explicit solution of the balance equations in a sequential fashion, and lastly a solution based on the pressure-based method SIMPLE developed by Patankar and Spalding [233, 210]. In this analysis, the heavy species energy balance is reduced to the isotherm relation [70, 209] for the sake of simplicity. For what concerns the electrons momentum equation, the drift-diffusion assumption is always employed, thus continuity and energy balance are solved by means of an explicit segregated approach. Lastly, the Poisson equation is handled through a semi-implicit scheme presented in Sec. 6.3. The different algorithms employed for solving the coupled balance equations for the heavy species were compared in terms of accuracy and computational cost.

7.4.1 Numerical strategies

Three numerical strategies have been adopted. First the Drift Diffusion approximation as shown in Sec. 6.2, has been considered for the heavy species without solving the momentum equation. The main advantage of this approach consists in the extreme simplification of the transport solution as the equations to be solved consist only in the continuity for each species (see Eq. 6.9). However, this method may be inaccurate with respect to the solution of the full momentum equation. As a matter of fact, this is the case for low pressure plasma (tenths of $mTorr$ or lower). Generally, the Drift Diffusion gains validity when the magnitude of the momentum collision frequency is several orders of magnitude higher than the total derivative in the momentum equation [220].

Second, the heavy species' momentum equation and continuity equation have been directly solved, in an explicit segregated fashion (EXP). The main issue of this methodology consists in the lack of a coupling algorithm of the equations' solution. For instance, if the momentum equation is solved at a certain time step, there is no guarantee that the resulting velocity field, when plugged into the continuity equation, will satisfy the conservation of mass [210]. When strongly coupled problems like the plasma equations are tackled, this methodology, although simple in its implementation, requires strict space-time resolution grids. For this reason, the *CFL* condition [210] must be enforced when using this approach.

Lastly, the *Semi-implicit Method for Pressure Linked Equations* (*Simple)* algorithm [210] has been exploited to solve the coupled pressure-velocity equations for the heavy species. This algorithm consists in the iterative solution of the momentum equation and of a pressure correction equation built from the continuity, with the goal of solving both a velocity and pressure fields that satisfy the conservation of mass. First the momentum equation is solved to compute an intermediate velocity field and mass fluxes, then the pressure correction equation is solved. The pressure correction is used to correct the velocity and mass fluxes. The process is iterated until the correction fields drops to zero [210].

7.4.2 Results

For this analysis the length and radius of the HPT source are respectively $L = 0.10\ m$ and $R = 0.01\ m$. The source is filled with argon at $T_0 = 300\ K$, and pressure $p_0 = 30\ mTorr$. For the sake of the analysis of different numerical strategies, a uniform antenna's power deposition map has been considered with a power deposition density of $Pw = 10^{26}\ \frac{V}{sm^3}$. Two Helmholtz coils generate the magnetic field. The currents in the coils are inverted to generate a cusp in the middle to test the different numerical strategies in condition of strong gradients in the electron fluxes that drive the plasma transport. The peak of the magnetic field is $B_0 = 0.05\ T$, and the topology is shown in Fig. 7.8.

Parameters of the simulations	
R	0.01 m
L	0.10 m
B_0	0.05 T
T_0	300 K
p_0	30 mTorr

Table 7.3: Parameters used in the simulations of the Helicon Source.

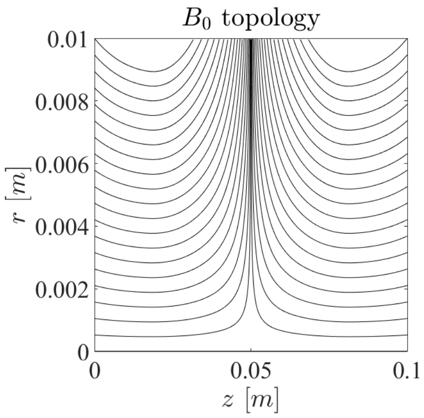

Figure 7.8: Magnetic topology with the Helmholtz inverted currents.

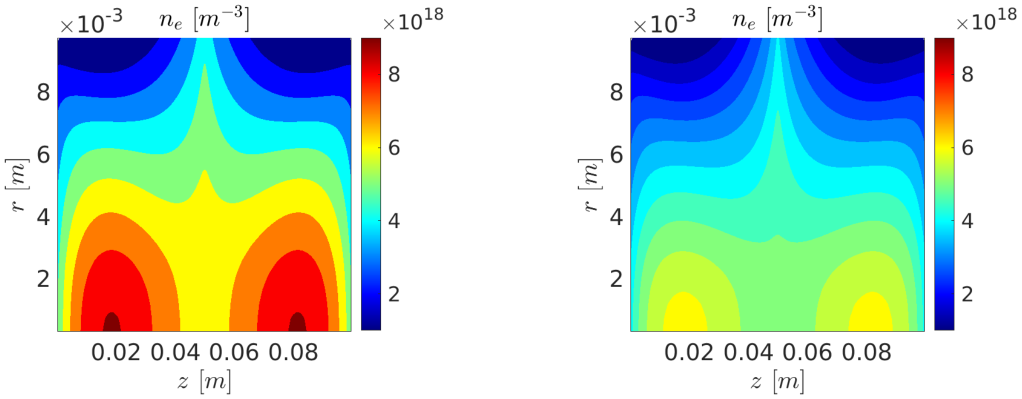

(a)

(b)

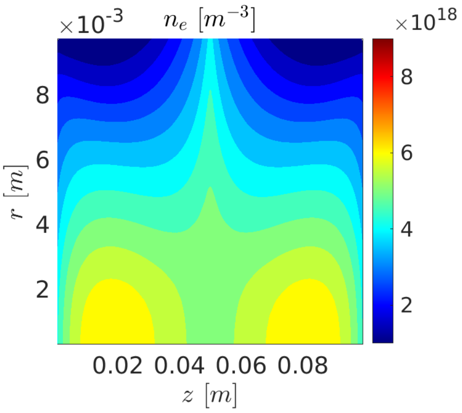

(c)

Figure 7.9: Electron density map computed with a) Drift-Diffusion, b) Explicit method, c) Simple algorithm.

The simulation strategies described in Sec. 7.4.1, namely the Drift Diffusion (DD), the explicit segregated solver (EXP) and the Simple algorithm (SMP), have been employed in the simulation of the HPT source. In Fig. 7.9-7.10 are shown respectively the electron density and temperature profiles calculated with the DD, EXP and SMP strategies. The physical trends of all the methods are quite in agreement with what expected in reality, although notable difference can be seen in the magnitude of the density and temperature profiles. The difference between the peak of electron density between the DD and the EXP case is about 38%, whereas the difference between the EXP and the SMP case is about 4.4%. It can be seen that the DD provides results notably different with respect to the solution of the full momentum equation and this is likely due to the drop of the temporal and spatial gradients which in low pressure plasma can be non-negligible. Analogous considerations apply to the electron temperature and the effects can be seen also in the propulsive performance (see Tab. 7.4).

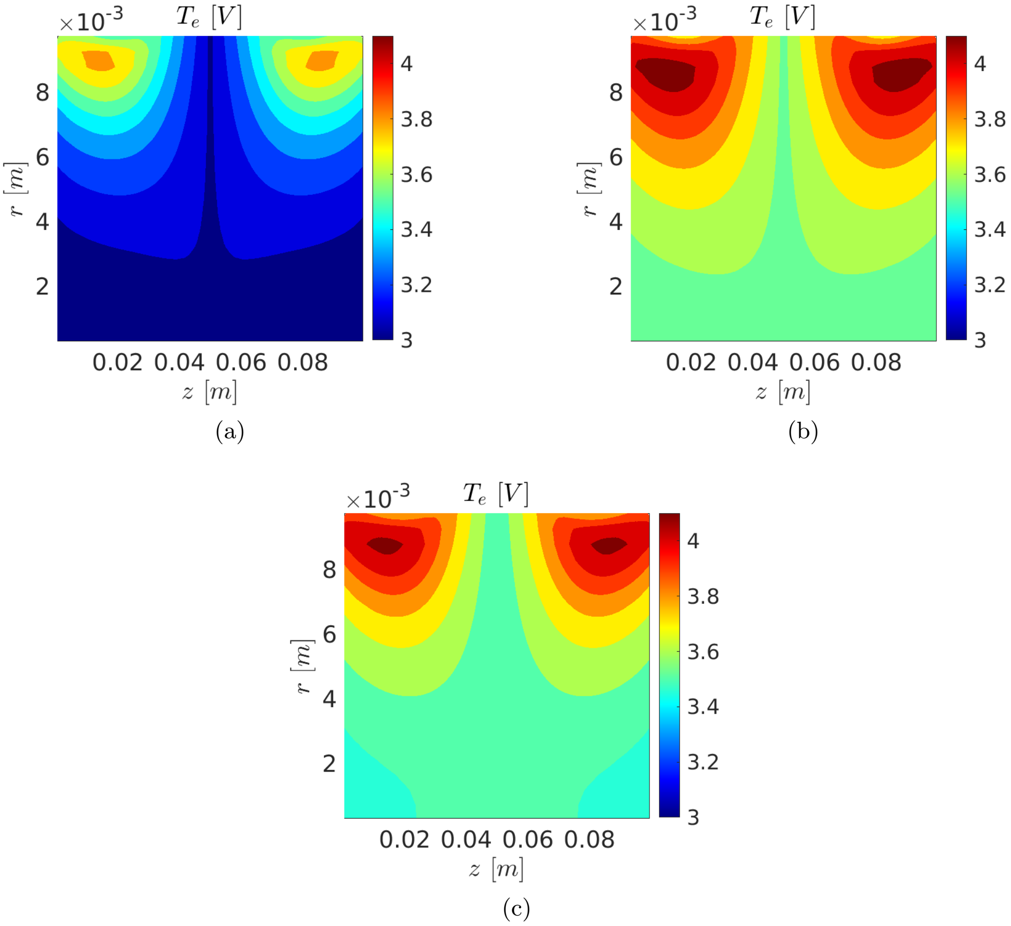

(a)

(b)

(c)

Figure 7.10: Electron temperature map computed with a) Drift-Diffusion, b) Explicit method, c) Simple algorithm.

Regarding the computational efficiency, the DD solution required 200 s to reach convergence, whereas the EXP solution required 700 s. The SMP solution converged in only 70 s being thus the most computationally efficient of the different simulation strategies. This is mainly due to the fact that the SMP method separates the pressure and velocity calculations and updates them iteratively, which allows for a larger time step to be taken, leading to faster convergence and reduced computational time. Additionally, the SMP method does not require the inversion of large matrices, as the pressure correction equation is solved using a simple iteration process [210]. This reduces the computational load compared to explicit methods and generally makes the SMP method a more efficient option for solving the momentum equations.

Model	Thrust [mN]	Specific impulse [s]	Computational time [s]
DD	6.32	359	200
EXP	4.50	426	700
SMP	4.69	423	70

Table 7.4: Propulsive data computed with the different numerical strategies and related computational time.

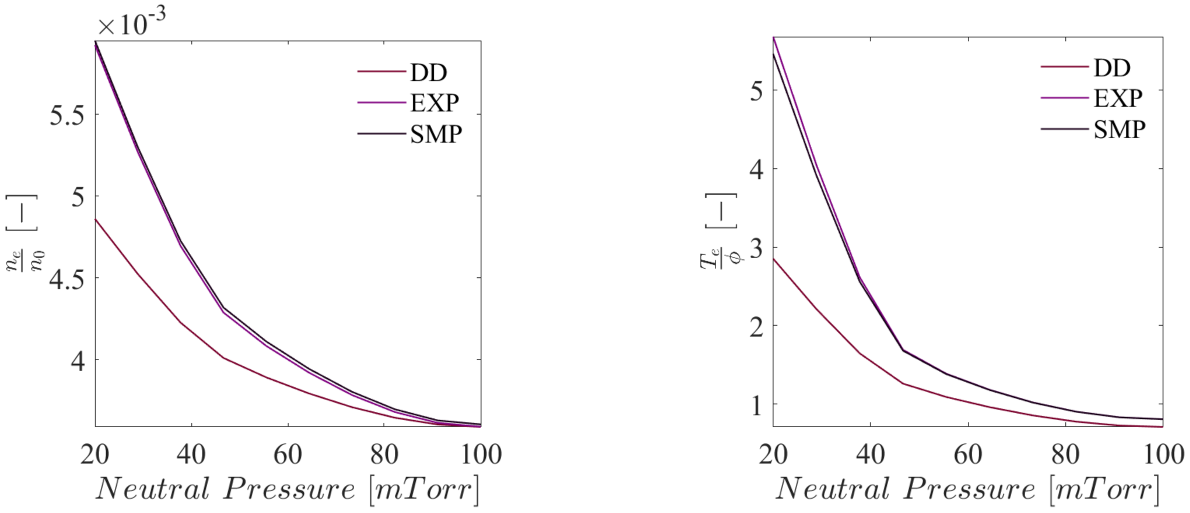

(a)

(b)

Figure 7.11: Sensitivity analysis of the different fluid approaches: a) electron density normalized with the neutral density; b) electron density normalized with the electrostatic potential.

Finally, a sensitivity analysis has been carried out over the neutral pressure to assess the range of validity for each numerical approach. The simulation setup is kept the same, however the neutral pressure is varied from 20 mTorr (low pressure) to 100 mTorr (high pressure). In Fig. 8.1, the normalized plasma density and temperature are shown for all the approaches. It can be noted that increasing neutral pressure all the proposed approaches converge to the same solution, whereas at low pressure regime the DD diverges with respect to the EXP and SMP of about 20% in the normalized electron density and of 66% in the normalized electron temperature. This is due to the fact that the DD neglects the material derivative in the momentum equation assuming that the collision frequency is way higher. However, in low pressure regime the plasma becomes weakly collisional and therefore the convective gradients cannot be neglected. At higher pressure, the collisional regime is higher and the DD solution becomes similar to the other approaches where the momentum equation is solved without further assumptions.

7.5 Discussion

The effect produced by different formulations of the plasma chemistry model, the electron energy equation, and the diffusion coefficients on the electron density and temperature profiles, along with the thrust and the specific impulse in case of a medium-low power HPT [8] has been assessed. To this end, a simplified Helicon source for space application has been studied, plasma profiles are computed with the FLUID module presented in Chapter 6, and the propulsive performance is estimated with the analytical model shown in Sec 2.2. Lumping different excitation levels in one or three equivalent species has a minor effect on the results of the simulation (n_e and T_e affected for less than 5%). On the contrary, the energy losses due to radiative decay reactions affect the propulsive performance up to 40%. Formulating the electron energy equation with the quasi-isotherm hypothesis or accounting for the heat flux results in estimations of the electron density that differ for about 30%. Defining the diffusion coefficients according to the classical formulation or the anomalous transport does not have a major influence on the propulsive performance (<20%).

Finally, for what concerns the solution of the momentum equation for the heavy species different numerical strategies have been considered, namely the DD, the explicit segregated solver and the Simple algorithm, while the electrons have been solved with the Drift-Diffusion assumption. For every analysis, the HPT source has been evaluated in terms of electron density, electron temperature, and propulsive performance, namely thrust. The DD strategy showed notably different behavior with respect to the other two methods probably due to neglecting the total time derivative in the momentum equations. The EXP and SMP provided very similar results with little difference in the plasma profiles, however the SMP showed to be the most computationally efficient among the three methods with computation times of one order of magnitude lower with respect to the DD and EXP. Moreover, a sensitivity analysis of the different strategies has been performed over the neutral pressure in order to assess the validity of each approach both at weak and high collisional regime. The DD showed that neglecting the convective gradients in the momentum equations leads to considerable divergence from the solution with the full momentum equation at low pressure regime, being this due to the low collisional regime to be expected at lower pressures. Therefore, one must always solve the full momentum equation without further assumptions on the convective gradients when dealing with low pressure discharges to accurately predict the plasma parameters and finally the thruster's performance.

Chapter 8

Validation of the numerical approach

8.1 Experiment/simulation set-up

The numerical strategy proposed in Chapter 6 has been benchmarked against experimental data collected on a Helicon source, namely the Piglet reactor analysed in the work of Lafleur [237]. Since the reported experiment was carried out on a reactor (i.e., not a thruster), the propulsive performance is not considered, and the validation is rather targeted on the prediction of the plasma profiles within the reactor. The setup is composed of a discharge camber (i.e., a dielectric tube) in which the plasma is produced and heated up, along with an expansion chamber. The discharge chamber is long 0.2 m with a diameter of 0.136 m, and is driven by a double-saddle antenna wrapped around the dielectric tube. The antenna powered at 250 W and at a frequency of 13.56 MHz generates the plasma within the discharge chamber. Two 500 turns electro-magnet coils surrounds the RF antenna and are employed to generate the confining magneto-static field; more specifically two configurations have been considered, namely the *Source Coil* and *Exhaust Coil* (see [237, Fig. 1] for further details). Both the configurations generate a magnetic field of intensity up to 2.1 mT. The source is filled with argon through a port in the diffusion chamber, and the gas pressure is 2.7 mTorr. The electron density has been measured along the axis of the discharge with a Langmuir probe operated in ion saturation mode. For further details on the experimental setup see Lafleur [237]. In Table 8.1, the input parameters considered for the numerical simulation are reported, and in Fig. 8.1a-8.1b the resulting magnetic field of the two configurations employed in the experiment [237], namely the *Source Coil* and *Exhaust Coil*, are shown. The generalized formulation of the energy equation is assumed, the *Collisional Radiative* chemistry model discussed in Sec. 6.2.2 has been adopted, and the anomalous diffusion correction (see Sec. 6.2.3) is considered with $\alpha = 1/16$. The power deposition profile is calculated with the EM module, and not assumed, in order to be more adherent with reality. The plasma transport is handled with the FLUID module and the whole simulation is carried out through the iterative convergence cycle described in Sec. 6.1. Regarding the chemistry data considered for the simulations, the reaction rates coefficients reported in Chapter 3 have been adopted. All the boundaries of the

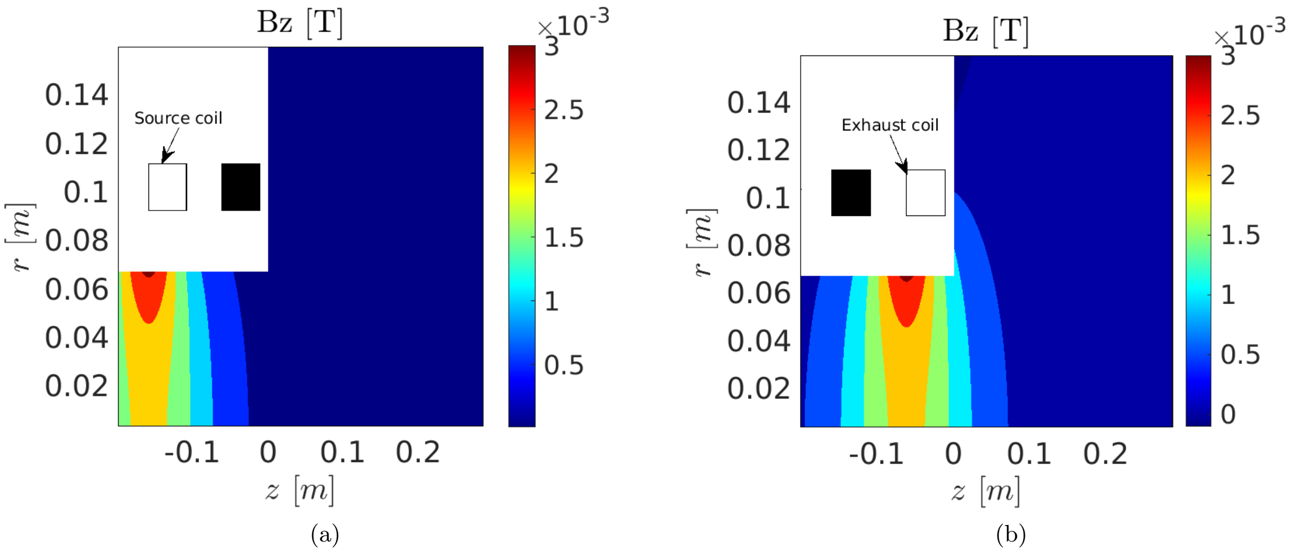

(a)

(b)

Figure 8.1: Axial intensity (B_z) of the magnetic field generated by: a) source coil; b) exhaust coil.

simulation domain have been treated as walls (see Sec. 6.2.4). Finally, the *SIMPLE* momentum coupling strategy discussed in Sec. 7.4 is employed for both the neutrals and the excited species, while the ions are solved through the *Explicit Segregated* method. The fluid domain consists of a 2D-axisymmetric structured hexa-mesh of 11000 elements. For what concerns the EM domain, the source is made of an unstructured mesh of about 10000 tetrahedral elements.

Parameter	Value
Source diameter	0.136 m
Source length	0.2 m
Expansion chamber diameter	0.320 m
Expansion chamber length	0.288 m
RF input power	250 W
Antenna frequency	13.56 MHz
Magneto-static field (axis peak)	2.1 mT
Gas pressure	2.7 mTorr

Table 8.1: Input parameters used to simulate the Piglet reactor [237].

8.2 Results

The numerical strategy presented in Chapter 6 has been compared against the measurement performed on a Piglet Helicon reactor [237]. In particular, the benchmark is done in terms of the electron density profiles measured on the axis of the Helicon reactor. The measurements were performed by means of a Langmuir probe aligned with the reactor's axis and the measurement sweeps were such to sample the electron density in different axial positions. For comparison, the results obtained with the formulation of the FLUID module proposed in Magarotto [70] have been reported as well in Fig. 8.2-8.3 (labelled as *Old*).

In Fig. 8.2, the plasma density profile (labelled as *New*) obtained in the *Source coil* configuration and the reference experimental data are depicted. The electron density is peaked in the source region (i.e., $z < 0$ m) under the coil and the antenna. More specifically, the peak is positioned on the reactor's axis, i.e., where the Langmuir probe is positioned. In Fig. 8.2b, the plasma density on the axis of the discharge is depicted. The experimental values are well reproduced by the numerical results, both in terms of physical trends and magnitude. In fact, the maximum deviation of the numerical results from measurements registered on the peak intensity is about 24% whereas the deviation of the results predicted with the *Old* model, is roughly 78%. Also in the *Exhaust Coil* configuration, the electron density profile predicted numerically is peaked in the source region in proximity of the axis as shown in Fig. 8.3a. Moreover, the trend predicted numerically is in very good accordance with the experimental one (see Fig. 8.3b) and the computed peak of electron density deviates roughly of 25% from the experimental one, whereas the *Old* model deviates of 55%.

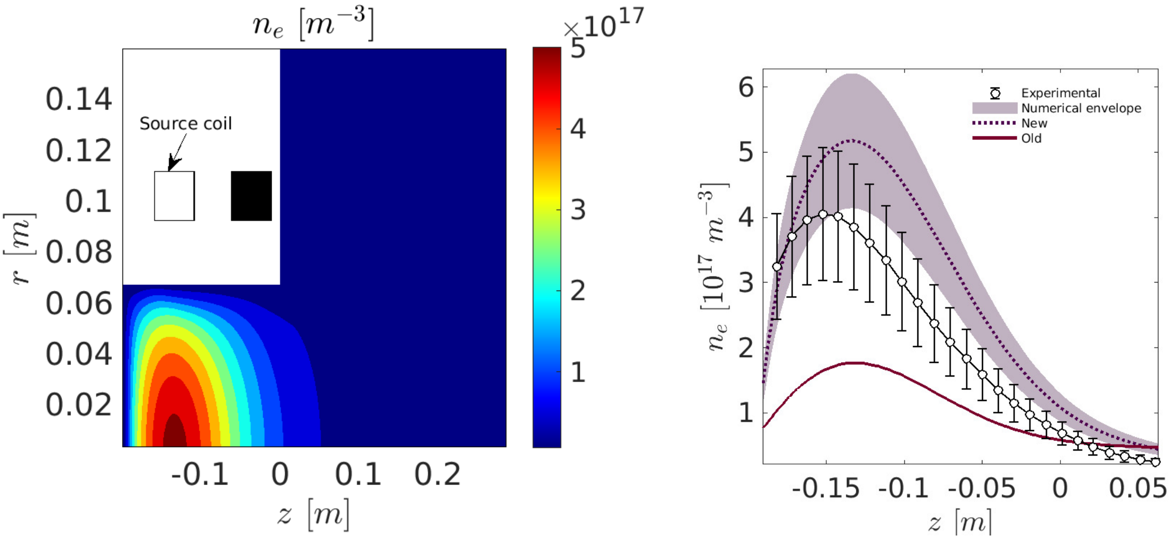

(a) (b)

Figure 8.2: a) The electron density profile (n_e) calculated numerically, and b) the computed electron density on the axis of the discharge, when the magneto-static field is generated by the *Source Coil* (dotted line) compared against the experimental data (open circles), and the *Old* model (solid line).

The uncertainty related to the experimental measurements are not explicitly reported in the reference paper [237]. Nevertheless, an uncertainty of ±25% was considered for this analysis, as discussed in Magarotto et al [70]. For what concerns the simulations, a confidence interval (referred to as numerical envelope) of about ±20% has been associated to the numerical results. The first source of numerical uncertainty is due to cross-sections. The variance associated to the choice of this parameter from different sources may be significant as already demonstrated in Chapter 3. Moreover, an additional source of uncertainty is related to further approximations on the input parameters of the model. The assumption of Maxwellian distribution function for the electrons may not always be accurate, e.g., this is particularly true in proximity of the walls where the sheath forms [238], and in the expansion chamber where a bi-Maxwellian might occur [70]. In addition, the hypothesis of non-magnetized ions might affect the results as well. However, each of these errors is expected to be in the order of few percent points [70].

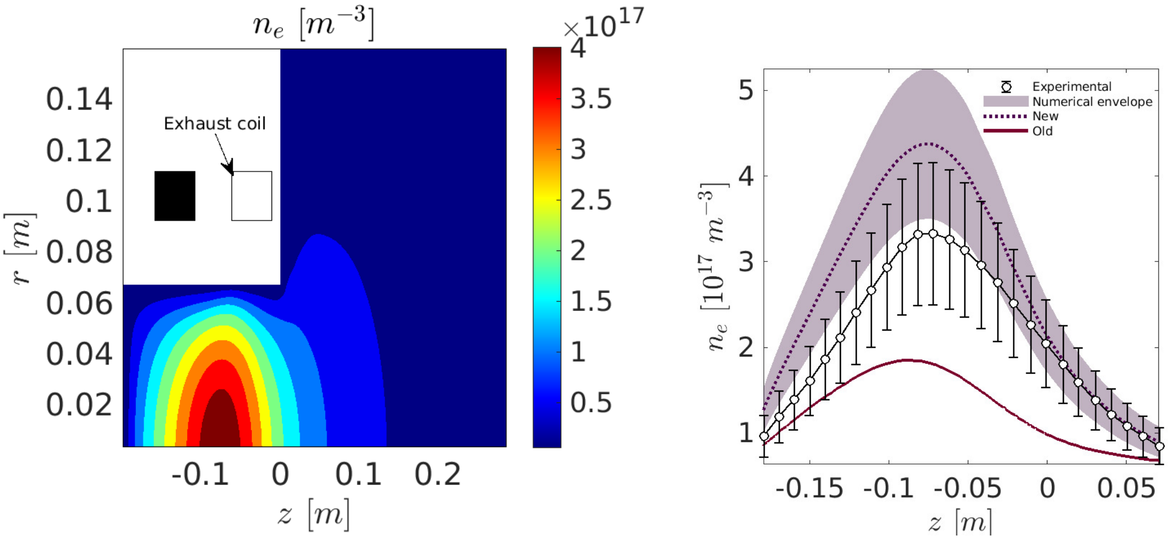

(a) (b)

Figure 8.3: a) The electron density profile (n_e) calculated numerically, and b) the computed electron density on the axis of the discharge, when the magneto-static field is generated by the *Exhaust Coil* (dotted line) compared against the experimental data (open circles), and the *Old* model (solid line).

Finally, the power deposition, the electron temperature and the ion temperature profiles have been reported for both the *Source Coil* and the *Exhaust Coil* cases (see respectively Figs. 8.4 and 8.5). In the reference paper [237] there are no data to benchmark these predictions, nonetheless the analysis of these results can give useful insights on the plasma behavior in this reactor. First, it can be seen that the deposited power density is not significantly influenced by the topology of the magnetic field: for both the configurations (see Fig. 8.4a and Fig. 8.5a) the power peak is located in the source region close to the edge of the discharge, i.e., near the antenna location. More significant differences can be noticed on the plasma temperature profiles (see Fig. 8.4b-8.4c and Fig. 8.5b-8.5c) which are clearly influenced by the magnetic topology. The position of the electron temperature peak is located near the deposited power peak but shifted in proximity of the active coil in both the configurations. Therefore, it can be concluded that the magnetic field topology affects more the electron density and temperature profiles (i.e., the plasma transport) than the power deposition. For what concerns the ions, it can be noted that the peak follows the electrons' one. However, there is no direct correlation between the ions and the deposited power as there is for the electrons, i.e., R_ε directly drives the electron energy equation (see Eq. 6.2b) but not the ion energy (see Eq. 6.7c). In fact, the main mechanism of energy transfer toward the ions consists in the electron collisions.

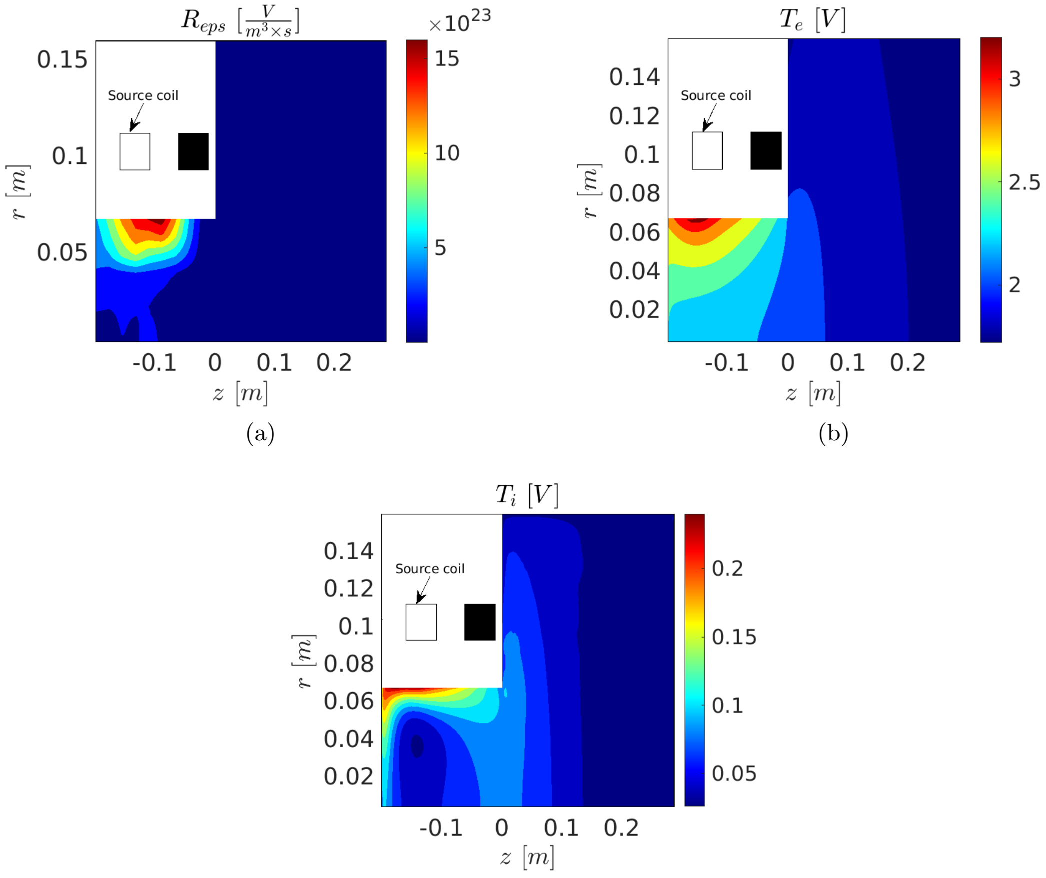

(a)

(b)

(c)

Figure 8.4: The profiles of a) deposited power ($\mathcal{R}_{pow}$), b) the computed electron temperature (T_e), and c) the computed ion temperature (T_i) when the magneto-static field is generated by the *Source Coil*.

To conclude, the numerical predictions and the experimental measurements have shown an excellent agreement. The physical trends are well reproduced and the quantitative differences between the numerical and experimental results is always within the uncertainty bands. In fact, the numerical envelope and the measurements uncertainty band are always overlapped. In addition, it has been shown numerically that the magnetic topology influences more the plasma transport rather than the power deposition. To further improve the agreement between numerical and experimental measurements, several strategies can be adopted. First, the assumption of a Maxwellian distribution for the plasma particles

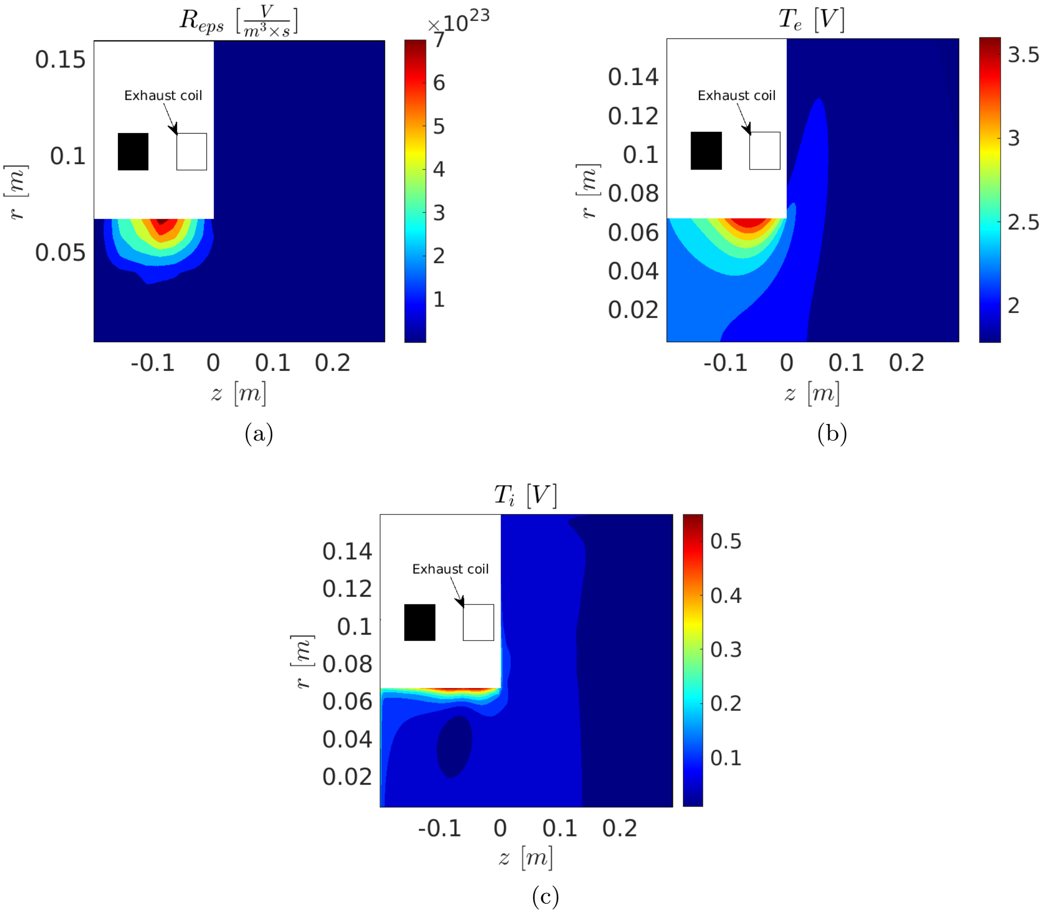

Figure 8.5: The profiles of a) deposited power ($\mathcal{R}_{pow}$), b) the computed electron temperature (T_e), and c) the computed ion temperature (T_i) when the magneto-static field is generated by the *Exhaust Coil.*

is a simplification and does not always hold in real plasma systems. Plasma particles in a Helicon Plasma Thruster may exhibit deviations from a Maxwellian distribution due to a variety of physical processes [92], such as non-uniform heating, cooling, and acceleration. These deviations can have a significant impact on the plasma properties, such as the density, temperature, and velocity distributions, and can therefore affect the accuracy of the numerical predictions. To account for non-Maxwellianity, more sophisticated models that consider the deviation from Maxwellian distributions can be employed. For example, bi-Maxwellian [237] or Kappa distributions [239] can be used to represent the particle distributions in the plasma. These models can provide a better description of the plasma particles and can result in improved numerical predictions compared to using a Maxwellian distribution alone. In addition, advanced diagnostic techniques can be used to measure the plasma properties in the experiments and validate the non-Maxwellian models used in the numerical simulations. This can help to further improve the accuracy of the numerical predictions and the agreement with experimental data.

Secondly, improving the boundary conditions can also play a key role in improving the agreement between experiments and numerical predictions. In particular, the boundary conditions for Poisson's equation, which governs the electric potential in the plasma, may have a significant impact on the results. Therefore, using a more accurate and refined representation of the plasma-wall interactions could lead to better agreement with experimental data.

Finally, improving the numerical methods used in the simulation can also help to improve the agreement between experiments and numerical predictions. This can involve the use of more advanced numerical schemes, such as higher order methods and Riemann HLLC methods [240] to capture the plasma physics more accurately and robustly.

Epilogue

Conclusions

In this work two main topics have been addressed:

(i) developing a *Global Model* (GM) with several chemistry models for the analysis of an HPT working with noble gases and alternative propellants;

(i) developing a multi dimensional numerical tool capable of predicting the plasma generation and transport across a HPT.

Regarding the first topic, the GM has been firstly used for the analysis of HPT working with classical propellants such as the noble gases. In this regard, two main topics have been addressed: (i) presenting a novel lumping strategy to account, in a reasonable computation time, for the dynamics of the excited states in neon, argon, krypton, and xenon low pressure (<50 mTorr) discharges; (ii) performing a sensitivity analysis to assess how cross-sections from different datasets affect the estimation of plasma parameters. Concerning the first point, the main outcome is a methodology to investigate, in a reasonable computation time (in the order of few seconds), how the dynamics of the excited states affect the estimation of plasma density and temperature in low pressure discharges. In this regard, only $1s$ and $2p$ excited states have been simulated. The fine structure energy levels have been lumped in metastable and resonant $1s$ ($1s_M$ and $1s_R$ respectively), along with $2p$. The proposed methodology relies on the assumption that LTE holds between the fine structure energy states that are lumped together. Both collisional excitation/de-excitation and radiative decay reactions have been considered, so no assumption of LTE nor Corona equilibrium is done between different lumped states [145]. The lumping methodology has been benchmarked against the results obtained treating all the excited states as separate species; differences lower than 1% have been registered. Experimental evaluations of the electron density and electron temperature have been used to validate the proposed methodology. Specifically an ICP reactor [146] operated with argon, neon, krypton and xenon has been simulated with a *Global Model.* Regarding the second point, the choice of the cross-section dataset can have a non-negligible effect on the results of the simulation, in particular if radiative decay is modelled. A maximum variance between highest and lowest density is 30%. A single set of cross-sections that gives results always closer to experiments has not been found. Therefore in Appendix A an analytical fitting of the rate coefficients that provide the highest and the lowest density for each gas has been reported.

Moreover, the HPT plasma chemistry has been tackled concerning alternative propellants such as air and iodine. Regarding the former, a chemistry set comprising reactions of both atomic and molecular oxygen and nitrogen, was implemented in the GM. Results have been verificated against numerical simulations taken from literature, showing good agreement of the numerical models, with a maximum deviation registered of 25% due to several factors such as different reactions considered in the chemistry, the diffusion models and different numerical algorithms employed in the solution of the balance equations. In addition, the on going experimental activities at the *University of Stuttgart* targeted on the characterization of an air-breathing HPT with the aim of validating the GM air chemistry, are reported. In particular, a momentum flux balance and a *B-Dot* probe have been calibrated. The first will provide thrust data that can be used for the validation of the GM with the air chemistry model, while the latter will be employed for demonstrating the propagation of the *Helicon* waves.

For what concerns iodine, the propulsive performance of *REGULUS*, an iodine fed HPT [12], has been addressed by coupling the GM and a PIC methodology. Numerical results have been quantitatively compared against experimental measurements [83]. The GM has been adapted with an iodine chemistry model, taking into account also the effects of electronegativity in the prediction of the plasma properties. Moreover, the chemistry model has been adopted also in the PIC code *Starfish.* The HPT propulsive performance have been assessed for several power inputs. The predicted results have shown to be in good agreement with the experimental data, being the maximum error of 12%, which lies in the uncertainty band of the experimental measurements.

Regarding the second topic addressed, the 3D numerical tool developed in this work, consists of two main modules, i) the EM module which provides the power deposited by the antenna into the plasma, and ii) the FLUID module, responsible of predicting the plasma profiles driven by the deposited power. The two modules run iteratively until a steady state solution is converged. This tool has been exploited for analysing a HPT in terms of physical models employed. Specifically, results provided with different formulations of the argon plasma chemistry (i.e., *Collisional Radiative Models*) lumping the excited states, the electron energy equation, and the diffusion coefficients have been quantitatively compared. The effect produced by each single aspect on the electron density and temperature profiles, along with the thrust and the specific impulse in case of a medium-low power HPT [8] has been assessed. To this end, a simplified Helicon source for space application has been studied, plasma profiles are computed, and the propulsive performance is estimated with a simplified analytical model [44]. Lumping different excitation levels in one or three equivalent species has a minor effect on the results of the simulation (n_e and T_e affected for less than 5%). On the contrary, the energy losses due to radiative decay reactions affect the propulsive performance up to 40%. Formulating the electron energy equation with the quasi-isotherm hypothesis or accounting for the heat flux results in estimations of the electron density that differ for about 30%. Defining the diffusion coefficients according to the classical formulation or the anomalous transport does not have a major influence on the propulsive performance (<20%).

Furthermore, an analysis on the solution of the momentum equation (FLUID module) for the heavy species, i.e., ions, exciteds and neutrals, was addressed. Different numerical strategies have been considered, namely the Drift Diffusion (DD), the explicit segregated solver (EXP) and the Simple algorithm (SMP), in the simulation of a typical HPT source. For every analysis, the source performance has been evaluated in terms of electron density, electron temperature, and propulsive performance, namely specific impulse and thrust. The DD strategy showed notably different behavior with respect to the other two methods probably due to neglecting the total time derivative in the momentum equations. The EXP and SMP provided very similar results with little difference in the plasma profiles (less than 5%), however the SMP showed to be the most computationally efficient among the three methods with computation times of one order of magnitude lower with respect to the DD and EXP.

In conclusion, results provided by the numerical tool with the generalized formulation of the FLUID module have been benchmarked against measures of the electron density performed on a Piglet reactor [237]. To this end, both the plasma transport and the power deposition profiles are solved and simulations are carried out through the iterative convergence cycle described in Sec. 6.1. The experimental trend is reproduced by numerical results for the reactor in two different configurations of the magnetic topology, namely the *Source coil* and *Exhaust coil* cases [237]. Generally, an excellent agreement of the physical trends of the numerical predictions against the measured data, is observed. For both the cases the disagreement on the plasma density peak is lower than 25%, and the profiles always within the uncertainty band of the measures.

Finally, it is worth mentioning that self-consistent numerical tools capable of simulating the plasma dynamics in RF sources are of interest not only for space applications, but also in the fields of material processing [105], lightning [241], along with radar and telecommunications [242, 243, 244, 245, 246].

Future developments

The GM has proven to be a satisfactory tool for gaining macroscopic insights on the physics and the performance of HPTs fed with traditional and alternative propellants. Nevertheless, a number of future developments must be accounted. First, the air chemistry model must be properly validated against experimental data. To this end, an experimental campaign is currently undergoing at the *University of Stuttgart* with the aim of collecting data for a proper validation. For what concerns both air and iodine chemistry models, a future work must be dedicated on finding accurate cross-section for the reactions involved in the model. This may be done via spectroscopic experiments [97] or through calculations with quantum methodologies [247].

Moreover, the chemistry model addressed in this work will be implemented on the 3D numerical strategy presented. In this way, it will be possible to accurately simulate the HPT fed with alternative propellants. Nevertheless, the 3D numerical strategy presented in Sec. 6.1 will be further improved also in terms of numerical and physical models. The boundary conditions for the FLUID model will be properly addressed. Physical models accounting for phenomena such as the *Secondary Electron Emission* and more realistic *sheath* models [238] will be analyzed. For what concerns the balance equations, other approaches will be considered and in particular the density methods like the HLLC Riemann methodology [210] as they are well suited for highly compressible fluids, such as plasma. Finally, since in the plume the distribution function of the charged particles can significantly depart from the Maxwellian [68, 69] and the plasma density is order of magnitudes lower than in the production stage [42], a PIC strategy might be the best candidate to obtain accurate propulsive performance data with reasonable computing time. Therefore, the numerical code SPIS [248] will be employed and coupled with the FLUID module by means of proper boundary conditions. Once the FLUID module and the PIC will be integrated, the numerical tool will be employed to optimize the design of the thruster, namely both *Production Stage* and *Acceleration Stage*, in order to improve the thruster's efficiency and propulsive performance. In conclusion, a comparison of the models will be made with respect to experimental measurements of a HPT fed with xenon, iodine and air for a thorough validation.

Novelty

Finally, it is worth highlighting the innovative contributions associated with this research work:

(i) The development of a GM with several chemistry models to analyze the performance of a HPT fed with both noble gases such as argon, neon, krypton and xenon and innovative propellants such as iodine and air. For what concerns the former, a novel lumping methodology has been developed. This can be used for dramatically reducing the computational cost without affecting accuracy when modelling the excited species in the plasma chemistry for both GM and multidimensional codes. Regarding iodine, this propellant is becoming of great interest as a valid alternative to xenon in the electric propulsion field, therefore there is a growing need for models capable of predicting the thruster performance accounting for its chemistry. In this regard, a GM with an iodine chemistry set has been developed and cross-sections and reaction rates have been collected from literature as well. Thanks to this numerical tool it is possible to design novel thrusters target at the utilization of iodine propellant and perform preliminary optimizations. For what concerns air, this raised a great deal of interest recently, due to the application of air-breathing technology [18]. In this regard, a chemistry model has been set collecting data, namely cross-sections and transport coefficients, from literature and a GM capable of simulating a HPT has been developed. This tool allows the preliminary estimation of an air-breathing thruster performance and can be used to assess both propulsion and system analysis of the thruster operating at various altitudes. Therefore this tool can provide a valid contribution in enabling the air-breathing technology with HPT and generally any RF plasma thruster.

(i) The development of a 3D numerical code capable of simulating an HPT in terms of plasma generation and transport. It is one of the very few self-consistent (i.e., which resolves both the EM wave propagation and plasma transport) numerical tools which can handle Helicon sources. In particular it is the only which can (i) treat discharges with a generic 3D geometry, and (ii) model the actual RF antenna, solving the current distribution thereof. In addition, the code can resolve generic plasma sources driven by RF antennas (e.g., ICPs and CCPs [30]) if all the plasma species can be considered Maxwellian. Furthermore, the FLUID module stand-alone can also simulate DC discharges [30], provided that the Maxwellian hypothesis is respected.

Appendices

Appendix A

Ar, Ne, Kr, Xe: fitting of the rate coefficients

The rate coefficients obtained from the cross-section datasets referring to the highest and lowest density cases (see Sec. 3.3) have been fitted using a polynomial form that reads,

$$K(T_e) = \sum_{i=0}^{n} p_i T_e^i \tag{A.1}$$

With $n = 6$, Eq. (A.1) holds true in the range $T_e = [1, 20]$ eV for both argon, neon, krypton and xenon. The fitting coefficients (p_i) refer to the collisional-radiative case; for the highest density they are reported in Tab. A.1-A.4, for the lowest density in Tab. A.5-A.8. The inverse reactions (i.e., de-excitation) rate coefficients, can be computed using the *Principle of Detailed Balancing* (PDB) and assuming a Maxwellian EEDF. The rate coefficient formula can be expressed as [139]:

$$K_{ji} = K_{ij} \frac{g_i}{g_j} exp\left(\frac{U_j - U_i}{qT_e} \right) \tag{A.2}$$

Table A.1: Lumped rate coefficients fitting constants for the highest density case in argon.

Transition [1][2]	p_6	p_5	p_4	p_3	p_2	p_1	p_0	Ref. [3]
$gs \rightarrow 1s_m$	5.127×10^{-23}	-5.266×10^{-21}	2.019×10^{-19}	-3.647×10^{-18}	2.973×10^{-17}	-5.543×10^{-17}	2.173×10^{-17}	[155, 156]
$gs \rightarrow 1s_r$	-3.619×10^{-22}	1.990×10^{-20}	-3.379×10^{-19}	1.653×10^{-19}	4.994×10^{-17}	-1.256×10^{-16}	5.670×10^{-17}	[155, 156]
$gs \rightarrow 2p$	-2.801×10^{-22}	1.408×10^{-20}	-1.841×10^{-19}	-1.287×10^{-18}	4.144×10^{-17}	-1.017×10^{-16}	4.653×10^{-17}	[154]
$1s_m \rightarrow 1s_r$	6.448×10^{-20}	-4.580×10^{-18}	1.301×10^{-16}	-1.891×10^{-15}	1.496×10^{-14}	-6.403×10^{-14}	1.443×10^{-13}	[155, 156]
$1s_m \rightarrow 2p$	4.237×10^{-20}	-1.939×10^{-18}	1.204×10^{-17}	7.987×10^{-16}	-2.037×10^{-14}	2.320×10^{-13}	-7.235×10^{-14}	[155, 156]
$1s_r \rightarrow 2p$	1.030×10^{-19}	-6.072×10^{-18}	1.228×10^{-16}	-6.799×10^{-16}	-1.011×10^{-14}	1.962×10^{-13}	-6.453×10^{-14}	[155, 156]
$gs \rightarrow ion$[4]	-6.207×10^{-21}	4.196×10^{-19}	-1.069×10^{-17}	1.179×10^{-16}	-3.352×10^{-16}	2.636×10^{-16}	-2.385×10^{-17}	[154]
$1s \rightarrow ion$	8.383×10^{-20}	-5.591×10^{-18}	1.441×10^{-16}	-1.762×10^{-15}	9.393×10^{-15}	-1.789×10^{-15}	-2.626×10^{-15}	[168]
$2p \rightarrow ion$	1.57×10^{-19}	-9.773×10^{-18}	2.254×10^{-16}	-2.218×10^{-15}	5.157×10^{-15}	5.868×10^{-14}	-3.014×10^{-14}	[168]
$0 \rightarrow 0$[5]	1.255×10^{-19}	-8.225×10^{-18}	2.047×10^{-16}	-2.31×10^{-15}	9.416×10^{-15}	2.265×10^{-14}	-7.953×10^{-15}	[154]

[1] Transitions refer to electronic collisional reactions.

[2] Reverse transitions shall be derived using the *Detailed Balance Principle.*

[3] Reference refer to the set of cross-sections considered for the actual lumped transition.

[4] Ionization by electron collision.

[5] Elastic scattering of neutral particles.

Table A.2: Lumped rate coefficients fitting constants for the highest density case in neon.

Transition [1][2]	p_6	p_5	p_4	p_3	p_2	p_1	p_0	Ref. [3]
$gs \rightarrow 1s_m$	-2.883×10^{-23}	1.588×10^{-21}	-2.782×10^{-20}	8.359×10^{-20}	1.912×10^{-18}	-5.746×10^{-18}	2.879×10^{-18}	[155, 156]
$gs \rightarrow 1s_r$	-1.643×10^{-22}	1.086×10^{-20}	-2.686×10^{-19}	2.811×10^{-18}	-6.025×10^{-18}	8.802×10^{-19}	2.045×10^{-18}	[155, 156]
$gs \rightarrow 2p$	-1.104×10^{-22}	7.115×10^{-21}	-1.691×10^{-19}	1.662×10^{-18}	-3.407×10^{-18}	-1.259×10^{-19}	1.638×10^{-18}	[155, 156]
$1s_m \rightarrow 1s_r$	-	-	-	-	-	-	-	-
$1s_m \rightarrow 2p$	1.141×10^{-20}	5.107×10^{-19}	-6.216×10^{-17}	1.803×10^{-15}	-2.367×10^{-14}	1.500×10^{-13}	-5.824×10^{-14}	[170]
$1s_r \rightarrow 2p$	2.029×10^{-19}	-1.064×10^{-17}	1.635×10^{-16}	3.213×10^{-16}	-3.217×10^{-14}	3.097×10^{-13}	-1.293×10^{-13}	[170]
$gs \rightarrow ion$[4]	-1.068×10^{-22}	1.109×10^{-20}	-4.296×10^{-19}	7.386×10^{-18}	-3.496×10^{-17}	5.561×10^{-17}	-2.115×10^{-17}	[165]
$1s \rightarrow ion$	5.721×10^{-20}	-3.886×10^{-18}	1.027×10^{-16}	-1.308×10^{-15}	7.525×10^{-15}	-5.076×10^{-15}	-1.139×10^{-16}	[168]
$2p \rightarrow ion$	1.55×10^{-19}	-9.868×10^{-18}	2.366×10^{-16}	-2.539×10^{-15}	9.265×10^{-15}	3.449×10^{-14}	-2.057×10^{-14}	[168]
$0 \rightarrow 0$[5]	3.175×10^{-21}	-2.326×10^{-19}	6.23×10^{-18}	-6.628×10^{-17}	-4.102×10^{-17}	8.1×10^{-15}	2.857×10^{-15}	[157]

[1] Transitions refer to electronic collisional reactions.

[2] Reverse transitions shall be derived using the *Detailed Balance Principle.*

[3] Reference refer to the set of cross-sections considered for the actual lumped transition.

[4] Ionization by electron collision.

[5] Elastic scattering of neutral particles.

Table A.3: Lumped rate coefficients fitting constants for the highest density case in krypton.

Transition [1,2]	p_6	p_5	p_4	p_3	p_2	p_1	p_0	Ref. [3]
$gs \rightarrow 1s_m$	-3.508×10^{-21}	2.128×10^{-19}	-4.594×10^{-18}	3.683×10^{-17}	1.321×10^{-17}	-2.538×10^{-16}	1.614×10^{-16}	[160]
$gs \rightarrow 1s_r$	-1.840×10^{-22}	8.551×10^{-21}	-8.404×10^{-20}	-1.427×10^{-18}	2.823×10^{-17}	-7.101×10^{-17}	3.368×10^{-17}	[160]
$gs \rightarrow 2p$	-1.875×10^{-21}	9.642×10^{-20}	-1.419×10^{-18}	-2.471×10^{-18}	1.912×10^{-16}	-5.224×10^{-16}	2.553×10^{-16}	[160]
$1s_m \rightarrow 1s_r$	9.351×10^{-19}	-8.017×10^{-17}	2.737×10^{-15}	-4.757×10^{-14}	4.448×10^{-13}	-2.164×10^{-12}	4.700×10^{-12}	[160]
$1s_m \rightarrow 2p$	3.055×10^{-19}	-1.377×10^{-17}	1.018×10^{-16}	4.098×10^{-15}	-9.285×10^{-14}	7.405×10^{-13}	-3.020×10^{-13}	[160]
$1s_r \rightarrow 2p$	-1.042×10^{-18}	7.400×10^{-17}	-2.105×10^{-15}	3.074×10^{-14}	-2.462×10^{-13}	1.062×10^{-12}	-2.401×10^{-13}	[160]
$gs \rightarrow ion$[4]	-9.064×10^{-21}	6.003×10^{-19}	-1.485×10^{-17}	1.549×10^{-16}	-3.252×10^{-16}	4.18×10^{-17}	1.116×10^{-16}	[165]
$1s \rightarrow ion$	9.019×10^{-20}	-5.965×10^{-18}	1.519×10^{-16}	-1.824×10^{-15}	9.332×10^{-15}	1.234×10^{-15}	-4.211×10^{-15}	[168]
$2p \rightarrow ion$	1.473×10^{-19}	-8.987×10^{-18}	1.997×10^{-16}	-1.788×10^{-15}	1.272×10^{-15}	7.632×10^{-14}	-3.633×10^{-14}	[168]
$0 \rightarrow 0$[5]	1.417×10^{-19}	-8.708×10^{-18}	1.951×10^{-16}	-1.77×10^{-15}	2.165×10^{-15}	4.954×10^{-14}	-1.645×10^{-14}	[163]

[1] Transitions refer to electronic collisional reactions.
[2] Reverse transitions shall be derived using the *Detailed Balance Principle*.
[3] Reference refer to the set of cross-sections considered for the actual lumped transition.
[4] Ionization by electron collision.
[5] Elastic scattering of neutral particles.

Table A.4: Lumped rate coefficients fitting constants for the highest density case in xenon.

Transition [1,2]	p_6	p_5	p_4	p_3	p_2	p_1	p_0	Ref. [3]
$gs \rightarrow 1s_m$	1.142×10^{-21}	-7.975×10^{-20}	2.172×10^{-18}	-2.846×10^{-17}	1.691×10^{-16}	-2.222×10^{-16}	6.016×10^{-17}	[153]
$gs \rightarrow 1s_r$	-1.623×10^{-21}	8.309×10^{-20}	-1.096×10^{-18}	-9.582×10^{-18}	3.141×10^{-16}	-7.064×10^{-16}	3.025×10^{-16}	[153]
$gs \rightarrow 2p$	7.969×10^{-22}	-6.896×10^{-20}	2.358×10^{-18}	-3.968×10^{-17}	3.146×10^{-16}	-5.489×10^{-16}	2.024×10^{-16}	[157]
$1s_m \rightarrow 1s_r$	2.180×10^{-21}	-5.305×10^{-20}	-2.078×10^{-18}	9.470×10^{-17}	-1.348×10^{-15}	7.811×10^{-15}	-3.385×10^{-15}	[118]
$1s_m \rightarrow 2p$	1.173×10^{-19}	-5.245×10^{-18}	4.148×10^{-17}	1.269×10^{-15}	-2.624×10^{-14}	1.791×10^{-13}	-8.287×10^{-14}	[118]
$1s_r \rightarrow 2p$	-3.960×10^{-19}	3.060×10^{-17}	-9.637×10^{-16}	1.595×10^{-14}	-1.494×10^{-13}	7.833×10^{-13}	-2.225×10^{-13}	[118]
$gs \rightarrow ion$[4]	-1.182×10^{-20}	7.33×10^{-19}	-1.627×10^{-17}	1.32×10^{-16}	2.268×10^{-16}	-1.25×10^{-15}	6.844×10^{-16}	[157]
$1s \rightarrow ion$	9.971×10^{-20}	-6.56×10^{-18}	1.657×10^{-16}	-1.963×10^{-15}	9.733×10^{-15}	4.011×10^{-15}	-5.768×10^{-15}	[168]
$2p \rightarrow ion$	1.456×10^{-19}	-8.759×10^{-18}	1.894×10^{-16}	-1.564×10^{-15}	-1.27×10^{-15}	9.049×10^{-14}	-4.146×10^{-14}	[168]
$0 \rightarrow 0$[5]	-8.535×10^{-21}	2.448×10^{-18}	-1.339×10^{-16}	3.084×10^{-15}	-3.464×10^{-14}	1.795×10^{-13}	-4.371×10^{-14}	[164]

[1] Transitions refer to electronic collisional reactions.
[2] Reverse transitions shall be derived using the *Detailed Balance Principle*.
[3] Reference refer to the set of cross-sections considered for the actual lumped transition.
[4] Ionization by electron collision.
[5] Elastic scattering of neutral particles.

Table A.5: Lumped rate coefficients fitting constants for the lowest density case in argon.

Transition [1,2]	p_6	p_5	p_4	p_3	p_2	p_1	p_0	Ref. [3]
$gs \rightarrow 1s_m$	6.176×10^{-23}	-8.633×10^{-21}	3.823×10^{-19}	-7.465×10^{-18}	6.352×10^{-17}	-1.260×10^{-16}	5.194×10^{-17}	[158]
$gs \rightarrow 1s_r$	-7.345×10^{-22}	3.842×10^{-20}	-5.515×10^{-19}	-2.677×10^{-18}	1.135×10^{-16}	-2.787×10^{-16}	1.260×10^{-16}	[158]
$gs \rightarrow 2p$	-1.041×10^{-21}	5.698×10^{-20}	-9.819×10^{-19}	2.390×10^{-18}	8.000×10^{-17}	-2.298×10^{-16}	1.126×10^{-16}	[151]
$1s_m \rightarrow 1s_r$	9.268×10^{-18}	-6.217×10^{-16}	1.637×10^{-14}	-2.141×10^{-13}	1.451×10^{-12}	-4.839×10^{-12}	6.733×10^{-12}	[160]
$1s_m \rightarrow 2p$	-2.634×10^{-19}	1.891×10^{-17}	-5.383×10^{-16}	7.727×10^{-15}	-6.107×10^{-14}	3.320×10^{-13}	-1.008×10^{-13}	[160]
$1s_r \rightarrow 2p$	-1.816×10^{-18}	1.266×10^{-16}	-3.503×10^{-15}	4.884×10^{-14}	-3.587×10^{-13}	1.301×10^{-12}	1.789×10^{-13}	[160]
$gs \rightarrow ion$[4]	-6.207×10^{-21}	4.196×10^{-19}	-1.069×10^{-17}	1.179×10^{-16}	-3.352×10^{-16}	2.636×10^{-16}	-2.385×10^{-17}	[154]
$1s \rightarrow ion$	8.383×10^{-20}	-5.591×10^{-18}	1.441×10^{-16}	-1.762×10^{-15}	9.393×10^{-15}	-1.789×10^{-15}	-2.626×10^{-15}	[168]
$2p \rightarrow ion$	1.57×10^{-19}	-9.773×10^{-18}	2.254×10^{-16}	-2.218×10^{-15}	5.157×10^{-15}	5.868×10^{-14}	-3.014×10^{-14}	[168]
$0 \rightarrow 0$[5]	1.255×10^{-19}	-8.225×10^{-18}	2.047×10^{-16}	-2.31×10^{-15}	9.416×10^{-15}	2.265×10^{-14}	-7.953×10^{-15}	[154]

[1] Transitions refer to electronic collisional reactions.
[2] Reverse transitions shall be derived using the *Detailed Balance Principle*.
[3] Reference refer to the set of cross-sections considered for the actual lumped transition.
[4] Ionization by electron collision.
[5] Elastic scattering of neutral particles.

Table A.6: Lumped rate coefficients fitting constants for the lowest density case in neon.

Transition [1][2]	p_6	p_5	p_4	p_3	p_2	p_1	p_0	Ref. [3]
$gs \rightarrow 1s_m$	-4.778×10^{-23}	2.725×10^{-21}	-5.159×10^{-20}	2.55×10^{-19}	2.148×10^{-18}	-7.363×10^{-18}	3.825×10^{-18}	[157]
$gs \rightarrow 1s_r$	-2.912×10^{-22}	1.958×10^{-20}	-4.937×10^{-19}	5.32×10^{-18}	-1.409×10^{-17}	9.289×10^{-18}	9.533×10^{-20}	[157]
$gs \rightarrow 2p$	-2.177×10^{-22}	1.395×10^{-20}	-3.282×10^{-19}	3.17×10^{-18}	-6.683×10^{-18}	2.265×10^{-19}	2.942×10^{-18}	[157]
$1s_m \rightarrow 1s_r$	-	-	-	-	-	-	-	-
$1s_m \rightarrow 2p$	1.141×10^{-20}	5.107×10^{-19}	-6.216×10^{-17}	1.803×10^{-15}	-2.367×10^{-14}	1.500×10^{-13}	-5.824×10^{-14}	[170]
$1s_r \rightarrow 2p$	2.029×10^{-19}	-1.064×10^{-17}	1.635×10^{-16}	3.213×10^{-16}	-3.217×10^{-14}	3.097×10^{-13}	-1.293×10^{-13}	[170]
$gs \rightarrow ion$[4]	-1.068×10^{-22}	1.109×10^{-20}	-4.296×10^{-19}	7.386×10^{-18}	-3.496×10^{-17}	5.561×10^{-17}	-2.115×10^{-17}	[165]
$1s \rightarrow ion$	5.721×10^{-20}	-3.886×10^{-18}	1.027×10^{-16}	-1.308×10^{-15}	7.525×10^{-15}	-5.076×10^{-15}	-1.139×10^{-16}	[168]
$2p \rightarrow ion$	1.55×10^{-19}	-9.868×10^{-18}	2.366×10^{-16}	-2.539×10^{-15}	9.265×10^{-15}	3.449×10^{-14}	-2.057×10^{-14}	[168]
$0 \rightarrow 0$[5]	3.175×10^{-21}	-2.326×10^{-19}	6.23×10^{-18}	-6.628×10^{-17}	-4.102×10^{-17}	8.1×10^{-15}	2.857×10^{-15}	[157]

[1] Transitions refer to electronic collisional reactions.

[2] Reverse transitions shall be derived using the *Detailed Balance Principle.*

[3] Reference refer to the set of cross-sections considered for the actual lumped transition.

[4] Ionization by electron collision.

[5] Elastic scattering of neutral particles.

Table A.7: Lumped rate coefficients fitting constants for the lowest density case in krypton.

Transition [1][2]	p_6	p_5	p_4	p_3	p_2	p_1	p_0	Ref. [3]
$gs \rightarrow 1s_m$	-8.269×10^{-22}	4.356×10^{-20}	$-6. \times 10^{-19}$	-3.501×10^{-18}	1.523×10^{-16}	-3.435×10^{-16}	1.465×10^{-16}	[155, 156]
$gs \rightarrow 1s_r$	-1.714×10^{-23}	-2.624×10^{-21}	2.038×10^{-19}	-4.925×10^{-18}	4.708×10^{-17}	-9.533×10^{-17}	3.981×10^{-17}	[155, 156]
$gs \rightarrow 2p$	-4.624×10^{-22}	8.278×10^{-21}	6.258×10^{-19}	-2.335×10^{-17}	2.686×10^{-16}	-5.703×10^{-16}	2.434×10^{-16}	[155, 156]
$1s_m \rightarrow 1s_r$	9.351×10^{-19}	-8.017×10^{-17}	2.737×10^{-15}	-4.757×10^{-14}	4.448×10^{-13}	-2.164×10^{-12}	4.700×10^{-12}	[160]
$1s_m \rightarrow 2p$	3.055×10^{-19}	-1.377×10^{-17}	1.018×10^{-16}	4.098×10^{-15}	-9.285×10^{-14}	7.405×10^{-13}	-3.020×10^{-13}	[160]
$1s_r \rightarrow 2p$	-1.042×10^{-18}	7.400×10^{-17}	-2.105×10^{-15}	3.074×10^{-14}	-2.462×10^{-13}	1.062×10^{-12}	-2.401×10^{-13}	[160]
$gs \rightarrow ion$[4]	-9.242×10^{-21}	6.128×10^{-19}	-1.517×10^{-17}	1.586×10^{-16}	-3.418×10^{-16}	6.276×10^{-17}	1.062×10^{-16}	[163]
$1s \rightarrow ion$	9.019×10^{-20}	-5.965×10^{-18}	1.519×10^{-16}	-1.824×10^{-15}	9.332×10^{-15}	1.234×10^{-15}	-4.211×10^{-15}	[168]
$2p \rightarrow ion$	1.473×10^{-19}	-8.987×10^{-18}	1.997×10^{-16}	-1.788×10^{-15}	1.272×10^{-15}	7.632×10^{-14}	-3.633×10^{-14}	[168]
$0 \rightarrow 0$[5]	1.452×10^{-19}	-8.848×10^{-18}	1.954×10^{-16}	-1.705×10^{-15}	6.815×10^{-16}	6.593×10^{-14}	-2.394×10^{-14}	[164]

[1] Transitions refer to electronic collisional reactions.

[2] Reverse transitions shall be derived using the *Detailed Balance Principle.*

[3] Reference refer to the set of cross-sections considered for the actual lumped transition.

[4] Ionization by electron collision.

[5] Elastic scattering of neutral particles.

Table A.8: Lumped rate coefficients fitting constants for the lowest density case in xenon.

Transition [1][2]	p_6	p_5	p_4	p_3	p_2	p_1	p_0	Ref. [3]
$gs \rightarrow 1s_m$	1.011×10^{-21}	-7.411×10^{-20}	2.142×10^{-18}	-3.016×10^{-17}	1.957×10^{-16}	-2.820×10^{-16}	8.728×10^{-17}	[156]
$gs \rightarrow 1s_r$	-2.919×10^{-22}	-3.913×10^{-23}	7.914×10^{-19}	-2.665×10^{-17}	3.359×10^{-16}	-6.299×10^{-16}	2.421×10^{-16}	[156]
$gs \rightarrow 2p$	3.020×10^{-22}	-4.962×10^{-20}	2.422×10^{-18}	-5.217×10^{-17}	4.964×10^{-16}	-9.126×10^{-16}	3.487×10^{-16}	[156]
$1s_m \rightarrow 1s_r$	-1.029×10^{-19}	6.702×10^{-18}	-1.717×10^{-16}	2.220×10^{-15}	-1.537×10^{-14}	4.340×10^{-14}	2.880×10^{-13}	[171]
$1s_m \rightarrow 2p$	1.173×10^{-19}	-5.245×10^{-18}	4.148×10^{-17}	1.269×10^{-15}	-2.624×10^{-14}	1.791×10^{-13}	-8.287×10^{-14}	[118]
$1s_r \rightarrow 2p$	-3.960×10^{-19}	3.060×10^{-17}	-9.637×10^{-16}	1.595×10^{-14}	-1.494×10^{-13}	7.833×10^{-13}	-2.225×10^{-13}	[118]
$gs \rightarrow ion$[4]	-1.201×10^{-20}	7.527×10^{-19}	-1.703×10^{-17}	1.461×10^{-16}	1.01×10^{-16}	-1.008×10^{-15}	5.883×10^{-16}	[165]
$1s \rightarrow ion$	9.971×10^{-20}	-6.56×10^{-18}	1.657×10^{-16}	-1.963×10^{-15}	9.733×10^{-15}	4.011×10^{-15}	-5.768×10^{-15}	[168]
$2p \rightarrow ion$	1.456×10^{-19}	-8.759×10^{-18}	1.894×10^{-16}	-1.564×10^{-15}	-1.27×10^{-15}	9.049×10^{-14}	-4.146×10^{-14}	[168]
$0 \rightarrow 0$[5]	-8.535×10^{-21}	2.448×10^{-18}	-1.339×10^{-16}	3.084×10^{-15}	-3.464×10^{-14}	1.795×10^{-13}	-4.371×10^{-14}	[164]

[1] Transitions refer to electronic collisional reactions.

[2] Reverse transitions shall be derived using the *Detailed Balance Principle.*

[3] Reference refer to the set of cross-sections considered for the actual lumped transition.

[4] Ionization by electron collision.

[5] Elastic scattering of neutral particles.

Appendix B

Air chemistry

Table B.1: Chemical reactions considered in the air-breathing model with their respective reaction rate. T_g and T_e are both in K while ε is the mean electron energy in eV [249]. Finally, $T_r = (T_e - T_g)/(T_e T_g)$. In Refs. a (Ref. [195]), b (Ref. [250]), c (Ref. [251])

#	Chemical reaction	Reaction rate [m^3/s] or [m^6/s]	Refs.
1	$e + N^+ + M \longrightarrow N + M$	$3.12 \times 10^{-35}/(T_e^{1.5})$	a
2	$e + e + N^+ \longrightarrow N + e$	$1 \times 10^{-31} \times (T_g/T_e)^{4.5}$	a
3	$e + N \longrightarrow N^+ + e + e$	$1.45 \times 10^{-17} \times \varepsilon^{2.58} \times \exp(-8.54/\varepsilon)$	a
4	$e + {N_2}^+ \longrightarrow N + N$	$2.8 \times 10^{-13} \times (300/T_e)^{0.5}$	a
5	$e + {N_2}^+ + M \longrightarrow N_2 + M$	$3.12 \times 10^{-35}/(T_e^{1.5})$	a
6	$e + e + {N_2}^+ \longrightarrow N_2 + e$	$1 \times 10^{-31} \times (T_g/T_e)^{4.5}$	a
7	$e + N_2 \longrightarrow {N_2}^+ + e + e$	EEDF-CALCULATION	c
8	$e + O^+ + M \longrightarrow O + M$	$3.12 \times 10^{-35}/(T_e^{1.5})$	a
9	$e + e + O^+ \longrightarrow O + e$	$1 \times 10^{-31} \times (T_g/T_e)^{4.5}$	a
10	$e + O \longrightarrow O^+ + e + e$	$4.75 \times 10^{-15} \times \varepsilon^{0.61} \times \exp(-22.1/\varepsilon)$	a
11	$e + O + O_2 \longrightarrow O^- + O_2$	1×10^{-43}	a
12	$e + O + O_2 \longrightarrow O + {O_2}^-$	1×10^{-43}	a
13	$e + {O_2}^+ \longrightarrow O + O$	$2 \times 10^{-13} \times (300/T_e)$	a
14	$e + e + {O_2}^+ \longrightarrow O_2 + e$	$1 \times 10^{-31} \times (T_g/T_e)^{4.5}$	a
15	$e + {O_2}^+ + M \longrightarrow O_2 + M$	$3.12 \times 10^{-35}/(T_e^{1.5})$	a
16	$e + O_2 \longrightarrow O + O^+ + e + e$	EEDF-CALCULATION	c
17	$e + O_2 \longrightarrow O + O + e$	$2.03 \times 10^{-14} \times \varepsilon^{-0.1} \times \exp(-8.47/\varepsilon)$	a
18	$e + O_2 \longrightarrow O^- + O$	EEDF-CALCULATION	c
19	$e + O_2 \longrightarrow {O_2}^+ + e + e$	EEDF-CALCULATION	c
20	$e + O_2 + O_2 \longrightarrow O_2 - + O_2$	$1.4 \times 10^{-41} \frac{T_g}{T_e} \exp(700 T_r - \frac{600}{T_g})$	a
21	$e + O_2 + N_2 \longrightarrow {O_2}^- + N_2$	$1.1 \times 10^{-43} (\frac{T_g}{T_e})^2 \exp(1500 T_r - \frac{70}{T_g})$	a
22	$e + NO^+ \longrightarrow N + O$	$1.07e - 11/(T_e^{0.85})$	a
23	$e + NO^+ + M \longrightarrow NO + M$	$3.12 \times 10^{-35}/(T_e^{1.5})$	a
24	$e + e + NO^+ \longrightarrow NO + e$	$1 \times 10^{-31} \times (T_g/T_e)^{4.5}$	a

Continued on next page

Table B.1 – continued from previous page

#	Chemical reaction	Reaction rate [m^3/s] or [m^6/s]	Refs.
25	$e + NO + M \longrightarrow NO^- + e$	8×10^{-43}	a
26	$e + NO_2{}^+ \longrightarrow NO + O$	$3.46 \times 10^{-12}/(T_e^{0.5})$	a
27	$e + NO_2 + M \longrightarrow NO_2{}^- + M$	1.5×10^{-42}	a
28	$e + NO_2 \longrightarrow O^- + NO$	1×10^{-17}	a
29	$e + N_2O^+ \longrightarrow N_2 + O$	$3.46 \times 10^{-12}/(T_e^{0.5})$	a
30	$e + N_2O \longrightarrow O^- + N_2$	2×10^{-16}	a
31	$N^+ + O \longrightarrow O^+ + N$	1×10^{-18}	a
32	$N^+ + O + M \longrightarrow NO^+ + M$	1×10^{-41}	a
33	$N^+ + O^- \longrightarrow O + N$	$2 \times 10^{-13} \times (300/T_g)^{0.5}$	a
34	$N^+ + N + M \longrightarrow N_2{}^+ + M$	1×10^{-41}	a
35	$N^+ + NO \longrightarrow NO^+ + N$	4.72×10^{-16}	a
36	$N^+ + NO \longrightarrow N_2{}^+ + O$	8.33×10^{-17}	a
37	$N^+ + NO \longrightarrow O^+ + N_2$	1×10^{-18}	a
38	$N^+ + NO^- \longrightarrow NO + N$	$2 \times 10^{-13} \times (300/T_g)^{0.5}$	a
39	$N^+ + O_2 \longrightarrow NO^+ + O$	2.7×10^{-16}	a
40	$N^+ + O_2 \longrightarrow O^+ + NO$	2.8×10^{-17}	a
41	$N^+ + O_2 \longrightarrow O_2{}^+ + N$	3×10^{-16}	a
42	$N^+ + O_2{}^- \longrightarrow O_2 + N$	$2 \times 10^{-13} \times (300/T_g)^{0.5}$	a
43	$N^+ + N_2O \longrightarrow NO^+ + N_2$	5.5×10^{-16}	a
44	$N^+ + N_2O^- \longrightarrow N_2O + N$	$2 \times 10^{-13} \times (300/T_g)^{0.5}$	a
45	$N^+ + NO_2 \longrightarrow NO_2{}^+ + N$	3×10^{-16}	a
46	$N^+ + NO_2 \longrightarrow NO^+ + NO$	5×10^{-16}	a
47	$N^+ + NO_2{}^- \longrightarrow NO_2 + N$	$2 \times 10^{-13} \times (300/T_g)^{0.5}$	a
48	$N + O^+ + M \longrightarrow NO^+ + M$	1×10^{-41}	a
49	$N + O + M \longrightarrow NO + M$	$6.3 \times 10^{-45} \times \exp(140/T_g)$	a
50	$N + O^- \longrightarrow NO + e$	2.6×10^{-16}	a
51	$N + N + M \longrightarrow N_2 + M$	$8.3 \times 10^{-46} \times \exp(500/T_g)$	a
52	$N + N_2{}^+ \longrightarrow N^+ + N_2$	1×10^{-18}	a
53	$N + NO^+ + M \longrightarrow N_2O^+ + M$	$1 \times 10^{-41} \times (300/T_g)$	a
54	$N + NO \longrightarrow N_2 + O$	$2.1 \times 10^{-17} \times \exp(100/T_g)$	a
55	$N + O_2{}^+ \longrightarrow NO^+ + O$	1.5×10^{-16}	a
56	$N + O_2 \longrightarrow NO + O$	$1.5 \times 10^{-17} \times \exp(-3600/T_g)$	a
57	$N + O_2{}^- \longrightarrow NO_2 + e$	5×10^{-16}	a
58	$N + NO_2 \longrightarrow N_2O + O$	$5.8 \times 10^{-18} \times \exp(220/T_g)$	a
59	$N + NO_2 \longrightarrow N_2 + O + O$	9.1×10^{-19}	a
60	$N + NO_2 \longrightarrow NO + NO$	6×10^{-19}	a
61	$N + NO_2 \longrightarrow N_2 + O_2$	7×10^{-19}	a
62	$N + NO_2{}^- \longrightarrow N_2 + O_2 + e$	1×10^{-18}	a
63	$O^+ + O + M \longrightarrow O_2{}^+ + M$	1×10^{-41}	a
64	$O^+ + O^- \longrightarrow O + O$	$2 \times 10^{-13} \times (300/T_g)^{0.5}$	a
65	$O^+ + NO \longrightarrow NO^+ + O$	1×10^{-18}	a
66	$O^+ + NO \longrightarrow O_2{}^+ + N$	3×10^{-18}	a

Continued on next page

Table B.1 – continued from previous page

#	Chemical reaction	Reaction rate [m^3/s] or [m^6/s]	Refs.
67	$O^+ + N_2 + M \longrightarrow NO^+ + N + M$	$6 \times 10^{-41} \times (300/T_g)^2$	a
68	$O^+ + NO^- \longrightarrow NO + O$	$2 \times 10^{-13} \times (300/T_g)^{0.5}$	a
69	$O^+ + O_2 \longrightarrow {O_2}^+ + O$	$2.1 \times 10^{-17} \times (300/T_g)^{0.5}$	a
70	$O^+ + {O_2}^- \longrightarrow O_2 + O$	$2 \times 10^{-13} \times (300/T_g)^{0.5}$	a
71	$O^+ + N_2O \longrightarrow N_2O^+ + O$	6.3×10^{-16}	a
72	$O^+ + N_2O \longrightarrow NO^+ + NO$	2.3×10^{-16}	a
73	$O^+ + N_2O \longrightarrow {O_2}^+ + N_2$	2×10^{-17}	a
74	$O^+ + N_2O^- \longrightarrow N_2O + O$	$2 \times 10^{-13} \times (300/T_g)^{0.5}$	a
75	$O^+ + NO_2 \longrightarrow NO^+ + O_2$	5×10^{-16}	a
76	$O^+ + NO_2 \longrightarrow {NO_2}^+ + O$	1.6×10^{-15}	a
77	$O^+ + {NO_2}^- \longrightarrow NO_2 + O$	$2 \times 10^{-13} \times (300/T_g)^{0.5}$	a
78	$O + O^- \longrightarrow O_2 + e$	1.4×10^{-16}	a
79	$O + {N_2}^+ \longrightarrow O^+ + N_2$	$1 \times 10^{-17} \times (300/T_g)^{0.5}$	a
80	$O + {N_2}^+ \longrightarrow NO^+ + N$	1.4×10^{-16}	a
81	$O + NO + M \longrightarrow NO_2 + M$	$1 \times 10^{-43} \times (300/T_g)^1.6$	a
82	$O + NO^- \longrightarrow O^- + NO$	3×10^{-16}	a
83	$O + {O_2}^- \longrightarrow O^- + O_2$	3.3×10^{-16}	a
84	$O + O + M \longrightarrow O_2 + M$	$3.2 \times 10^{-47} \times \exp(900/T_g)$	a
85	$O + NO_2 \longrightarrow NO + O_2$	$6.5 \times 10^{-18} \times \exp(120/T_g)$	a
86	$O^- + N_2 \longrightarrow N_2O + e$	1×10^{-18}	a
87	$O^- + NO \longrightarrow NO_2 + e$	2.6×10^{-16}	a
88	$O^- + NO + M \longrightarrow {NO_2}^- + M$	1×10^{-41}	a
89	$O^- + {N_2}^+ \longrightarrow O + N_2$	$2 \times 10^{-13} \times (300/T_g)^{0.5}$	a
90	$O^- + {N_2}^+ \longrightarrow O + N + N$	1×10^{-13}	a
91	$O^- + NO^+ \longrightarrow O + O + N$	1×10^{-13}	a
92	$O^- + NO^+ \longrightarrow O + NO$	$2 \times 10^{-13} \times (300/T_g)^{0.5}$	a
93	$O^- + {O_2}^+ \longrightarrow O + O + O$	1×10^{-13}	a
94	$O^- + {O_2}^+ \longrightarrow O + O_2$	$2 \times 10^{-13} \times (300/T_g)^{0.5}$	a
95	$O^- + N_2O^+ \longrightarrow O + N_2O$	$2 \times 10^{-13} \times (300/T_g)^{0.5}$	a
96	$O^- + N_2O^+ \longrightarrow O + O + N_2$	1×10^{-13}	a
97	$O^- + N_2O \longrightarrow NO^- + NO$	2×10^{-16}	a
98	$O^- + N_2O \longrightarrow N_2O^- + O$	2×10^{-18}	a
99	$O^- + {NO_2}^+ \longrightarrow O + NO_2$	$2 \times 10^{-13} \times (300/T_g)^{0.5}$	a
100	$O^- + {NO_2}^+ \longrightarrow O + N + O_2$	1×10^{-13}	a
101	$O^- + NO_2 \longrightarrow {NO_2}^- + O$	1.2×10^{-15}	a
102	${N_2}^+ + NO \longrightarrow NO^+ + N_2$	3.9×10^{-16}	a
103	${N_2}^+ + NO^- \longrightarrow NO + N_2$	$2 \times 10^{-13} \times (300/T_g)^{0.5}$	a
104	${N_2}^+ + NO^- \longrightarrow NO + N + N$	1×10^{-13}	a
105	${N_2}^+ + O_2 \longrightarrow {O_2}^+ + N_2$	5×10^{-17}	a
106	${N_2}^+ + {O_2}^- \longrightarrow O_2 + N_2$	$2 \times 10^{-13} \times (300/T_g)^{0.5}$	a
107	${N_2}^+ + {O_2}^- \longrightarrow O_2 + N + N$	1×10^{-13}	a
108	${N_2}^+ + N_2O \longrightarrow N_2O^+ + N_2$	6×10^{-16}	a

Continued on next page

Table B.1 – continued from previous page

#	Chemical reaction	Reaction rate [m^3/s] or [m^6/s]	Refs.
109	$N_2^+ + N_2O \longrightarrow NO^+ + N_2 + N$	4×10^{-16}	a
110	$N_2^+ + N_2O^- \longrightarrow N_2O + N_2$	$2 \times 10^{-13} \times (300/T_g)^{0.5}$	a
111	$N_2^+ + N_2O^- \longrightarrow N_2O + N + N$	1×10^{-13}	a
112	$N_2^+ + NO_2 \longrightarrow NO^+ + N_2O$	5×10^{-17}	a
113	$N_2^+ + NO_2 \longrightarrow NO_2^+ + N_2$	3×10^{-16}	a
114	$N_2^+ + NO_2^- \longrightarrow NO_2 + N_2$	$2 \times 10^{-13} \times (300/T_g)^{0.5}$	a
115	$N_2^+ + NO_2^- \longrightarrow NO_2 + N + N$	1×10^{-13}	a
116	$N_2 + O_2^+ \longrightarrow NO^+ + NO$	1×10^{-23}	a
117	$N_2 + O_2^- \longrightarrow N_2 + O_2 + e$	$1.9 \times 10^{-18} (T_g/300)^{0.5} \exp(-4990/T_g)$	a
118	$NO^+ + NO^- \longrightarrow NO + NO$	$2 \times 10^{-13} \times (300/T_g)^{0.5}$	a
119	$NO^+ + NO^- \longrightarrow NO + N + O$	1×10^{-13}	a
120	$NO^+ + O_2^- \longrightarrow O_2 + N + O$	1×10^{-13}	a
121	$NO^+ + O_2^- \longrightarrow O_2 + NO$	$2 \times 10^{-13} \times (300/T_g)^{0.5}$	a
122	$NO^+ + N_2O^- \longrightarrow N_2O + NO$	$2 \times 10^{-13} \times (300/T_g)^{0.5}$	a
123	$NO^+ + N_2O^- \longrightarrow N_2O + N + O$	1×10^{-13}	a
124	$NO^+ + NO_2^- \longrightarrow NO_2 + NO$	$2 \times 10^{-13} \times (300/T_g)^{0.5}$	a
125	$NO^+ + NO_2^- \longrightarrow NO_2 + N + O$	1×10^{-13}	a
126	$NO + NO^- \longrightarrow NO + NO + e$	5×10^{-18}	a
127	$NO + O_2^+ \longrightarrow NO^+ + O_2$	4.6×10^{-16}	a
128	$NO + N_2O^+ \longrightarrow NO^+ + N_2O$	2.3×10^{-16}	a
129	$NO + NO_2^+ \longrightarrow NO^+ + NO_2$	2.75×10^{-16}	a
130	$NO + NO_2^- \longrightarrow NO^- + NO_2$	2.75×10^{-16}	a
131	$NO^- + M \longrightarrow NO + M + e$	2.4×10^{-19}	a
132	$NO^- + O_2^+ \longrightarrow NO + O_2$	$2 \times 10^{-13} \times (300/T_g)^{0.5}$	a
133	$NO^- + O_2^+ \longrightarrow NO + O + O$	1×10^{-13}	a
134	$NO^- + O_2 \longrightarrow O_2^- + NO$	5×10^{-16}	a
135	$NO^- + NO_2^+ \longrightarrow NO + NO_2$	$2 \times 10^{-13} \times (300/T_g)^{0.5}$	a
136	$NO_2^+ + NO^- \longrightarrow NO + N + O_2$	1×10^{-13}	a
137	$NO^- + N_2O^+ \longrightarrow NO + N_2O$	$2 \times 10^{-13} \times (300/T_g)^{0.5}$	a
138	$NO^- + N_2O^+ \longrightarrow NO + N_2 + O$	1×10^{-13}	a
139	$NO^- + N_2O \longrightarrow NO + N_2O + e$	5.1×10^{-18}	a
140	$NO^- + N_2O \longrightarrow NO_2^- + N_2$	2.8×10^{-20}	a
141	$NO^- + NO_2 \longrightarrow NO_2^- + NO$	3×10^{-16}	a
142	$O_2^+ + O_2^- \longrightarrow O_2 + O_2$	$2 \times 10^{-13} \times (300/T_g)^{0.5}$	a
143	$O_2^+ + O_2^- \longrightarrow O_2 + O + O$	1×10^{-13}	a
144	$O_2^+ + N_2O^- \longrightarrow N_2O + O_2$	$2 \times 10^{-13} \times (300/T_g)^{0.5}$	a
145	$O_2^+ + N_2O^- \longrightarrow N_2O + O + O$	1×10^{-13}	a
146	$O_2^+ + NO_2 \longrightarrow NO_2^+ + O_2$	6.6×10^{-16}	a
147	$O_2^+ + NO_2^- \longrightarrow NO_2 + O_2$	$2 \times 10^{-13} \times (300/T_g)^{0.5}$	a
148	$O_2^+ + NO_2^- \longrightarrow NO_2 + O + O$	1×10^{-13}	a
149	$O_2 + O_2^- \longrightarrow O_2 + O_2 + e$	$2.7 \times 10^{-16} (T_g/300)^{0.5} \exp(-5590/T_g)$	a
150	$O_2 + N_2O^+ \longrightarrow NO^+ + NO_2$	4.59×10^{-17}	a

Continued on next page

Table B.1 – continued from previous page

#	Chemical reaction	Reaction rate [m^3/s] or [m^6/s]	Refs.
151	$O_2 + N_2O^+ \longrightarrow O_2^+ + N_2O$	2.24×10^{-16}	a
152	$O_2^- + N_2O^+ \longrightarrow O_2 + N_2O$	$2 \times 10^{-13} \times (300/T_g)^{0.5}$	a
153	$O_2^- + N_2O^+ \longrightarrow O_2 + N_2 + O$	1×10^{-13}	a
154	$O_2^- + NO_2^+ \longrightarrow O_2 + NO_2$	$2 \times 10^{-13} \times (300/T_g)^{0.5}$	a
155	$O_2^- + NO_2^+ \longrightarrow O_2 + N + O_2$	1×10^{-13}	a
156	$O_2^- + NO_2 \longrightarrow NO_2^- + O_2$	7×10^{-16}	a
157	$N_2O^+ + N_2O \longrightarrow NO^+ + NO + N_2$	1.2×10^{-17}	a
158	$N_2O^+ + N_2O^- \longrightarrow N_2O + N_2O$	$2 \times 10^{-13} \times (300/T_g)^{0.5}$	a
159	$N_2O^+ + N_2O^- \longrightarrow N_2O + N_2 + O$	1×10^{-13}	a
160	$N_2O^+ + NO_2 \longrightarrow NO^+ + N_2 + O_2$	4.29×10^{-16}	a
161	$N_2O^+ + NO_2 \longrightarrow NO_2^+ + N_2O$	2.21×10^{-16}	a
162	$N_2O^+ + NO_2^- \longrightarrow NO_2 + N_2O$	$2 \times 10^{-13} \times (300/T_g)^{0.5}$	a
163	$N_2O^+ + NO_2^- \longrightarrow NO_2 + N_2 + O$	1×10^{-13}	a
164	$N_2O^- + NO_2^+ \longrightarrow N_2O + NO_2$	$2 \times 10^{-13} \times (300/T_g)^{0.5}$	a
165	$N_2O^- + NO_2^+ \longrightarrow N_2O + N + O_2$	1×10^{-13}	a
166	$NO_2^+ + NO_2^- \longrightarrow NO_2 + NO_2$	$2 \times 10^{-13} \times (300/T_g)^{0.5}$	a
167	$NO_2^+ + NO_2^- \longrightarrow NO_2 + N + O_2$	1×10^{-13}	a
168	$e + N_2 \longrightarrow e + N + N$	DATA-FROM-PLOT	b
169	$e + N_2 \longrightarrow e + N_2^*$	DATA-FROM-PLOT	b
170	$e + N_2 \longrightarrow e + N_2$	DATA-FROM-PLOT	b
171	$e + N_2^+ \longrightarrow e + N_2^+$	DATA-FROM-PLOT	b
172	$e + N \longrightarrow e + N^*$	DATA-FROM-PLOT	b
173	$e + N \longrightarrow e + N$	DATA-FROM-PLOT	b
174	$e + N^+ \longrightarrow e + N^+$	DATA-FROM-PLOT	b
175	$e + O \longrightarrow e + O^*$	DATA-FROM-PLOT	b
176	$e + O \longrightarrow e + O$	DATA-FROM-PLOT	b
177	$e + O^+ \longrightarrow e + O^+$	DATA-FROM-PLOT	b
178	$e + O_2 \longrightarrow e + O_2$	EEDF-CALCULATION	c

Bibliography

[1] Ronald W Humble, Gary N Henry, Wiley J Larson, and *et al.* *Space propulsion analysis and design*. McGraw-Hill, New York NY, USA, 1995.

[2] Robert G Jahn. *Physics of electric propulsion*. Courier Corporation, 2006.

[3] Wiley J Larson and James R Wertz. *Space Mission Analysis and Design*. Microcosm, Inc., El Segundo CA, USA, 3 edition, 1999.

[4] M Martinez-Sanchez and James E Pollard. Spacecraft electric propulsion-an overview. *Journal of propulsion and power*, 14(5):688–699, 1998.

[5] Robert G Jahn and Edgar Y Choueiri. Electric propulsion. `http://alfven.princeton.edu/publications/ep-encyclopedia-2001`. Accessed: 2018-09-19.

[6] List of spacecraft with electric propulsion. `https://en.wikipedia.org/wiki/List_of_spacecraft_with_electric_propulsion`. Accessed: 2018-09-19.

[7] Dan M Goebel and Ira Katz. *Fundamentals of electric propulsion: Ion and Hall thrusters*. JPL Space Science & Technology Series, 2008.

[8] Kazunori Takahashi. Helicon-type radiofrequency plasma thrusters and magnetic plasma nozzles. *Reviews of Modern Plasma Physics*, 3(1):1–61, 2019.

[9] Technology for propulsion and innovation official web site. `http://www.t4innovation.com/`. Accessed: 2018-09-19.

[10] Francis F Chen. Helicon discharges and sources: a review. *Plasma Sources Science and Technology*, 24(1):014001, 2015.

[11] M. Manente, F. Trezzolani, M. Magarotto, E. Fantino, A. Selmo, N. Bellomo, E. Toson, and D. Pavarin. Regulus: A propulsion platform to boost small satellite missions. *Acta Astronautica*, 157:241–249, 4 2019.

[12] Nicolas Bellomo, Mirko Magarotto, Marco Manente, Fabio Trezzolani, Riccardo Mantellato, Lorenzo Cappellini, Devis Paulon, Antonio Selmo, Davide Scalzi, Marco Minute, et al. Design and in-orbit demonstration of regulus, an iodine electric propulsion system. *CEAS Space Journal*, 2021.

[13] Mirko Magarotto, Marco Manente, Fabio Trezzolani, and Daniele Pavarin. Numerical model of a helicon plasma thruster. *IEEE Transactions on Plasma Science*, 48:835–844, 4 2020.

[14] Mirko Magarotto and Daniele Pavarin. Parametric study of a cathode-less radio frequency thruster. *IEEE Transactions on Plasma Science*, 48:2723–2735, 8 2020.

[15] Eduardo Ahedo and Mario Merino. Two-dimensional supersonic plasma acceleration in a magnetic nozzle. *Physics of Plasmas*, 17(7):073501, 2010.

[16] Jiewei Zhou, Gonzalo Sánchez-Arriaga, and E Ahedo. Time-dependent expansion of a weakly-collisional plasma beam in a paraxial magnetic nozzle. *Plasma Sources Science and Technology*, 30(4):045009, 2021.

[17] Dan M. Goebel and Ira Katz. *Fundamentals of Electric Propulsion: Ion and Hall Thrusters*. John Wiley & Sons, Inc., 10 2008.

[18] Francesco Romano, Y-A Chan, Georg Herdrich, C Traub, S Fasoulas, PCE Roberts, K Smith, S Edmondson, S Haigh, NH Crisp, et al. Rf helicon-based inductive plasma thruster (ipt) design for an atmosphere-breathing electric propulsion system (abep). *Acta Astronautica*, 176:476–483, 2020.

[19] Alfio E Vinci and Stéphane Mazouffre. Direct experimental comparison of krypton and xenon discharge properties in the magnetic nozzle of a helicon plasma source. *Physics of Plasmas*, 28(3):033504, 2021.

[20] Michael D West, Christine Charles, and Rod W Boswell. Testing a helicon double layer thruster immersed in a space-simulation chamber. *Journal of Propulsion and Power*, 24(1):134–141, 2008.

[21] D. Pavarin, F. Ferri, M. Manente, D. Rondini, D. Curreli, Y. Guclu, M. Melazzi, S. Suman, and G. Bianchini. Helicon plasma hydrazine combined micro project overview and development status. In *Proceedings of the 2nd Space Propulsion Conference SP2010-1842379*, San Sebastian, E, 2010.

[22] F. Trezzolani, M. Manente, A. Selmo, D. Melazzi, M. Magarotto, D. Moretto, P. De Carlo, M. Pessana, and D. Pavarin. Development and test of an high power rf plasma thruster in project sapere-strong. In *The 35th International Electric Propulsion Conference IEPC-2017-462*, Atlanta, GA, USA, 2017.

[23] Technology for propulsion and innovation. `https://www.t4innovation.com`, Accessed on 1 January 2022.

[24] Franklin R. Chang Díaz. The vasimr rocket. *Scientific American*, 283:90–97, 11 2000.

[25] Mercedes Ruiz, V Gomez, P Fajardo, J Navarro, R Albertoni, G Dickeli, A Vinci, Stéphane Mazouffre, and N Hildebrand. Hipatia: A project for the development of the helicon plasma thruster and its associated technologies to intermediate-high trls. In *71st International Astronautical Congress (IAC)*, Washington, DC, USA, 2020.

[26] Kazunori Takahashi. Magnetic nozzle radiofrequency plasma thruster approaching twenty percent thruster efficiency. *Scientific reports*, 11(1):1–12, 2021.

[27] Oleg V Batishchev. Minihelicon plasma thruster. *IEEE Transactions on plasma science*, 37(8):1563–1571, 2009.

[28] JP Sheehan, Timothy A Collard, Frans H Ebersohn, and Benjamin W Longmier. Initial operation of the cubesat ambipolar thruster. In *34th International Electric Propulsion Conference, IEPC-2015-243*, Hyogo-Kobe,J, 2015.

[29] R Winglee, T Ziemba, L Giersch, J Prager, J Carscadden, and BR Roberson. Simulation and laboratory validation of magnetic nozzle effects for the high power helicon thruster. *Physics of Plasmas*, 14(6):063501, 2007.

[30] Michael A Lieberman and Alan J Lichtenberg. *Principles of plasma discharges and materials processing.* John Wiley & Sons, Inc., Hoboken NJ, USA, 2005.

[31] D Melazzi, D Curreli, M Manente, J Carlsson, and D Pavarin. SPIREs: A Finite-Difference Frequency-Domain electromagnetic solver for inhomogeneous magnetized plasma cylinders. *Computer Physics Communications*, 183(6):1182–1191, 2012.

[32] J A Lehane and P C Thonemann. An experimental study of helicon wave propagation in a gaseous plasma. *Proceedings of the Physical Society*, 85(2):301–316, 1965.

[33] Roderick William Boswell. Very efficient plasma generation by whistler waves near the lower hybrid frequency. *Plasma Physics and Controlled Fusion*, 26(10):1147–1162, 1984.

[34] Francis F Chen and Rod W Boswell. Helicons-the past decade. *IEEE Transactions on Plasma Science*, 25(6):1245–1257, 1997.

[35] I Tepermeister, N Blayo, FP Klemens, DE Ibbotson, RA Gottscho, JTC Lee, and HH Sawin. Comparison of advanced plasma sources for etching applications. I. Etching rate, uniformity, and profile control in a helicon and a multiple electron cyclotron resonance source. *Journal of Vacuum Science & Technology B: Microelectronics and Nanometer Structures Processing, Measurement, and Phenomena*, 12(4):2310–2321, 1994.

[36] R. H. Goulding, J. B. O. Caughman, J. Rapp, T. M. Biewer, T. S. Bigelow, I. H. Campbell, J. F. Caneses, D. Donovan, N. Kafle, E. H. Martin, H. B. Ray, G. C. Shaw, and M. A. Showers. Progress in the development of a high power helicon plasma source for the materials plasma exposure experiment. *Fusion Science and Technology*, 72(4):588–594, 2017.

[37] A. J. Perry, D. Vender, and R. W. Boswell. The application of the helicon source to plasma processing. *Journal of Vacuum Science and Technology B, Nanotechnology and Microelectronics: Materials, Processing, Measurement, and Phenomena*, 9(2):310–317, 1991.

[38] Francis F Chen and Donald Arnush. Generalized theory of helicon waves. i. normal modes. *Physics of Plasmas*, 4(9):3411–3421, 1997.

[39] Francis F Chen. *Introduction to plasma physics and controlled fusion*, volume 1: Plasma Physics. Plenum Press, New York NY, USA, 2 edition, 1984.

[40] M. D. Carter, F. W. Baity Jr., G. C. Barber, R. H. Goulding, Y. Mori, D. O. Sparks, K. F. White, E. F. Jaeger, F. R. Chang-Diaz, and J. P. Squire. Comparing experiments with modeling for light ion helicon plasma sources. *Physics of Plasmas*, 9(12):5097–5110, December 2002.

[41] A Cardinali, D Melazzi, M Manente, and D Pavarin. Ray-tracing wkb analysis of whistler waves in non-uniform magnetic fields applied to space thrusters. *Plasma Sources Science and Technology*, 23(1):015013, 2014.

[42] Filippo Cichocki, Adrián Domínguez-Vázquez, Mario Merino, and Eduardo Ahedo. Hybrid 3D model for the interaction of plasma thruster plumes with nearby objects. *Plasma Sources Science and Technology*, 26(12):125008, 2017.

[43] Mario Merino, Filippo Cichocki, and Eduardo Ahedo. A collisionless plasma thruster plume expansion model. *Plasma Sources Science and Technology*, 24(3):035006, 2015.

[44] Trevor Lafleur. Helicon plasma thruster discharge model. *Physics of Plasmas*, 21(4):043507, 2014.

[45] Eduardo Ahedo and Jaume Navarro-Cavallé. Helicon thruster plasma modeling: Two-dimensional fluid-dynamics and propulsive performances. *Physics of Plasmas*, 20(4):043512, 2013.

[46] A Fruchtman, K Takahashi, C Charles, and RW Boswell. A magnetic nozzle calculation of the force on a plasma. *Physics of Plasmas*, 19(3):033507, 2012.

[47] Arnab Rai Choudhuri. *The Physics of Fluids and Plasmas*. Cambridge University Press, 1998.

[48] J van Dijk, G M W Kroesen, and A. Bogaerts. Plasma modelling and numerical simulation. *Journal of Physics D: Applied Physics*, 42:190301, 10 2009.

[49] Filippo Cichocki, Adrián Domínguez-Vázquez, Mario Merino, and Eduardo Ahedo. Hybrid 3d model for the interaction of plasma thruster plumes with nearby objects. *Plasma Sources Science and Technology*, 26:125008, 11 2017.

[50] M. Martinez-Sanchez, J. Navarro-Cavallé, and E. Ahedo. Electron cooling and finite potential drop in a magnetized plasma expansion. *Physics of Plasmas*, 22:053501, 5 2015.

[51] Yoshinori Takao and Kazunori Takahashi. Numerical validation of axial plasma momentum lost to a lateral wall induced by neutral depletion. *Physics of Plasmas*, 22(11):113509, 2015.

[52] Guangye Chen. A self-consistent model of helicon discharge, phd thesis, 2008.

[53] Álvaro Sánchez-Villar, Jiewei Zhou, Eduardo Ahedo, and Mario Merino. Coupled plasma transport and electromagnetic wave simulation of an ecr thruster. *Plasma Sources Science and Technology*, 30(4):045005, 2021.

[54] Jiewei Zhou, Daniel Pérez-Grande, Pablo Fajardo, and Eduardo Ahedo. Numerical treatment of a magnetized electron fluid model within an electromagnetic plasma thruster simulation code. *Plasma Sources Science and Technology*, 28(11):115004, 2019.

[55] Y. Mouzouris and J. E. Scharer. Modeling of profile effects for inductive helicon plasma sources. *IEEE Transactions on Plasma Science*, 24(1):152–160, February 1996.

[56] D. Melazzi, D. Curreli, M. Manente, J. Carlsson, and D. Pavarin. SPIREs: A finite-difference frequency-domain electromagnetic solver for inhomogeneous magnetized plasma cylinders. *Computer Physics Communication*, 183(6):1182–1191, 2012.

[57] Davide Melazzi and Vito Lancellotti. Adamant: A surface and volume integral-equation solver for the analysis and design of helicon plasma sources. *Computer Physics Communications*, 185(7):1914–1925, 2014.

[58] Donald Arnush. The role of Trivelpiece - Gould waves in antenna coupling to helicon waves. *Physics of Plasmas*, 7(7):3042–3050, July 2000.

[59] A Cardinali and F Santini. Lower hybrid penetration across a steep density gradient. *Plasma Physics and Controlled Fusion*, 53(12):125001, 2011.

[60] Suwon Cho and MA Lieberman. Self-consistent discharge characteristics of collisional helicon plasmas. *Physics of Plasmas*, 10(3):882–890, 2003.

[61] Ronald L Kinder and Mark J Kushner. Wave propagation and power deposition in magnetically enhanced inductively coupled and helicon plasma sources. *Journal of Vacuum Science & Technology A: Vacuum, Surfaces, and Films*, 19(1):76–86, 2001.

[62] Ronald L Kinder and Mark J Kushner. Noncollisional heating and electron energy distributions in magnetically enhanced inductively coupled and helicon plasma sources. *Journal of Applied Physics*, 90(8):3699–3712, 2001.

[63] Deepak Bose, TR Govindan, and M Meyyappan. Modeling of a helicon plasma source. *IEEE transactions on plasma science*, 31(4):464–470, 2003.

[64] Guangye Chen. *A self-consistent model of helicon discharge.* PhD thesis, The University of Texas at Austin, 2008.

[65] M Martinez-Sanchez, J Navarro-Cavallé, and E Ahedo. Electron cooling and finite potential drop in a magnetized plasma expansion. *Physics of Plasmas*, 22(5):053501, 2015.

[66] Marco Manente, Johan Carlsson, Ivano Musso, Cristina Bramanti, Daniele Pavarin, and Francesco Angrilli. Numerical simulation of the helicon double layer thruster concept. In *43^{rd} AIAA/ASME/SAE/ASEE Joint Propulsion Conference & Exhibit*, number AIAA 2007-5312, Cincinnati, OH, 2007.

[67] Johan Carlsson, Marco Manente, and Daniele Pavarin. Implicitly charge-conserving solver for Boltzmann electrons. *Physics of Plasmas*, 16(6):062310, 2009.

[68] Mario Merino and Eduardo Ahedo. Two-dimensional quasi-double-layers in two-electron-temperature, current-free plasmas. *Physics of Plasmas*, 20(2):023502, 2013.

[69] Nagendra Singh. Current-free double layers: A review. *Physics of plasmas*, 18(12):122105, 2011.

[70] M. Magarotto, D. Melazzi, and D. Pavarin. 3d-virtus: Equilibrium condition solver of radio-frequency magnetized plasma discharges for space applications. *Computer Physics Communications*, 247:106953, 2 2020.

[71] D. Melazzi and V. Lancellotti. Adamant: A surface and volume integral-equation solver for the analysis and design of helicon plasma sources. *Computer Physics Communications*, 185:1914–1925, 7 2014.

[72] Openfoam.

[73] D. Pavarin E. Ahedo K. Katsonis F. Scortecci M. Pessana G. Parissenti, N. Koch. Non conventional propellants for electric propulsion applications. In *Proceedings of the 2^{nd} Space Propulsion Conference*, number SP2010-1841086, San Sebastian, ES, 2010.

[74] K. Holste et al. In search of alternative propellants for ion thrusters. In *Proceedings of the 34th International Electric Propulsion Conference*, number IEPC-2015-320, Hyogo-Kobe, Japan, 2015.

[75] V. Giannetti et al. Electric propulsion system trade-off analysis based on alternative propellant selection. In *Proceedings of the 5th Space Propulsion Conference*, number SP2016-3125194, Rome, Italy, 2016.

[76] Anna J Sheppard and Justin M Little. Scaling laws for electrodeless plasma propulsion with water vapor propellant. *Plasma Sources Science and Technology*, 29(4):045007, March 2020.

[77] F. Romano et al. Performance evaluation of a novel inductive atmosphere-breathing ep system. In *Proceedings of the 35th International Electric Propulsion Conference*, number IEPC-2017-184, Atlanta, USA, 2017.

[78] N. Souhair et al. K. Papavramidis, J. Skalden. Development activities for the rf helicon-based plasma thruster: Thrust measurement and b-dot probe set-up. In *Proceedings of the 37th International Electric Propulsion Conference*, number IEPC-2022-432, Boston, USA, 2022.

[79] T. Andreussi, E. Ferrato, C. A. Paissoni, A. Kitaeva, V. Giannetti, A. Piragino, S. Schäff, K. Katsonis, Ch. Berenguer, Z. Kovacova, E. Neubauer, M. Tisaev, B. Karadag, A. Lucca Fabris, M. Smirnova, A. Mingo, D. Le Quang, Z. Alsalihi, F. Bariselli, P. Parodi, P. Jorge, and T. E. Magin. The AETHER project: development of air-breathing electric propulsion for VLEO missions. *CEAS Space Journal*, 14(4):717–740, April 2022.

[80] F Cannat, T Lafleur, J Jarrige, P Chabert, P-Q Elias, and D Packan. Optimization of a coaxial electron cyclotron resonance plasma thruster with an analytical model. *Physics of Plasmas*, 22(5):053503, 2015.

[81] C Charles, R W Boswell, R Laine, and P MacLellan. An experimental investigation of alternative propellants for the helicon double layer thruster. *Journal of Physics D: Applied Physics*, 41(17):175213, August 2008.

[82] J. Szabo, M. Robin, and S. Paintal. Iodine propellant space propulsion, 2013.

[83] Nicolas Bellomo, Marco Manente, Fabio Trezzolani, Alessia Gloder, Antonio Selmo, Riccardo Mantellato, Elena Toson, Lorenzo Cappellini, Matteo Duzzi, Davide Scalzi, Alessandro Schiavon, Alessandro Barbato, Devis Paulon, Nabil Souhair, Mirko Magarotto, Marco Minute, Riccardo Di Roberto, Daniele Pavarin, and Filippo Graziani. Enhancement of microsatellites' mission capabilities: integration of regulus electric propulsion module into unisat-7. In *Proceedings of the 70th International Astronautical Congress (IAC)*, 2019.

[84] D. Rafalskyi et al. In-orbit demonstration of an iodine electric propulsion system, 2021.

[85] T. Lafleur. Helicon plasma thruster discharge model, 2014.

[86] Lubos Brieda and Michael Keidar. Development of the starfish plasma simulation code and update on multiscale modeling of hall thrusters. In *48th AIAA/ASME/SAE/ASEE Joint Propulsion Conference & Exhibit*, number AIAA 2012-4015, Atlanta, GA, USA, 2012.

[87] Shaun Andrews, Simone Di Fede, and Mirko Magarotto. Fully kinetic model of plasma expansion in a magnetic nozzle. *Plasma Sources Science and Technology*, 31(3):035022, March 2022.

[88] J. A. Bittencourt. *Fundamentals of Plasma Physics.* Springer New York, 2004.

[89] D. M. Goebel and I. Katz. Fundamentals of electric propulsion: Ion and hall thrusters, 2008.

[90] Trevor Lafleur. Helicon plasma thruster discharge model. *Physics of Plasmas*, 21(4):043507, 2014.

[91] Pascal Chabert, J Arancibia Monreal, Jérôme Bredin, Lara Popelier, and Ane Aanesland. Global model of a gridded-ion thruster powered by a radiofrequency inductive coil. *Physics of Plasmas*, 19(7):073512, 2012.

[92] Michael A Lieberman and Alan J Lichtenberg. *Principles of plasma discharges and materials processing.* John Wiley & Sons, 2005.

[93] Matteo Guaita, Mirko Magarotto, Marco Manente, Daniele Pavarin, and Michéle Lavagna. Semi-analytical model of a Helicon plasma thruster. *IEEE Transactions on Plasma Science*, 50(2):425–438, 2022.

[94] Shaun Andrews, Simone Di Fede, and Mirko Magarotto. Fully kinetic model of plasma expansion in a magnetic nozzle. *Plasma Sources Science and Technology*, 31:035022, 2022.

[95] C. Lee and M.A. Lieberman. Global model of ar, o2, cl2, and ar/o2 high density plasma discharges, 1995.

[96] V. A. Godyak. Soviet radio frequency discharge research, 1986.

[97] Michael A. Lieberman and Allan J. Lichtenberg. Principles of plasma discharges and materials processing, 2005.

[98] P. Chabert. An expression for the hl factor in low-pressure electronegative plasma discharges, 2016.

[99] K. Mròzek et al. Global plasma modeling of a magnetized high-frequency plasma source in low-pressure nitrogen and oxygen for air-breathing electric propulsion applications, 2021.

[100] D. Levko and C. Shukla et al. Plasma kinetics of c-c4f8 inductively coupled plasma revisited, 2022.

[101] R. S. Brokaw. Predicting transport properties of dilute gases, 1969.

[102] P. D. Neufeld, A. R. Janzen, and R. A. Aziz. Empirical equations to calculate 16 of the transport collision integrals g(i,8)* for the lennard-jones (12-6) potentials, 1972.

[103] R.A. Svehla. Transport coefficients for the nasa lewis chemical equilibrium program, 1995.

[104] L. D. Smoot and D. T. Pratt. Pulverized-coal combustion and gasification, 1979.

[105] Michael A. Lieberman and Alan J. Lichtenberg. *Principles of Plasma Discharges and Materials Processing.* Wiley, ii edition, 2005.

[106] Z Navrátil, D Trunec, V Hrachová, and A Kanka. Collisional–radiative model of neon discharge: determination of E / N in the positive column of low pressure discharge. *Journal of Physics D: Applied Physics*, 40(4):1037–1046, feb 2007.

[107] Philip G Hill and Carl R Peterson. *Mechanics And Thermodynamics of Propulsion.* Pearson, 1992.

[108] Benjamin D. Prince, Raymond J. Bemish, and Yu-Hui Chiu. Emission-Excitation Cross Sections Relevant to Krypton-Propelled Electric Thrusters. *Journal of Propulsion and Power*, 31(2):725–736, mar 2015.

[109] L Srivastava Gangwar, R K Sharma. Argon plasma modeling with detailed fine-structure cross sections. *Journal of Applied Physics*, 2012.

[110] Annemie Bogaerts, Renaat Gijbels, and Jaroslav Vlcek. Collisional-radiative model for an argon glow discharge. *Journal of Applied Physics*, 84(1):121–136, jul 1998.

[111] J Vlcek. A collisional-radiative model applicable to argon discharges over a wide range of conditions. I. Formulation and basic data. *Journal of Physics D: Applied Physics*, 22(5):623–631, may 1989.

[112] K. Katsonis and H.W. Drawin. Transition probabilities for argon(I). *Journal of Quantitative Spectroscopy and Radiative Transfer*, 23(1):1–55, jan 1980.

[113] J Vlcek and V Pelikan. A collisional-radiative model applicable to argon discharges over a wide range of conditions. II. Application to low-pressure, hollow-cathode arc and low-pressure glow discharges. *Journal of Physics D: Applied Physics*, 22(5):632–643, may 1989.

[114] J Vicek and V Pelikan. A collisional-radiative model applicable to argon discharges over a wide range of conditions. III. Application to atmospheric and subatmospheric pressure arcs. *Journal of Physics D: Applied Physics*, 23(5):526–532, may 1990.

[115] Xi-Ming Zhu and Yi-Kang Pu. A simple collisional–radiative model for low-temperature argon discharges with pressure ranging from 1 pa to atmospheric pressure: kinetics of paschen 1s and 2p levels. *Journal of Physics D: Applied Physics*, 43(1):015204, dec 2009.

[116] S S Baghel, S Gupta, R K Gangwar, and R Srivastava. Diagnostics of low-temperature neon plasma through a fine-structure resolved collisional–radiative model. *Plasma Sources Science and Technology*, 28(11):115010, nov 2019.

[117] Reetesh K Gangwar, Dipti, Rajesh Srivastava, and Luc Stafford. Spectroscopic diagnostics of low-pressure inductively coupled Kr plasma using a collisional–radiative model with fully relativistic cross sections. *Plasma Sources Science and Technology*, 25(3):035025, jun 2016.

[118] Priti, R K Gangwar, and R Srivastava. Collisional-radiative model of xenon plasma with calculated electron-impact fine-structure excitation cross-sections. *Plasma Sources Science and Technology*, 28(2):025003, feb 2019.

[119] Xi-Ming Zhu, Yan-Fei Wang, Yang Wang, Da-Ren Yu, Oleg Zatsarinny, Klaus Bartschat, Tsanko Vaskov Tsankov, and Uwe Czarnetzki. A xenon collisional-radiative model applicable to electric propulsion devices: II. Kinetics of the 6 s , 6 p , and 5 d states of atoms and ions in Hall thrusters. *Plasma Sources Science and Technology*, 28(10):105005, oct 2019.

[120] B. Der Van Sijde, J. J. A. M. van der Mullen, and D. C. Schram. Collisional Radiative Models in Plasmas. *Beiträge aus der Plasmaphysik*, 24(5):447–473, 1984.

[121] H. C. Kim, F. Iza, S. S. Yang, M. Radmilović-Radjenović, and J. K. Lee. Particle and fluid simulations of low-temperature plasma discharges: benchmarks and kinetic effects. *Journal of Physics D: Applied Physics*, 38:R283–R301, 10 2005.

[122] G. J. M. Hagelaar, J. Bareilles, L. Garrigues, and J. P. Boeuf. Two-dimensional model of a stationary plasma thruster. *Journal of Applied Physics*, 91(9):5592–5598, may 2002.

[123] Ioannis G. Mikellides, Ira Katz, Dan M. Goebel, and James E. Polk. Hollow cathode theory and experiment. II. A two-dimensional theoretical model of the emitter region. *Journal of Applied Physics*, 98(11):113303, dec 2005.

[124] Horatiu C. Dragnea, Alejandro Lopez Ortega, Hani Kamhawi, and Iain D. Boyd. Simulation of a Hall Effect Thruster Using Krypton Propellant. *Journal of Propulsion and Power*, 36(3):335–345, may 2020.

[125] J. D. Bukowski, D. B. Graves, and P. Vitello. Two-dimensional fluid model of an inductively coupled plasma with comparison to experimental spatial profiles. *Journal of Applied Physics*, 80(5):2614–2623, sep 1996.

[126] D. Bose, T.R. Govindan, and M. Meyyappan. Modeling of a helicon plasma source. *IEEE Transactions on Plasma Science*, 31(4):464–470, aug 2003.

[127] Ronald L. Kinder and Mark J. Kushner. Wave propagation and power deposition in magnetically enhanced inductively coupled and helicon plasma sources. *Journal of Vacuum Science Technology A: Vacuum, Surfaces, and Films*, 19(1):76–86, jan 2001.

[128] Álvaro Sánchez-Villar, Jiewei Zhou, Eduardo Ahedo, and Mario Merino. Coupled plasma transport and electromagnetic wave simulation of an ECR thruster. *Plasma Sources Science and Technology*, 30(4):045005, apr 2021.

[129] J Zhou, D Pérez-Grande, P Fajardo, and E Ahedo. Numerical treatment of a magnetized electron fluid model within an electromagnetic plasma thruster simulation code. *Plasma Sources Science and Technology*, 28(1):115004, nov 2019.

[130] M. Magarotto, D. Melazzi, and D. Pavarin. 3D-VIRTUS: Equilibrium condition solver of radio-frequency magnetized plasma discharges for space applications. *Computer Physics Communications*, 247:106953, feb 2020.

[131] Mirko Magarotto, Marco Manente, Fabio Trezzolani, and Daniele Pavarin. Numerical model of a helicon plasma thruster. *IEEE Transactions on Plasma Science*, 48(4):835–844, 2020.

[132] Sumio Ashida, C. Lee, and M. A. Lieberman. Spatially averaged (global) model of time modulated high density argon plasmas. *Journal of Vacuum Science & Technology A*, 13(5):2498–2507, 1995.

[133] E. Suetomi, M. Tanaka, S. Kamiya, S. Hayashi, S. Ikeda, H. Sugawara, and Y. Sakai. Two-dimensional fluid simulation of plasma reactors for the immobilization of krypton. *Computer Physics Communications*, 125(1-3):60–74, mar 2000.

[134] J. Meunier, Ph. Belenguer, and J. P. Boeuf. Numerical model of an ac plasma display panel cell in neon-xenon mixtures. *Journal of Applied Physics*, 78(2):731–745, jul 1995.

[135] L C Pitchford, L L Alves, K Bartschat, S F Biagi, M C Bordage, A V Phelps, C M Ferreira, G J M Hagelaar, W L Morgan, S Pancheshnyi, et al. Comparisons of sets of electron–neutral scattering cross sections and swarm parameters in noble gases: I. Argon. *Journal of Physics D: Applied Physics*, 46(33):334001, aug 2013.

[136] M C Bordage, S F Biagi, L L Alves, K Bartschat, S Chowdhury, L C Pitchford, G J M Hagelaar, W L Morgan, V Puech, and O Zatsarinny. Comparisons of sets of electron–neutral scattering cross sections and swarm parameters in noble gases: III. Krypton and xenon. *Journal of Physics D: Applied Physics*, 46(33):334003, aug 2013.

[137] L L Alves, K Bartschat, S F Biagi, M C Bordage, L C Pitchford, C M Ferreira, G J M Hagelaar, W L Morgan, S Pancheshnyi, A V Phelps, et al. Comparisons of sets of electron–neutral scattering cross sections and swarm parameters in noble gases: II. Helium and neon. *Journal of Physics D: Applied Physics*, 46(33):334002, aug 2013.

[138] P.A. Miller, G.A. Hebner, K.E. Greenberg, P.D. Pochan, and B.P. Aragon. An Inductively-Coupled Plasma Source for the Gaseous Electronics Conference Rf Reference Cell. *Journal of Research of the National Institute of Standards and Technology*, 100(4):427, jul 1995.

[139] Kirill E. Evdokimov, Maxim E. Konischev, Vladimir F. Pichugin, and Z. Sun. Study of argon ions density and electron temperature and density in magnetron plasma by optical emission spectroscopy and collisional-radiative model. *Resource-Efficient Technologies*, 3(2):187–193, jun 2017.

[140] Xi-Ming Zhu and Yi-Kang Pu. A simple collisional–radiative model for low-pressure argon discharges. *Journal of Physics D: Applied Physics*, 40(8):2533–2538, apr 2007.

[141] Nist: National institute of standards and technology.

[142] Kazunori Takahashi, Aiki Chiba, Atsushi Komuro, and Akira Ando. Axial Momentum Lost to a Lateral Wall of a Helicon Plasma Source. *Physical Review Letters*, 114(19):195001, may 2015.

[143] G. J.M. Hagelaar and L. C. Pitchford. Solving the boltzmann equation to obtain electron transport coefficients and rate coefficients for fluid models. *Plasma Sources Science and Technology*, 14:722–733, 11 2005.

[144] R Mewe. Relative intensity of helium spectral lines as a function of electron temperature and density. *British Journal of Applied Physics*, 18(1):107–118, jan 1967.

[145] Richard H. Huddlestone and Stanley L. Leonard. *Plasma Diagnostic Techniques*. Academic Press; 1st edition (January 1, 1965), 1966.

[146] A. Schwabedissen, E. C. Benck, and J. R. Roberts. Langmuir probe measurements in an inductively coupled plasma source. *Physical Review E*, 55(3):3450–3459, mar 1997.

[147] Wei Yang, Sergey N Averkin, Alexander V Khrabrov, Igor D Kaganovich, You-Nian Wang, Spyridon Aleiferis, and Panagiotis Svarnas. Benchmarking and validation of global model code for negative hydrogen ion sources articles you may be interested in. *Phys. Plasmas*, 25:113509, 2018.

[148] Johan Carlsson, Alexander Khrabrov, Igor Kaganovich, Timothy Sommerer, and David Keating. Validation and benchmarking of two particle-in-cell codes for a glow discharge. *Plasma Sources Science and Technology*, 26:014003, 11 2016.

[149] M. M. Turner, A. Derzsi, Z. Donkó, D. Eremin, S. J. Kelly, T. Lafleur, and T. Mussenbrock. Simulation benchmarks for low-pressure plasmas: Capacitive discharges. *Physics of Plasmas*, 20:013507, 1 2013.

[150] Antonin Berthelot and Annemie Bogaerts. Modeling of plasma-based co2 conversion: lumping of the vibrational levels. *Plasma Sources Science and Technology*, 25:045022, 7 2016.

[151] L L Alves. The IST-LISBON database on LXCat. *Journal of Physics: Conference Series*, 565:012007, dec 2014.

[152] TRINITI Database. Available online: `https://www.lxcat.net/TRINITI` (Accessed on 1 January 2021).

[153] PUECH Database. Available online: `https://www.lxcat.net/Puech` (Accessed on 1 January 2021).

[154] HAYASHI Database. Available online: `https://www.lxcat.net/Hayashi` (Accessed on 1 January 2021).

[155] O Zatsarinny and K Bartschat. B-spline breit– pauli r-matrix calculations for electron collisions with argon atoms. *Journal of Physics B: Atomic, Molecular and Optical Physics*, 37(23):4693–4706, nov 2004.

[156] M. Allan, O. Zatsarinny, and K. Bartschat. Near-threshold absolute angle-differential cross sections for electron-impact excitation of argon and xenon. *Phys. Rev. A*, 74:030701, Sep 2006.

[157] BIAGI V8.97 Database. Available online: `https://www.lxcat.net/Biagi` (Accessed on 1 January 2021).

[158] M A Khakoo, P Vandeventer, J G Childers, I Kanik, C J Fontes, K Bartschat, V Zeman, D H Madison, S Saxena, R Srivastava, and A D Stauffer. Electron impact excitation of the argon 3p54s configuration: differential cross-sections and cross-section ratios. *Journal of Physics B: Atomic, Molecular and Optical Physics*, 37(1):247–281, dec 2003.

[159] J. Ethan Chilton, John B. Boffard, R. Scott Schappe, and Chun C. Lin. Measurement of electron-impact excitation into the 3p5-4p levels of argon using Fourier-transform spectroscopy. *Physical Review A*, 57(1):267–277, jan 1998.

[160] NGFSRDW Database. Available online: `https://www.lxcat.net/NGFSRDW` (Accessed on 1 January 2021).

[161] Oleg Zatsarinny and Klaus Bartschat. B -spline calculations of oscillator strengths in neutral argon. *Journal of Physics B: Atomic, Molecular and Optical Physics*, 39(9):2145–2158, may 2006.

[162] John B. Boffard, Garrett A. Piech, Mark F. Gehrke, L. W. Anderson, and Chun C. Lin. Measurement of electron-impact excitation cross sections out of metastable levels of argon and comparison with ground-state excitation. *Physical Review A*, 59(4):2749–2763, apr 1999.

[163] MORGAN Database. Available online: `https://www.lxcat.net/Morgan` (Accessed on 1 January 2021).

[164] COP Database. Available online: `https://www.lxcat.net/COP` (Accessed on 1 January 2021).

[165] BIAGI v7 Database. Available online: `https://www.lxcat.net/Biagi-v7.1` (Accessed on 1 January 2021).

[166] PHELPS Database. Available online: `https://www.lxcat.net/Phelps` (Accessed on 1 January 2021).

[167] SIGLO Database. Available online: `https://www.lxcat.net/SIGLO` (Accessed on 1 January 2021).

[168] H. A. Hyman. Electron-impact ionization cross sections for excited states of the rare gases (ne, ar, kr, xe), cadmium, and mercury. *Phys. Rev. A*, 20:855–859, Sep 1979.

[169] H. Deutsch, K. Becker, A.N. Grum-Grzhimailo, K. Bartschat, H. Summers, M. Probst, S. Matt-Leubner, and T.D. Märk. Calculated cross sections for the electron-impact ionization of excited argon atoms using the DM formalism. *International Journal of Mass Spectrometry*, 233(1-3):39–43, apr 2004.

[170] S S Baghel, S Gupta, R K Gangwar, and R Srivastava. Diagnostics of low-temperature neon plasma through a fine-structure resolved collisional–radiative model. *Plasma Sources Science and Technology*, 28(11):115010, nov 2019.

[171] Timothy J Sommerer. Model of a weakly ionized, low-pressure xenon dc positive column discharge plasma. *Journal of Physics D: Applied Physics*, 29(3):769–778, mar 1996.

[172] P. Grondein, T. Lafleur, P. Chabert, and A. Aanesland. Global model of an iodine gridded plasma thruster. *Physics of Plasmas*, 23(3):033514, mar 2016.

[173] Franco Javier Bosi. Global model of microwave plasma assisted N 2 O dissociation for monopropellant propulsion. *Physics of Plasmas*, 26(3):033510, mar 2019.

[174] D L Crintea, U Czarnetzki, S Iordanova, I Koleva, and D Luggenhölscher. Plasma diagnostics by optical emission spectroscopy on argon and comparison with Thomson scattering. *Journal of Physics D: Applied Physics*, 42(4):045208, feb 2009.

[175] K.A. Polzin, J.F. Seixal, and S.L. Mauro. The iodine satellite (isat) propellant feed system – design and development, 2017.

[176] Thrustme. `https://www.thrustme.fr`, Accessed on 1 January 2022.

[177] Florian Marmuse. Iodine plasmas: experimental and numerical studies. application to electric propulsion, 2020. PhD thesis.

[178] James Szabo. *Fully kinetic numerical modeling of a plasma thruster*. PhD thesis, Massachusetts Institute of Technology, Jul. 2001.

[179] S. Dalle Fabbriche R. Andriulli S. Andrews F. Ponti D. Pavarin N. Souhair, M. Magarotto. Development activities for the rf helicon-based plasma thruster: Thrust measurement and b-dot probe set-upsimulation and modelling of an iodine fed helicon plasma thruster. In *Proceedings of the 37th International Electric Propulsion Conference*, number IEPC-2022-496, Boston, USA, 2022.

[180] Lubos Brieda and Michael Keidar. Development of the starfish plasma simulation code and update on multiscale modeling of hall thrusters. 2012.

[181] Hong Qin, Shuangxi Zhang, Jianyuan Xiao, Jian Liu, Yajuan Sun, and William M. Tang. Why is boris algorithm so good? *Physics of Plasmas*, 20(8):084503, 2013.

[182] Simone Di Fede, Mirko Magarotto, Shaun Andrews, and Daniele Pavarin. Simulation of the plume of a magnetically enhanced plasma thruster with spis. *Journal of Plasma Physics*, 87(6):905870611, 2021.

[183] Shaun Andrews, Simone Di Fede, and Mirko Magarotto. Fully kinetic model of plasma expansion in a magnetic nozzle. *Plasma Sources Science and Technology*, 02 2022.

[184] M. Magarotto, S. Di Fede, N. Souhair, S. Andrews, and F. Ponti. Numerical suite for cathodeless plasma thrusters. *Acta Astronautica*, 197:126–138, 2022.

[185] C. K. Birdsall. Particle-in-cell charged-particle simulations, plus monte carlo collisions with neutral atoms, pic-mcc. *IEEE Transactions on Plasma Science*, 19(2):65–85, 1991.

[186] G A Bird. *Molecular gas dynamics and the direct simulation of gas flows.* Clarendon: Oxford University press, 1994.

[187] F Trezzolani, M Magarotto, M Manente, and D Pavarin. Development of a counter-balanced pendulum thrust stand for electric propulsion. *Measurement*, 122:494–501, 2018.

[188] Kazutaka Nishiyama. Air breathing ion engine concept, 2012.

[189] T. Andreussi et al. Development and experimental validation of a hall effect thruster ram-ep concept, 2017.

[190] V. Hruby, B. Pote, and T. Brogan. Air breathing electrically powered hall effect thruster, 2004.

[191] P. Zheng, J. Wu, and Y. Zhang. A comprehensive review of atmosphere-breathing electric propulsion systems, 2004.

[192] F. Romano et al. Inductive plasma thruster (ipt) for an atmosphere-breathing electric propulsion system: Design and set inoperation, 2019.

[193] B.A. BanksBruce, A. Banks, and K.K. deGroh. Low earth orbital atomic oxygen interactions with spacecraft materials, 2004.

[194] J. M. Picone, A. E. Hedin, D. P. Drob, and A. C. Aikin. Nrlmsise-00 empirical model of the atmosphere: Statistical comparisons and scientific issues. *Journal of Geophysical Research: Space Physics*, 107(A12):SIA 15–1–SIA 15–16, 2002.

[195] Anmol Taploo, Li Lin, and Michael Keidar. Analysis of ionization in air-breathing plasma thruster. *Physics of Plasmas*, 28:093505, 09 2021.

[196] F Romano, Y.-A. Chan, G. Herdrich, C. Traub, S. Fasoulas, P.C.E. Roberts, K. Smith, S. Edmondson, S. Haigh, N.H. Crisp, V.T.A. Oiko, S.D. Worrall, S. Livadiotti, C. Huyton, L.A. Sinpetru, A. Straker, J. Becedas, R.M. Domínguez, D. González, V. Cañas, V. Sulliotti-Linner, V. Hanessian, A. Mølgaard, J. Nielsen, M. Bisgaard, D. Garcia-Almiñana, S. Rodriguez-Donaire, M. Sureda, D. Kataria, R. Outlaw, R. Villain, J.S. Perez, A. Conte, B. Belkouchi, A. Schwalber, and B. Heißerer. Rf helicon-based inductive plasma thruster (ipt) design for an atmosphere-breathing electric propulsion system (abep). *Acta Astronautica*, 176:476–483, 2020.

[197] Ph Guittienne, R. Jacquier, B. Pouradier Duteil, A. A. Howling, R. Agnello, and I. Furno. Helicon wave plasma generated by a resonant birdcage antenna: magnetic field measurements and analysis in the raid linear device. *Plasma Sources Science and Technology*, 30:075023, 7 2021.

[198] F Romano, Y.-A. Chan, G. Herdrich, C. Traub, S. Fasoulas, P.C.E. Roberts, N. Crisp, B.E.A. Holmes, S. Edmondson, S. Haigh, S. Livadiotti, A. Macario-Rojes,

L.A. Oiko, V.T.A. amd Sinpetru, Becedas J. Smith, K., V. Sulliotti-Linner, M. Bisgaard, S. Christensen, V. Hanessian, T. Kauffman Jensen, J. Nielsen, D. Garcia-Almiñana, M. Garcia-Berenguer, S. Rodriguez-Donaire, M. Sureda, D. Kataria, B. Belkouchi, A. Conte, and S. Seminari. Design, set-up, and first ignition of the rf helicon-based plasma thruster. *Space Propulsion Conference 2020+1*, 247, 2021.

[199] F. Romano, G. Herdrich, Y.-A. Chan, N. Crisp, P. C.E. Roberts, B. E.A. Holmes, S. Edmondson, S. Haigh, Macario-Rojes, A., V.T.A. Oiko, L.A. Sinpetru, K. Smith, J. Becedas, V. Sulliotti-Linner, M. Bisgaard, S. Christensen, V. Hanessian, T. Kauffman Jensen, J. Nielsen, S. Fasoulas, C. Traub, D. Garcia-Almiñana, S. Rodriguez-Donaire, M. Sureda, D. Kataria, B. Belkouchi, A. Conte, S. Seminari, and R. Villain. Design of an intake and a thruster for an atmosphere-breathing electric propulsion system. *CEAS Space Journal*, 2022.

[200] Schafft Marcel. Design and test of a baffle plate to perfom first thrust measurement of the ipt. Master Thesis, University of Stuttgart, Institute of Space Systems, 2022.

[201] K. Takahashi, A. Komuro, and A. Ando. Measurement of plasma momentum exerted on target by a small helicon plasma thruster and comparison with direct thrust measurement. *Journal Article in The Review of scientific instruments*, 86(2), 2015.

[202] A. Spethmann, T. Trottenberg, , and H. Kersten. Measurement and simulation of forces generated when a surface is sputtered. *Journal Article in Physics of Plasmas*, 24(9), 2017.

[203] K. Takahashi. Helicon-type radiofrequency plasma thrusters and magnetic plasma nozzles. *Journal Article in Reviews of Modern Plasma Physics*, 3(1), 2019.

[204] L. D. Flansburg and N. Hershkowitz. Magnetism in austenitic stainless steels. *Journal Article in Journal of Applied Physics*, 41(10), 1970.

[205] W. A. Johnson and L. K. Warne. Electrophysics of micromechanical comb actuators. *Journal Article in Journal of Microelectromechanical Systems*, 4(1), 1995.

[206] Deepak Bose, T. R. Govindan, and M. Meyyappan. Modeling of a helicon plasma source. *IEEE Transactions on Plasma Science*, 31:464–470, 8 2003.

[207] Eduardo Ahedo, Sara Correyero, J Navarro-Cavallé, and Mario Merino. Macroscopic and parametric study of a kinetic plasma expansion in a paraxial magnetic nozzle. *Plasma Sources Science and Technology*, 29(4):045017, 2020.

[208] G. Gallina, M. Magarotto, M. Manente, and Daniele Pavarin. Enhanced bidimensional pic: an electrostatic/magnetostatic particle-in-cell code for plasma based systems. *Journal of Plasma Physics*, 85:905850205, 4 2019.

[209] N. Souhair, M. Magarotto, F. Ponti, and D. Pavarin. Analysis of the plasma transport in numerical simulations of helicon plasma thrusters. *AIP Advances*, 11(11):115016, November 2021.

[210] F Moukalled, L Mangani, M Darwish, and *et al.* *The finite volume method in computational fluid dynamics.* Springer, Cham, DE, 2016.

[211] Simone Di Fede, Mirko Magarotto, Shaun Andrews, Marco Manente, and Daniele Pavarin. Numerical simulation of the plume of a magnetically enhanced plasma thruster. In *Proceedings of the 7th Space Propulsion Conference SP2020-00111*, Online conference, 2020.

[212] Thomas Howard Stix. *The theory of plasma waves.* McGraw-Hill, New York NY, USA, 1962.

[213] Francis F Chen and David D Blackwell. Upper limit to landau damping in helicon discharges. *Physical review letters*, 82(13):2677, 1999.

[214] JL Kline and EE Scime. Parametric decay instabilities in the helix helicon plasma source. *Physics of Plasmas*, 10(1):135–144, 2003.

[215] Matthew M Balkey, Robert Boivin, John L Kline, and Earl E Scime. Ion heating and density production in helicon sources near the lower hybrid frequency. *Plasma Sources Science and Technology*, 10(2):284, 2001.

[216] Isaac D Sudit and Francis F Chen. Discharge equilibrium of a helicon plasma. *Plasma Sources Science and Technology*, 5(1):43–53, 1996.

[217] D Pavarin, F Ferri, M Manente, D Rondini, D Curreli, Y Guclu, M Melazzi, S Suman, and G Bianchini. Helicon Plasma Hydrazine: COmbined Micro project overview and development status. In *Proceedings of the 2^{nd} Space Propulsion Conference*, number SP2010-1842379, San Sebastian, ES, 2010.

[218] M Manente, F Trezzolani, M Magarotto, A Selmo, E Fantino, G Miste, E Toson, and D Pavarin. A low-cost helicon propulsion system to boost small satellite missions. In *Proceedings of 68th Internationa Astronautical Congress IAC, Adelaide, AU*, 2017.

[219] A Fiala, L C Pitchford, and J P Boeuf. Two-dimensional, hybrid model of low-pressure glow discharges. *Physical Review E*, 49(6):5607–5622, 1994.

[220] Deepak Bose, T R Govindan, and M Meyyappan. Modelling of magnetic field profile effects in a helicon source. *Plasma Sources Science and Technology*, 13(4):553–561, August 2004.

[221] JD Bukowski, DB Graves, and P Vitello. Two-dimensional fluid model of an inductively coupled plasma with comparison to experimental spatial profiles. *Journal of Applied Physics*, 80(5):2614–2623, 1996.

[222] M Abdollahzadeh, JC Pascoa, and PJ Oliveira. Implementation of the classical plasma–fluid model for simulation of dielectric barrier discharge (dbd) actuators in openfoam. *Computers & Fluids*, 128:77–90, 2016.

[223] N Souhair, M Magarotto, E Majorana, F Ponti, and D Pavarin. Development of a lumping methodology for the analysis of the excited states in plasma discharges operated with argon, neon, krypton, and xenon. *Physics of Plasmas*, 28(9):093504, 2021.

[224] Ronald L. Kinder and Mark J. Kushner. Noncollisional heating and electron energy distributions in magnetically enhanced inductively coupled and helicon plasma sources. *Journal of Applied Physics*, 90:3699–3712, 10 2001.

[225] Richard S Brokaw. Predicting transport properties of dilute gases. *Industrial & Engineering Chemistry Process Design and Development*, 8(2):240–253, 1969.

[226] Philip D Neufeld, AR Janzen, and RA Aziz. Empirical equations to calculate 16 of the transport collision integrals ω (l, s)* for the Lennard-Jones (12–6) potential. *The Journal of Chemical Physics*, 57(3):1100–1102, 1972.

[227] Kirill E. Evdokimov, Maxim E. Konischev, Vladimir F. Pichugin, and Z. Sun. Study of argon ions density and electron temperature and density in magnetron plasma by optical emission spectroscopy and collisional-radiative model. *Resource-Efficient Technologies*, 3:187–193, 6 2017.

[228] E Ahedo, JM Gallardo, and M Martınez-Sánchez. Effects of the radial plasma-wall interaction on the hall thruster discharge. *Physics of Plasmas*, 10(8):3397–3409, 2003.

[229] Francis F. Chen. *Introduction to Plasma Physics and Controlled Fusion.* Springer International Publishing, 2016.

[230] J. P. Boeuf and L. Garrigues. Low frequency oscillations in a stationary plasma thruster. *Journal of Applied Physics*, 84:3541–3554, 10 1998.

[231] Ioannis G Mikellides, Ira Katz, Dan M Goebel, and James E Polk. Hollow cathode theory and experiment. ii. a two-dimensional theoretical model of the emitter region. *Journal of Applied Physics*, 98(11):113303, 2005.

[232] GJM Hagelaar, FJ De Hoog, and GMW Kroesen. Boundary conditions in fluid models of gas discharges. *Physical Review E*, 62(1):1452, 2000.

[233] Suhas V. Patankar. *Numerical Heat Transfer and Fluid Flow.* CRC Press, October 2018.

[234] GJM Hagelaar and GMW Kroesen. Speeding up fluid models for gas discharges by implicit treatment of the electron energy source term. *Journal of Computational Physics*, 159(1):1–12, 2000.

[235] Timothy Ziemba, John Carscadden, John Slough, James Prager, and Robert Winglee. High power helicon thruster. In *41st AIAA/ASME/SAE/ASEE Joint Propulsion Conference & Exhibit,AIAA-2005-4119*, Tucson, AZ, USA, 2005.

[236] Arnab Rai Choudhuri. *The physics of fluids and plasmas: an introduction for astrophysicists.* Cambridge University Press, Cambridge, UK, 1998.

[237] Trevor Lafleur, Christine Charles, and RW Boswell. Characterization of a helicon plasma source in low diverging magnetic fields. *Journal of Physics D: Applied Physics*, 44(5):055202, 2011.

[238] V. V. Gorin, A. A. Kudryavtsev, Jingfeng Yao, Chengxun Yuan, and Zhongxiang Zhou. Boundary conditions for drift-diffusion equations in gas-discharge plasmas. *Physics of Plasmas*, 27(1):013505, 2020.

[239] George Livadiotis. Kappa distributions: Statistical physics and thermodynamics of space and astrophysical plasmas. *Universe*, 4:144, 12 2018.

[240] E.F. Toro. *Riemann Solvers and Numerical Methods for Fluid Dynamics: A Practical Introduction.* Springer Berlin Heidelberg, 2009.

[241] A Schwabedissen, Eric C Benck, and JR Roberts. Langmuir probe measurements in an inductively coupled plasma source. *Physical Review E*, 55(3):3450, 1997.

[242] Mirko Magarotto, Paola De Carlo, Giulia Mansutti, Franco J. Bosi, Nicholas E. Buris, Antonio-D. Capobianco, and Daniele Pavarin. Numerical suite for gaseous plasma antennas simulation. *IEEE Transactions on Plasma Science*, 49:285–297, 1 2021.

[243] Paola De Carlo, Mirko Magarotto, Giulia Mansutti, Stefano Boscolo, Antonio-Daniele Capobianco, and Daniele Pavarin. Experimental characterization of a plasma dipole in the uhf band. *IEEE Antennas and Wireless Propagation Letters*, 2021.

[244] Paola De Carlo, Mirko Magarotto, Giulia Mansutti, Antonio Selmo, Antonio-Daniele Capobianco, and Daniele Pavarin. Feasibility study of a novel class of plasma antennas for satcom navigation systems. *Acta Astronautica*, 178:846–853, 1 2021.

[245] Alexander Daykin-Iliopoulos, Franco Bosi, Fabio Coccaro, Mirko Magarotto, Athanasios Papadimopoulos, Paola De Carlo, Cristian Dobranszki, Igor Golosnoy, and Steve Gabriel. Characterisation of a thermionic plasma source apparatus for high-density gaseous plasma antenna applications. *Plasma Sources Science and Technology*, 29:115002, 11 2020.

[246] Giulia Mansutti, Paola De Carlo, Mohammad A. Hannan, Federico Boulos, Paolo Rocca, Antonio-D. Capobianco, Mirko Magarotto, and Alberto Tuozzi. Modeling and design of a plasma-based transmit-array with beam scanning capabilities. *Results in Physics*, 16:102923, 3 2020.

[247] Ch. Berenguer, K. Katsonis, and J. Gonzalez. Using of an iodine detailed global model for characterization and for optical diagnostics of helicon thrusters, 2018.

[248] Simone Di Fede, Mirko Magarotto, Shaun Andrews, and Daniele Pavarin. Simulation of the plume of a magnetically enhanced plasma thruster with SPIS. *Journal of Plasma Physics*, 87(6), December 2021.

[249] Yukinori Sakiyama. Plasma chemistry model of surface microdischarge in humid air and dynamics of reactive neutral species, 2012.

[250] J. Zhou and F. Taccogna et al. Performance analysis of alternative propellants for a helicon plasma thruster, 2021.

[251] Lxcat, the plasma data exchange project, https://nl.lxcat.net.